

University of Alberta

**Passive and Non-mechanical Pumping in Microfluidic
Devices**

by
Prashant Rakhmaji Waghmare

A thesis submitted to the Faculty of Graduate Studies and Research in
partial fulfillment of the requirements for the degree of

Doctor of Philosophy

Department of Mechanical Engineering

©Prashant Rakhmaji Waghmare
Fall 2012
Edmonton, Alberta

Permission is hereby granted to the University of Alberta Libraries to reproduce single copies of this thesis and to lend or sell such copies for private, scholarly or scientific research purposes only. Where the thesis is converted to, or otherwise made available in digital form, the University of Alberta will advise potential users of the thesis of these terms.

The author reserves all other publication and other rights in association with the copyright in the thesis and, except as herein before provided, neither the thesis nor any substantial portion thereof may be printed or otherwise reproduced in any material form whatsoever without the author's prior written permission.

To My Family and friends

Abstract

Last couple of decades have witnessed massive upsurge in efforts of transporting and manipulating solutes and moieties in microfluidic devices, motivated by their wide applications in disciplines ranging from astrophysics to nanomedicine. Pressure-driven transport scales as the square of the channel height, and therefore demands massive pumping power for microchannels making it unusable in several microfluidic applications. Accordingly, there have been a plethora of endeavors to devise novel non-mechanical fluid driving techniques in microchannels, e.g., transport by applying electrostatic, magnetic, or acoustic forces. However, these mechanisms, often necessitate special fluid properties, as well as cumbersome fabrication requirements. Hence, there has been a tremendous drive to develop passive pumping mechanisms, that successfully exploit the inherent geometric and physical characteristics of the microchannel and the fluid, *yet* are free from the above constraints.

In this thesis, several aspects of one of the foremost microfluidic passive pumping mechanisms, namely capillary-driven transport, has been analyzed. Firstly, the effect of a transient velocity profile on a classical capillary filling problem has been investigated. All the existing analyses invariably consider a fully-developed velocity profile – accordingly, the proposed model could reveal several *yet unaddressed* non-trivial mechanisms inherent in a capillary filling problem, intrinsic to the consideration of a more generalized situation of a developing velocity profile.

Secondly, an appropriate analytical model has been developed to describe the pressure-field at the entrance of the capillary. This pressure-field improves on the existing expressions in the sense that it is applicable to capillaries of all possible aspect ratios, and manifest its influence by predicting a capillary filling length that is different from that hypothesized by the existing models.

Thirdly, important correlations interrelating the wetting and other physical properties of popular biomicrofluidic solvents such as BSA (Bovine Serum Albumin) solution or microbead suspension have been derived from thoroughly performed experimental studies. These correlations are next employed to study the capillary dynamics of these two liquid as a functions of its physical properties.

Finally, effects of additional body forces, such as gravity or electrostatics, in affecting a capillary transport have been investigated.

Acknowledgements

The last four years of my PhD in the University of Alberta have been by far the most memorable phase of my life. It has been a most amazing and unforgettable journey where at every step I have been embraced by new horizons of learning, research and their associated challenges. The person to whom I am most indebted to make this journey a success is my PhD supervisor Dr. Sushanta K. Mitra. Apart from educating me on different aspects of my research, he inculcated in me all the necessarily professional qualities. I am thankful to him for teaching me invaluable scientific communication and writing skills. I am amazed by his great vision, professional attitude and zest for excellence in all aspects of the work. He has been the ultimate role model of energy, knowledge, hard work, patience, motivation and sacrifice that I have always tried to emulate.

I would like to thank the members of my supervisory committee, Dr. Subir Bhattacharjee and Dr. Thomas Thundat, for their valuable suggestions and advices which went a long way in improving my thesis. I would also like to thank the members of my examining committee: Dr. Meenakshinathan Parameswaran, Dr. Anthony Yeung, Dr. Marc Secanell and Dr. Cagri Ayranci, for reviewing my thesis.

I am grateful to all the Mechanical Engineering department office staff, machine shop staff, and IT personnel for their generous help at different stages. I am also thankful to all the support staff at NRC facility and Nanofab.

I would like to acknowledge the financial support from Alberta Ingenuity, now part of Alberta Innovates-Technology Futures, provided through the Graduate Student Scholarship in Nanotechnology.

I would like to thank all my past and the present colleagues of Micro Nano Transport Laboratory (MNTL). I would like to specially thank Dr. Siddhartha Das, presently a postdoctoral fellow in MNTL, for his valuable scientific inputs towards my research. I am extremely indebted to him for helping me compile certain sections of the thesis. I would also like to thank Naga Siva Kumar Gunda, presently a PhD candidate in MNTL, for his overwhelming support at various occasions.

To me, friends who have not directly contributed to my research have been equally influential. The first and foremost among them is Olena Sivachenko – I express my special thanks to her for her support and guidance at different occasions. I am also very much grateful to Richard Groulix, Farhan Ahmad and Sampada Bagai. I would also like to thank the Mechanical Engineering Graduate Student Association (MEGSA) team mates, for making my Presidentship in MEGSA very eventful.

I would also like to thank my M-Tech project supervisor, Dr. Nakka Muraidhar Rao, for inspiring me to do PhD. Finally, I express my deepest regards and gratitude to my family members without whose blood, sweat and incessant sacrifices my journey would not have been possible. My parents have always been a source of inspiration for me. Finally, I would like to dedicate this work to my both brothers Kunal and Anand, who made several sacrifices at different stages of their professional careers to ensure that I can successfully complete this journey.

Contents

1 Introduction	1
1.1 Motivation	1
1.2 Objective	5
1.3 Outline of thesis	5
1.3.1 Thesis Contributions	5
1.3.2 Thesis Outline	6
References	8
2 A comprehensive theoretical model of capillary transport in rectangular microchannels	11
2.1 Introduction	11
2.2 Mathematical modeling	15
2.3 Effect of developing velocity profile in capillary transport . . .	20
2.4 Pressure field at the entrance of the microchannel	25
2.4.1 Pressure field at the entrance of non-circular microchannels	27
2.5 Effect of appropriate pressure field in the capillary transport .	33
2.6 Conclusion	35
References	37
3 On the derivation of pressure field distribution at the entrance of a rectangular capillary	41
3.1 Introduction	41
3.2 Pressure field distribution at the entrance of the parallel plate arrangement	43

3.3	Comparison between the pressure field based on the equivalent radius and the exact solution	49
3.4	Conclusion	50
	References	52
4	Contact angle hysteresis of microbead suspensions	54
4.1	Introduction	54
4.2	Experimental details	59
4.2.1	Sample preparation	60
4.2.2	Surface tension measurement	62
4.2.3	Dynamic contact angle measurement	63
4.3	Results and discussion	64
4.4	Conclusion	75
	References	77
5	Contact angle hysteresis of Bovine Serum Albumin (BSA) solution/metal (Au-Cr) coated glass substrate	83
5.1	Introduction	83
5.2	Experimental details	85
5.2.1	Surface characterization	86
5.2.2	Surface tension and contact angle measurements	86
5.3	Results and discussion	87
5.4	Conclusion	96
	References	98
6	Finite Reservoir Effect on Capillary Flow of Microbead Suspension in Rectangular Microchannels	102
6.1	Introduction	102
6.2	Mathematical modeling for gravity assisted capillary transport	106
6.2.1	Pressure field and force at the inlet of rectangular microchannel	109

6.2.2	Physical properties of suspension	112
6.3	Results and discussion	116
6.4	Conclusion	125
References		127
7	Modeling of combined electroosmotic and capillary flow in microchannels	131
7.1	Introduction	131
7.2	Formulation of the Mathematical Model and Solution	134
7.3	Results and Discussion	141
7.4	Conclusion	155
References		157
8	General discussion and conclusion	161
8.1	Overview and Summary	161
8.2	Scope of Future Work	163
References		165
Appendix		166
A-1	Detailed explanation of momentum equation	166
A-2	Dimensional governing equation	169
A-2.1	Expressions for constants of non-dimensional governing equation	171
A-3	Detailed explanation of numerical technique used	173
References		173

List of Tables

2.1	Constants of the generalized non-dimensional governing equation for a capillary flow in a rectangular microchannel with a developing velocity profile	20
3.1	Comparison between the coefficients of the expression used in the literature and proposed expression in the presented analysis	49
4.1	Correlations for contact angle and surface tension using curve fitting to the measurement values over the range of the volume fraction expressed in percentage. The values in the parenthesis represent the corresponding coefficient of determination of the curve.	74
6.1	Empirical correlations for contact angle and surface tension using curve fitting to the measurement values over the range of the volume fraction expressed in percentage	115
6.2	Constants of the generalized non-dimensional governing equation for a gravity assisted capillary flow of microbead suspension in a microchannel	116

List of Figures

1.1	Schematic of typical Lab-on-a-Chip (LOC) device	3
2.1	Schematic of microchannel of width $2B$ and depth $2W$ considered for the theoretical modeling of capillary transport. Figure (a) shows the rectangular microchannel where the width and depth are comparable to each other and Fig. (b) represents the high aspect ratio microchannel which is considered in this analysis. The dotted line shows the control volume considered for the analysis.	16
2.2	Transient response of penetration depth with fully developed (steady state) and developing (unsteady) velocity profile . . .	22
2.3	Transient response of penetration depth with fully developed (steady state) and developing (unsteady) velocity profile for highly dense and viscous fluid. In both the figures bottom left inset shows the variation in the penetration depth at the beginning of the transport and upper right inset shows the variations in the penetration depth during the attainment of the equilibrium penetration depth.	23
2.4	Transient response in the difference in the penetration depths with fully developed (steady state) and developing (unsteady) velocity profile under different conditions.	24

2.5	The fluid volume from infinite reservoir considered as control volume for pressure field expression analysis. Figure 2.5(a) is the control volume considered for circular capillary, Fig 2.5(b) represents the appropriate control volume for parallel plate arrangement and for rectangular microchannel Fig 2.5(c) is the appropriate control volume. Arrow shows the direction of the fluid flow from the reservoir into the microchannel.	26
2.6	The comparison of variations in the penetration depth with equivalent radius and with recently proposed pressure field expressions. Figure 2.6(a) shows the comparison of penetration depth for $\gamma = 0.05$ where Fig. 2.6(b) shows the comparison for $\gamma = 0.9$	34
3.1	Schematic of the capillary flow between parallel plates with the semicylindrical control volume. Arrows indicating the direction of fluid flow into the capillary	44
4.1	Schematic of a symmetric sessile drop on a solid surface with an equilibrium contact angle.	56
4.2	Pictorial representation of advancing and receding contact angles with initial and final positions of the interface during measurements.	60
4.3	Schematic of the experimental set-up used for dynamic contact angle and surface tension measurements. Images of pendant drop and sessile drops in the inset are captured from the CCD camera.	61
4.4	Variation in the surface tension with the change in the microbead volume fraction. Error bar reveals the range of maximum and minimum surface tension for corresponding measurement series.	65

4.5	Images during the advancement and the recession of sessile drop on the glass substrate. Underneath numbers represent the corresponding time in seconds at which the image has been captured and the respective base diameter in millimeters.	66
4.6	Measurement of average advancing and initial receding contact angle corresponding to the variation in the base diameter for Suspension B of 5% microbead volume fraction on the glass substrate.	68
4.7	Measurement of an average advancing and minimum receding contact angle with corresponding to the variation in the base diameter for the Suspension A of 10% microbead volume fraction on the glass substrate.	70
4.8	Variation in the advancing and receding contact angle of Suspension B with the change in the microbead volume fraction on the glass substrate. Error bar reveals the range of maximum and minimum contact angles for corresponding measurement series.	72
4.9	Variation in the equilibrium contact angle with the microbead volume fraction on the glass substrate for two different microbead suspensions. Solid lines represent the corresponding curve fitted expressions, reported in Table 4.1	73
5.1	The surface roughness measurements of the metal coated glass substrate with an optical profilometer. The surface profile of the scanned area is presented in (a) and, (b) represents the surface roughness of the corresponding area of the substrate.	88
5.2	The variation in the surface tension with the change in the BSA concentration. Error bar reveals the range of maximum and minimum surface tension for the corresponding measurement series.	89

5.3	The variation in the static contact angle with the change in the BSA concentration. Error bar reveals the range of maximum and minimum static contact angle for the corresponding measurement series.	90
5.4	The variations in the base diameter, contact angle, and volume of the sessile drop corresponding to the particular measurement series. The encircled point represents the time at which decrement in the drop volume starts.	92
5.5	Variation in the equilibrium contact angle (θ_e) with the change in the BSA concentration (ϕ). Error bar reveals the range of maximum and minimum equilibrium contact angle for corresponding measurement series. Dotted line represents the corresponding curve fitted expression presented at the bottom right corner and the value in parentheses represents the corresponding coefficient of determination of the curve.	94
6.1	Schematic of gravity assisted capillary flow in a vertically oriented microchannels of width $2B_1$ and depth $2W_1$. The additional gravitational head from the fluid in finite reservoir of size $(2B_2 \times 2W_2)$ is assisting the capillary flow. The depth of microchannel is assumed very large as compared to the width of microchannel.	108
6.2	Transient response of a flow front transport for different gravitational heads in the reservoir with $Bo=0.0055$, $Oh=0.0084$, $\gamma_1=0.05$ $\gamma_2 = 0.2$, $\gamma_B = 0.1$ and $\phi = 0.04$. I : Flow front penetration rate for $H^* = 100$ surpasses the penetration rate for $H^* = 50$. II : Flow front penetration rate for $H^* = 100$ surpasses the penetration rate for $H^* = 10$. III : Flow front penetration rate for $H^* = 50$ surpasses the penetration rate for $H^* = 10$	117

6.3	Transient response of a flow front transport for different ratios of microchannel to reservoir width with $Bo=0.0055$, $Oh=0.0084$, $\gamma_1=0.001$ $\gamma_2 = 0.1$, $H^* = 10.0$ and $\phi = 0.04$. Inset shows the linear increment in the penetration depth under gravity dominating region.	119
6.4	Transient response of a flow front transport for different ratios of microchannel to reservoir width with $Bo=0.0055$, $Oh=0.0084$, $\gamma_1=0.001$ $\gamma_2 = 0.1$, $H^* = 500.0$ and $\phi = 0.04$	120
6.5	Transient response of a flow front transport for different aspect ratios for parallel plate arrangements of the capillary with $Bo=0.0055$, $Oh=0.0084$, $\gamma_B=0.005$, $\gamma_2 = 0.2$, $H^* = 10.0$ and $\phi = 0.04$	122
6.6	Transient response of a flow front transport for different aspect ratios of reservoir with $Bo=0.0055$, $Oh=0.0084$, $\gamma_B=0.005$ $\gamma_1 = 0.005$, $H^* = 10.0$ and $\phi = 0.04$	123
6.7	Transient response of a flow front transport for different concentrations of microbeads with $Bo=0.0055$, $Oh=0.0084$, $\gamma_1 = 0.05$ $\gamma_2 = 0.2$, $\gamma_B=0.1$ and $H^* = 20.0$. The case $\phi = 0$ represents the fluid without microbeads.	124
7.1	Schematic of the microchannel of width $2B$, depth $2W$ and of length L considered for electroosmotically assisted capillary transport.	134
7.2	Transient response of a penetration depth for $0.01 \leq E_o \leq -0.01$ with $Oh = 0.0070$, $Bo = 0.0075$, $\gamma = 0.006$, $\epsilon^* = 0.07$, $L^* = 300$ and $B\kappa = 4$. $E_o = 0$ represents pure capillary flow	142
7.3	Variation in the penetration depth for vertically oriented channel with water as electrolyte where $B = 100\mu m$, $W = 400\mu m$, $L = 75mm$, $\zeta = -75mV$ and constant contact angle of 27° . Inset shows the variation in the electric field within the electrolyte as flow front progresses under different applied voltages	144

7.4	Transient response of a flow front velocity for different E_0 with $Oh = 0.0070$, $Bo = 0.0075$, $\gamma = 0.006$, $\epsilon^* = 0.07$, $L^* = 300$ and $B\kappa = 4$ with constant contact angle of 27°	145
7.5	Transient response of a penetration depth for different non-dimensional permittivity(ϵ^*) with $Oh = 0.0070$, $Bo = 0.0075$, $\gamma = 0.006$, $E_o = -0.001$ and -0.01 , $L^* = 300$ and $B\kappa = 4$ with constant contact angle of 27°	146
7.6	Transient response of a penetration depth for different non-dimensional Debye-length($B\kappa$) with $Oh = 0.0070$, $Bo = 0.0075$, $\gamma = 0.006$, $E_o = -0.01$, $L^* = 300$ and $\epsilon^* = 0.07$ with constant contact angle of 27°	148
7.7	Transient response of a penetration depth for different aspect ratios(γ) with $Oh = 0.0070$, $Bo = 0.0075$, $\epsilon^* = 0.07$, $E_o = -0.01$ and -1.5 , $L^* = 300$ and $B\kappa = 4$ with constant contact angle of 27°	149
7.8	Transient response of a penetration depth for different values of Bond number(Bo) with $Oh = 0.0070$, $\epsilon^* = 0.07$, $E_o = -0.01$ and -1.5 , $L^* = 300$ and $B\kappa = 4$ with constant contact angle of 27°	150
7.9	Transient response of a penetration depth and flow front velocity for different values of Bond number(Bo) with $Oh = 0.0070$, $\epsilon^* = 0.07$, $E_o = -1.5$, $L^* = 300$ and $B\kappa = 4$ with constant contact angle of 27°	151
7.10	Transient response of a penetration depth and flow front velocity for different values of Ohnesorge number(Oh) with $Bo = 0.0075$, $\gamma = 0.006$, $\epsilon^* = 0.07$, $E_o = -0.01$ and -1.5 , $L^* = 300$ and $B\kappa = 4$ with constant contact angle of 27°	153
7.11	Transient response of a penetration depth and flow front velocity for different values of Ohnesorge number(Oh) with $Bo = 0.0075$, $\gamma = 0.006$, $\epsilon^* = 0.07$, $E_o = -1.5$, $L^* = 300$ and $B\kappa = 4$ with constant contact angle of 27°	154

A-1 Free body diagram for a control volume considered in mathematical analysis.	167
---	-----

Nomenclature

B	Width of the rectangular microchannel
Bo	Bond number
C	Coefficients of the governing equations
c	Concentration
d	Diameter
E	Electric field
Eo	Electroosmotic number
F	Force
g	Acceleration due to gravity
h	Penetration depth
L	Length of the channel
M	Momentum
n	Number of particles
Oh	Ohnesorge number
p	Pressure
R	Principle radii of the liquid-air interface curvature

r	Radius of the control volume
t	Time
V	Voltage
v	Velocity
W	Depth of the rectangular microchannel
x	Rectangular coordinates in x-direction
y	Rectangular coordinates in y-direction
z	Rectangular coordinates in z-direction

Greek Letters

ϵ	Permittivity of the medium
γ	Aspect ratio of the microchannel
λ	Debye length
μ	Dynamic viscosity of the fluid
ν	Kinematic viscosity of the fluid
ϕ	Volume fraction
ρ	Density of the fluid
σ	Surface tension of the fluid
θ	Contact angle
ζ	Zeta potential

Superscript

*	Non-dimensional parameters
---	----------------------------

Subscript

atm Atmospheric

e Effective

f Fluid

i At the inlet of the microchannel

p Particle

pf Pressure at flow front

pf Pressure at flow front

x Along the direction of the x-axis

y Along the direction of the y-axis

z Along the direction of the z-axis

Abbreviations

BSA Bovine Serum Albumin

EDL Electric Double Layer

LOC Lab-on-a-chip

MEMS Microelectromechanical System

Chapter 1

Introduction

1.1 Motivation

Over the past and the present decades, microfluidic channels have become integral components of biomedical devices like Lab-on-a-Chip (LOC) (Stone et al., 2004). A typical LOC device consists of three different sections; (i) sample preparation section, (ii) reaction chamber, and (iii) quantification / detection sites (see Fig. 1.1). These sections are interconnected by microchannels of varied geometries and cross-sections. In order to transport biomolecules, particles and chemicals from one section to the other, we therefore need to drive these moieties through these interconnecting microchannels. The necessary driving force is typically achieved through several traditional or conventional pumping mechanisms (Nguyen and Wereley, 2003). Till date these mechanisms are such that the pumping is actuated by some external means, which inevitably introduces several undesired difficulties in operation of the device. These difficulties can be either due to the unfavorable scaling of the corresponding actuation forces in a microchannel, or the possible intrusive changes that the actuation mechanism triggers inside the system. For example, when the transport is achieved by a pressure driven flow, actuated by an externally operated mechanical pump such as a syringe pump, the flow strength scales linearly with the applied pressure gradient and quadratically with the microchannel height – therefore one requires an extremely large pressure-gradient to obtain a satisfactory flow strength in a pressure-driven microchannel flow (Karniadakis

et al., 2005). Additionally, for such a flow external microscopic actuators and connectors with external pumping interface are needed, thereby restricting the flexibility of the devices. To overcome such extremely intuitive difficulties associated with the pressure-driven transport in a microchannel, researchers have attempted other methods of driving flow in a microchannel. These methods typically rely on generating additional volume/surface forces on the liquid, thereby successfully driving a non-pressure-driven transport in the microchannel. To ensure that such non-conventional forces are created one requires additional features to be patterned on the microchannel system, and the rapid advancement in micro-nano-manufacturing in recent times has served as a great blessing for such endeavors. The most important related example is to drive an electrolyte in a microchannel by employing an external electric field applied through micro-manufactured electrodes embedded in the microchannel. Such a transport is classically known as *electroosmosis*, and is one of the four methods of imparting fluid/particle motion by the application of electric field (known as *electrokinetics*). Electroosmosis relies on the fluid motion created by the body force generated by the interaction of the charge density (within the induced Electric Double Layer or EDL formed at the interface of the solid and a dielectric liquid) with the applied electric field. Therefore, the properties of the solid and the liquid dictate the electroosmotic transport. One of the major advantage of the electroosmotically-driven fluid flow over the conventional pressure-driven transport is the absence of any moving mechanical parts, as well as a favorable scaling that appropriately utilizes the enhanced surface-to-volume ratio of a microchannel. In fact, the electroosmotic transport is the most favored non-mechanical transport for microfluidic operations (as compared to other non-mechanical mechanisms such as magnetohydrodynamic, optofluidic or acousto-fluidic transport) owing to factors such as its ease of operation, understanding and repeatability. However, one major difficulty associated with the electrokinetic transport is that it is strongly dependent on the conductivity of the solution. In case the conductivity is very high (i.e., ionic strength is significantly large) the electroosmotic effect is substantially

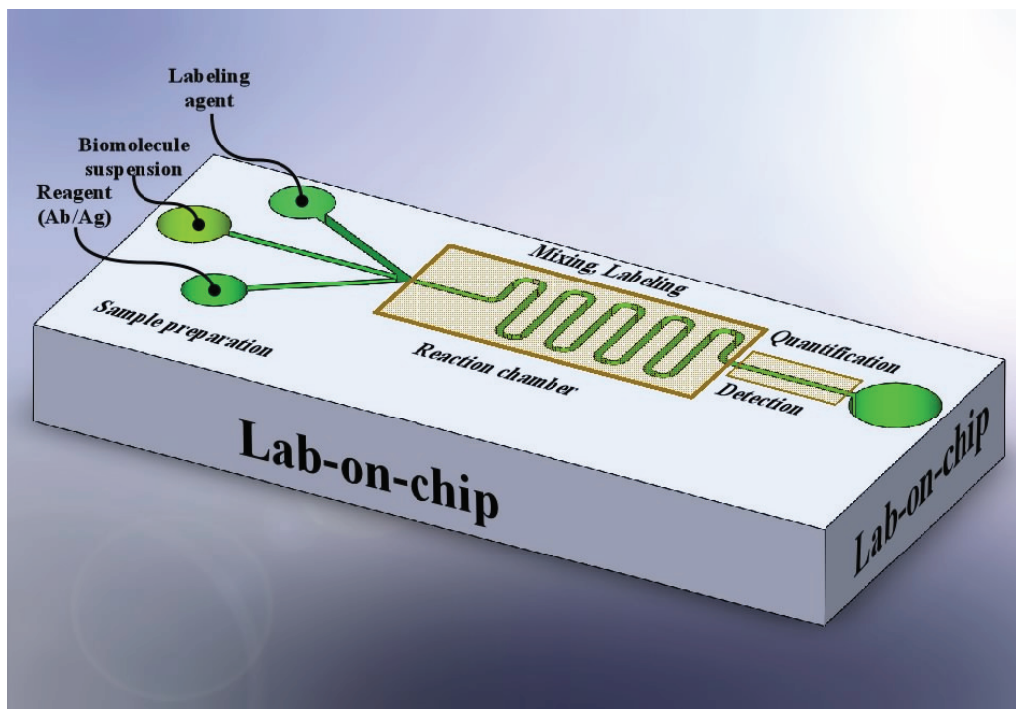


Figure 1.1: Schematic of typical Lab-on-a-Chip (LOC) device

screened. This typically occurs for biomolecular solution, where the solution conductivity is substantially large – as a result in presence of the applied electric field the biomolecules are transported due to their own electrophoretic motion and there is no influence of electroosmotic advection. Similarly, for other non-mechanical means of transport the advantages obtained by employing a transport without a non-moving part is often compensated with other difficulties intrinsic to the very nature of the transport. More importantly, for all such transport, commencement of flows requires external equipments for the actuation of the necessary driving field (electric, magnetic, or acoustic), which in turn requires the additional equipments and the complex fabricating steps. This not only increases the cost of the device but also the self sustained LOC device can not be obtained, neither can they be applied to real life applications on account of the entire set up becoming extremely cumbersome.

Hence, non-mechanical pumping approaches without any moving components have been introduced.

The intrinsic difficulties associated with the microfluidic devices with ex-

ternal actuation have motivated design and implementation of self-actuated microfluidic systems without any external actuations. These systems are also devoid of any cumbersome connectors and are considered as ideal microfluidic systems (Juncker et al., 2002), where the flow is autonomously generated with passive pumping (Walker and Beebe, 2002) by controlling channel geometries, surface chemistry, and physical properties of the fluid (e.g., surface tension). The passive pumping has several advantages such as operational simplicity, portability, and suitability for handling multiple biological species (since the denaturation of biomolecules, typical in electroosmotic flows, can easily be avoided). The terminology of *passive pumping* for microfluidic devices has been first introduced in 2002 by Beebe and Walker (K. Young and Beebe, 2010; Walker and Beebe, 2002). Further, the passive pumping in LOC devices has successfully been attempted for different biomedical applications for immunoassay (Hosokawa et al., 2006; Juncker et al., 2002), plasma extraction (Sollier et al., 2009), microsphere arrangement (Randall and Doyle, 2005), cell culture (Meyvantsson et al., 2008), protein production (Khnouf et al., 2009), enzyme sensing (Chen and Lindner, 2009), stable concentration gradient generation (Gao et al., 2012), (Gervais and Delamarche, 2009; Zimmermann et al., 2007) etc. Overview of such passive pumping based microfluidic devices can be found elsewhere (Sollier et al., 2009). There are, however, certain challenges associated with the passive pumping – for example, it is difficult to generate a continuous flow (with uniform flow rate) with passive pumping, and efforts are being made to overcome this difficulty (Berthier and Beebe, 2007; Lynn and Dandy, 2009).

As the size of the devices decrease, the large surface-to-volume ratio makes the surface forces dominant. Transporting liquid in microfluidic channels by the use of capillary action demonstrates a typical example where such dominant surface effects can be utilized to ensure passive pumping (Walker and Beebe, 2002). The state of the art on the subject performs the analysis of such capillary transport with several simplified assumptions, which may not always hold true for micro-scale geometries. Moreover, in capillary flow, wet-

ting properties of the transporting liquid decide the capability of the pumping, i.e. passive pumping and the change in the wetting properties due to inclusion of different suspensions or biomolecules is also neglected in most of the reported studies. As the traditional theory predicts, the fluid transport with capillarity always attains the steady state due to the balance among the driving capillary pressure, and retarding viscous and gravity forces. For maintaining the continuous flow with constant flow rate is also another challenging task in the capillary flow. Hence, it is necessary to explore the several other passive or non-mechanical pumping approaches combination with the capillary flow for enhancement in the pumping capability.

1.2 Objective

Objective of the present research has been the development of passive and non-mechanical pumping mechanisms for LOC devices. The rationale for this study is to investigate the scope of passive and non-mechanical pumping like capillary, gravity assisted capillary, electrokinetic (or a combination of these mechanisms) in microfluidic devices. Individual role of these mechanisms in driving the flow in a microchannel is well known; however a combination of them and their effect on the microfluidic transport has been grossly overlooked in the literature.

1.3 Outline of thesis

1.3.1 Thesis Contributions

The novel approaches for transport in microfluidic devices, realized by a combination of different passive and non-mechanical actuation mechanisms, are proposed in this study. These flow mechanisms have the potential to be used as an alternative of the existing conventional pumping mechanisms, and therefore will usher in important paradigms for microfluidic pumping. Theoretical background and implementation of these ideas will be elaborated in the upcoming chapters. The main contribution towards of the present thesis, clearly

distinguishable from past studies, are summarized as follow:

1. Identification of the key parameters that dictate the transport in the microfluidic device with a combined passive and non-mechanical pumping and use of these parameters for further improvement in the design
2. Proposition of a theoretical model for passive pumping using a capillary flow in a microchannel considering microscale effects
3. Investigation of the wetting properties of microbead and biomolecule solutions to regulate the passive pumping capabilities
4. Exploring the potential of combination of passive and non-mechanical pumping for transport of biomolecules

1.3.2 Thesis Outline

The guidelines from the Faculty of Graduate Studies and Research (FGSR) at the University of Alberta have been followed to prepare the thesis and this thesis is arranged as follows:

This thesis contains the analysis of passive and non-mechanical pumping approaches. In view of the proposed motivation, the first phase of the work deals with the theoretical background of passive (capillary transport) and non-mechanical (electrokinetic transport) pumping. Further, the impact of wetting properties of the working fluid containing microbeads and biomolecules is well understood. Finally, the combination of passive and non-mechanical pumping is also presented.

Chapter 2 emphasizes the comprehensive theoretical modeling of the capillary flow with different aspects which are considered in the literature with simplified assumptions.

Chapter 3 provides the detailed procedure for the derivation of the pressure field at the entrance of the rectangular microchannel of high aspect ratio.

Chapter 4 presents the empirical expressions for the variations in the contact angle and surface tension of microbead suspension with the change in the microbead volume fraction.

Chapter 5 is the extension of Chapter 4 where the the variations in the contact angle and surface tension of Bovine Serum Albumin (BSA) solution with the change in the concentration of BSA is presented.

Chapter 6 shows the effect of microbead presence in the carrier fluid on the capillary transport along with the demonstration of use of additional gravity head along with the capillary transport.

Chapter 7 presents the enhancement in the capillary flow pumping by coupling it with the non-mechanical pumping approaches like electroosmotic flow.

Finally, Chapter 8 draws the conclusion with important observations along with the future scope with recommendation based on the outcome of the performed research.

References

- Berthier E. and Beebe D. J., Flow rate analysis of a surface tension driven passive micropump. *Lab on a Chip - Miniaturisation for Chemistry and Biology*, 7(11):1475–1478, 2007.
- Chen I.-J. and Lindner E., Lab-on-chip flow injection analysis system without an external pump and valves and integrated with an in line electrochemical detector. *Analytical Chemistry*, 81(24):9955–9960, 2009.
- Gao Y., Sun J., Lin W.-H., Webb D. J., and Li D., A compact microfluidic gradient generator using passive pumping. *Microfluidics and Nanofluidics*, 12(6):887–895, 2012.
- Gervais L. and Delamarche E., Toward one-step point-of-care immunodiagnos-
tics using capillary-driven microfluidics and PDMS substrates. *Lab on a
Chip - Miniaturisation for Chemistry and Biology*, 9(23):3330–3337, 2009.
- Hosokawa K., Omata M., Sato K., and Maeda M., Power-free sequential
injection for microchip immunoassay toward point-of-care testing. *Lab on a
Chip - Miniaturisation for Chemistry and Biology*, 6(2):236–241, 2006.
- Juncker D., Schmid H., Drechsler U., Wolf H., Wolf M., Michel B., de Rooij N.,
and Delamarche E., Autonomous microfluidic capillary system. *Analytical
Chemistry*, 74(24):6139–6144, 2002.
- Karniadakis G., Beskok A., and Aluru N., *Microflows and Nanoflows Funda-
mentals and Simulation*. Springer Berlin, New York, 2005.
- Khnouf R., Beebe D. J., and Fan Z. H., Cell-free protein expression in a

- microchannel array with passive pumping. *Lab on a Chip - Miniaturisation for Chemistry and Biology*, 9(1):56–61, 2009.
- Lynn N. S. and Dandy D. S., Passive microfluidic pumping using coupled capillary/evaporation effects. *Lab on a Chip - Miniaturisation for Chemistry and Biology*, 9(23):3422–3429, 2009.
- Meyvantsson I., Warrick J. W., Hayes S., Skoien A., and Beebe D. J., Automated cell culture in high density tubeless microfluidic device arrays. *Lab on a Chip - Miniaturisation for Chemistry and Biology*, 8(5):717–724, 2008.
- Nguyen N. and Wereley S., *Fundamentals and Applications of Microfluidics*. Artech House, New York, 2003.
- Randall G. C. and Doyle P. S., Permeation-driven flow in poly(dimethylsiloxane) microfluidic devices. *Proceedings of the National Academy of Sciences of the United States of America*, 102(31):10813–10818, 2005.
- Sollier E., Rostaing H., Pouteau P., Fouillet Y., and Achard J.-L., Passive microfluidic devices for plasma extraction from whole human blood. *Sensors and Actuators, B: Chemical*, 141(2):617–624, 2009.
- Stone H. A., Stroock A., and Ajdari A., Engineering flows in small devices: Microfluidics toward a lab-on-a-chip. *Annual Review of Fluid Mechanics*, 36:381–411, 2004.
- Walker G. M. and Beebe D. J., A passive pumping method for microfluidic devices. *Lab on a Chip - Miniaturisation for Chemistry and Biology*, 2(3):131–134, 2002.
- Young E. W. and Beebe D. J., Fundamentals of microfluidic cell culture in controlled microenvironments. *Chemical Society Reviews*, 39(3):1036–1048, 2010.

Zimmermann M., Schmid H., Hunziker P., and Delamarche E., Capillary pumps for autonomous capillary systems. *Lab on a Chip - Miniaturisation for Chemistry and Biology*, 7(1):119–125, 2007.

Chapter 2

A comprehensive theoretical model of capillary transport in rectangular microchannels ¹

2.1 Introduction

Microfluidic channels are integral components of a Lab-on-a-Chip (LOC) devices. Transport of biomolecules, particles or chemicals of interest within these microchannels is an important requirement which has been achieved by several traditional or conventional pumping mechanisms. However, in most of the mechanisms till date, pumping has been actuated by external actuations, which are an additional burden on the system. Most commonly, transport is obtained with pressure driven flow by actuating a mechanical pump. However, due to large surface forces at micro-scale, a very high pressure drop is required for the transport of the working fluid. Hence, non-mechanical pumping approaches like electrokinetic and electromagnetic pumping have been introduced (Karniadakis et al., 2005; Nguyen and Wereley, 2003). Commencement of such flows requires external equipments to actuate of electrical and magnetic fields, which in turn requires additional complex fabricating steps for the device. In such external microscopic actuators and connectors with electromechanical interface restricts the flexibility of the devices. Moreover, electroviscous effects have to be included with other significant effects (Phan

¹A version of this chapter has been published. Waghmare and Mitra, 2012, *Microfluidics and Nanofluidics*, 12 (1-4), 53-63

et al., 2009). Attempts are being made to establish flow without any external means i.e., autonomous flow. The fluid transport can be achieved by controlling channel geometries, surface chemistry, and physical properties of the fluid like surface tension. Such pumping approach is widely termed as autonomous or passive pumping which would be an ideal mechanism of transport for microfluidic devices (Juncker et al., 2002; Zimmermann et al., 2007). As the size of the device decreases, the large surface to volume ratio makes surface forces dominant, particularly the force due to capillarity-induced pressure is very high as compared to other forces (Eijkel and van den Berg, 2006). Attempts are also being made to pump the fluid with capillary flow in closed end nanochannels (Phan et al., 2010; Radiom et al., 2010). Hence, the use of surface forces to transport the liquid with capillary action is becoming a popular option in microfluidic devices (Walker and Beebe, 2002) and have attracted special attention at micro (Waghmare and Mitra, 2010) (Waghmare and Mitra, 2010b,c), meso (Diotallevi et al., 2009; Zhang, 2011) and molecular level (Dimitrov et al., 2007).

Theoretical understanding of capillarity has been conducted over the past century. Through the theoretical investigations, temporal variation in the position of the flow front along the length of the capillary is predicted. The position of the flow front from the capillary inlet is generally termed as penetration depth. Two distinct modeling approaches are reported in the literature. In the first approach, the closed form expression for the transient variation in the penetration depth is proposed which is similar to Washburn approach (Washburn, 1921). Whereas, in the second approach, the differential equation in terms of penetration depth is obtained which encompasses all possible forces present during the penetration of the flow front (Levine et al., 1976). The penetration depth with the first approach is predicted without considering the viscous and inertial effects and therefore to include such effects, the second approach has been developed (Levine et al., 1980). Further, the final governing equation for the capillary penetration is obtained by applying differential (Levine et al., 1980) or integral (Dreyer et al., 1993) momentum equation. Washan-

burn (Washburn, 1921) has reported the close form solution for the entrance length, which emphasizes that the steady state velocity assumption is a valid assumption for capillary flow analysis. A microscopic energy balance is used by Newman (Newman, 1968) and Szekely (Szekely et al., 1971), as opposed to the quasi-steady state approximation of Washburn (Washburn, 1921) and they claimed that, the Washburn approach (Washburn, 1921) can not be used for short capillary transport. Further Saha and Mitra (Saha and Mitra, 2009b) demonstrated numerically and experimentally (Saha et al., 2009) that Washburn prediction deviates for micro-scale geometries. Moreover, Saha and Mitra (Saha and Mitra, 2009a) have performed the numerical simulation of capillary filling process in a pillared microfluidic geometry and reported that variation in the capillary filling length does not follow the Washburn equation. Dreyer et al. (Dreyer et al., 1994) have also quantified the capillary flow behavior according to the penetration depth variations with respect to the time. In such analysis, the governing equation for penetration depth is obtained by balancing various forces viz., the entrance pressure force, the surface or the pressure force at the interface, the viscous and the gravity forces with the inertial and transient terms in the momentum equation. The viscous force, inertial, and convective terms in the momentum equation depend on the velocity profile across the channel. Whereas, other forces are function of the fluid properties, as reported in a recent modeling effort (Waghmare and Mitra, 2010c). In such analysis, the velocity dependent terms are determined by assuming a fully developed i.e., parabolic velocity profile across the channel.

The assumption of the parabolic velocity profile is a valid assumption for steady state conditions. In case of the transient flow, several researcher have used the assumption of parabolic velocity profile (Dreyer et al., 1994; Chakraborty, 2007; Dreyer et al., 1993; Levine et al., 1976, 1980; Newman, 1968; Szekely et al., 1971; Washburn, 1921) in their analyses. But this assumption is only valid for a high viscous fluid or very low Reynolds number flow which may not be true in all cases (Bhattacharya and Gurung, 2010). Hence, it is important to adopt a different approach for capillary flow analysis

to rectify this discrepancy. This can be achieved by considering the transient velocity profile derived from transient momentum equation. This transient velocity profile not only satisfies the transient integral momentum equation but also accounts for the time dependent term in the velocity profile. The equation which governs the capillary transport consist of two types of terms-velocity dependent and velocity independent terms. The velocity dependent terms can be determined using transient velocity profile and further transient effects can be analyzed by comparing the results with the steady state velocity profile.

The velocity independent terms in the momentum equation are force terms except the viscous force viz.; pressure forces at the inlet of the microchannel and at the air-fluid interface. The pressure field at the air-fluid interface can be calculated using Young-Laplace equation. On the other hand, Levine (Levine et al., 1976) proposed the pressure field at the inlet of the microchannel, different from the common notation of an atmospheric pressure typically applied at the entrance of the microchannel. In their study, they have proposed the pressure field expression for circular capillary. Several researchers have extended this circular capillary expression for non-circular capillaries with equivalent radius assumption. The equivalent radius assumption may not be applicable for a wide range of microchannel aspect ratios. The present literature suggest that there is a lack of a pressure field expression for rectangular microchannels, which is a more common geometry based on microfabrication techniques for microfluidic devices. The authors have attempted to propose a pressure field expression at the entrance of a parallel plate arrangement (Waghmare and Mitra, 2010). The pressure field expression is developed by assuming the length of the plate is much longer than the gap between two plates, but in microfluidics applications such assumption may not be universally valid. Further, the capillary transport analysis with such modified pressure field for a rectangular microchannel is also not available in the literature. Therefore, it is necessary to determine the appropriate pressure field at the entrance of the rectangular microchannel and the effect of such pressure field expression on

the capillary flow analysis needs to be studied, which is performed in the later part of this study.

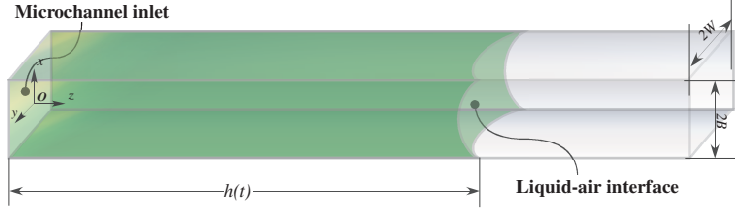
A generalized non-dimensional equation for capillary transport can be obtained by calculating the velocity dependent and independent, i.e., appropriate force terms. In the upcoming section, the theoretical model for capillary transport with transient velocity profile is presented. Further, a generalized non-dimensional equation with steady state and transient velocity profiles is derived and solved numerically to investigate the effect of transient velocity profile. An appropriate pressure field expression at the entrance of the rectangular microchannel is also derived in the later part of this study. Finally, the effect of such pressure field on the capillary transport is also analyzed. Hence, the analysis presented here is a comprehensive one, which provides a greater understanding of capillary transport in rectangular microchannels.

2.2 Mathematical modeling

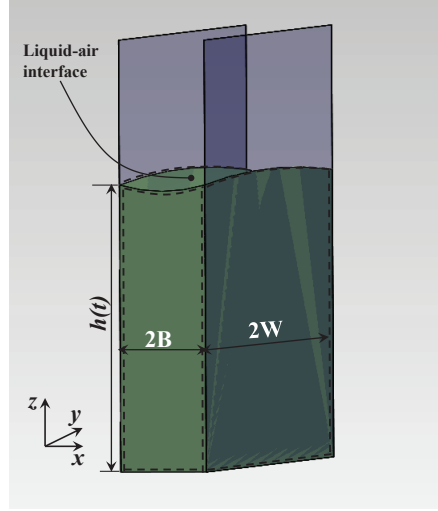
In most of the capillary flow analysis, the integral momentum equation for deformable fluid control volume along the microchannel is used (Dreyer et al., 1994, 1993; Levine et al., 1976, 1980). The integral momentum equation for the fluid transport in the microchannel of width $2B$ and depth $2W$, as shown in Fig. 2.1, can be written as,

$$\sum F_z = \frac{\partial}{\partial t} \int_0^h \int_{-W}^W \int_{-B}^B \rho v_z dx dy dz + \int_{-W}^W \int_{-B}^B v_z (-\rho v_z) dx dy \quad (2.1)$$

Here, ρ is the density of the fluid, v_z is the velocity of the capillary across the channel and h is the penetration depth or movement of the fluid flow front in the capillary. This momentum equation governs the transient response of the capillary front movement along z -axis, which is termed as penetration depth in this analysis. Here, $\sum F_z$ is the summation of all forces acting on the fluid under consideration viz., viscous (F_v), gravity ($F_g = 4\rho ghBW$), pressure



(a) Rectangular microchannel



(b) High aspect ratio microchannel

Figure 2.1: Schematic of microchannel of width $2B$ and depth $2W$ considered for the theoretical modeling of capillary transport. Figure (a) shows the rectangular microchannel where the width and depth are comparable to each other and Fig. (b) represents the high aspect ratio microchannel which is considered in this analysis. The dotted line shows the control volume considered for the analysis.

forces at the flow front (F_{pf}) and at the inlet (F_{pi}), as illustrated here:

$$\sum F_z = \underbrace{F_v}_{\text{velocity dependent}} + \underbrace{F_g + F_{pf} + F_{pi}}_{\text{velocity independent}} \quad (2.2)$$

Transient and convective terms in Eq. 2.1 and the viscous force term in Eq. 2.2 can be determined by using the velocity profile, v_z across the channel. For simplicity, fully developed Poiseuille flow is assumed in the literature (Dreyer et al., 1994; Waghmare and Mitra, 2010b; Chakraborty, 2007; Dreyer et al., 1993; Levine et al., 1976, 1980; Newman, 1968; Szekely et al., 1971; Washburn, 1921), neglecting the change in the velocity profile at the entrance region

and at the flow front. This introduces an inconsistency due to the fact that the fully developed velocity profile assumption is valid only for steady flow systems (Bhattacharya and Gurung, 2010). Thus a developing i.e., transient velocity profile instead of a developed velocity profile needs to be considered for the analysis. This can be achieved by considering the transient momentum equation for pressure driven flow with pressure drop dp/dz as depicted here,

$$\rho \frac{\partial v_z}{\partial t} = \mu \frac{\partial^2 v_z}{\partial x^2} + \frac{dp}{dz} \quad (2.3)$$

where, μ is the viscosity of the fluid. The velocity in Eq. 2.3 can be decoupled in the following manner (Keh and Tseng, 2001),

$$v_z(x, t) = v_{z\infty}(x) + v_{zt}(x, t) \quad (2.4)$$

here, $v_{z\infty}(x)$ is the velocity field at steady state, which can be written as (White, 2006),

$$v_{z\infty}(x) = \frac{B^2}{2\mu} \frac{dp}{dz} \left[1 - \left(\frac{x}{B} \right)^2 \right] \quad (2.5)$$

The transient component of the velocity can be obtained from following equation using boundary conditions of no-slip and maximum velocity at wall and center, respectively with zero velocity as an initial condition (Keh and Tseng, 2001).

$$\frac{1}{\rho} \frac{\partial v_{zt}}{\partial t} = \mu \frac{\partial^2 v_{zt}}{\partial x^2} \quad (2.6)$$

The method of separation of variable is used to obtain the solution of Eq. 2.6 and is given as,

$$v_{zt}(x, t) = 2 \sum_{n=1}^{\infty} (-1)^n \left[\frac{1}{B\mu\lambda_n^3} \frac{dp}{dz} \right] \cos(\lambda_n x) \exp(-\nu\lambda_n^2 t) \quad (2.7)$$

where, $\lambda_n = \frac{(2n-1)\pi}{2B}$ and ν is the kinematic viscosity of the fluid. Hence, the transient fluid velocity profile $v_z(x, t)$ can be obtained by combining Eq. 2.5 and 2.7.

$$v_z(x, t) = \left\{ \sum_{n=1}^{\infty} (-1)^n \frac{1}{B\mu} \left(\frac{2}{\lambda_n^3} \right) \cos(\lambda_n x) \exp(-\nu \lambda_n^2 t) + \frac{1}{2\mu} (B^2 - x^2) \right\} \frac{dp}{dz} \quad (2.8)$$

The average velocity across the channel can be expressed as,

$$v_z(x, t)_{avg} = \frac{B^2}{3\mu} \left[1 - \sum_{n=1}^{\infty} \frac{96}{(2n-1)^4 \pi^4} \exp \left[-\frac{(2n-1)^2 \pi^2 \nu t}{4B^2} \right] \right] \frac{dp}{dz} \quad (2.9)$$

As done for other capillary flow models (Newman, 1968), the pressure drop term in Eq. 2.8 is replaced by the average velocity so that the velocity profile is obtained in terms of the penetration depth,

$$v_z(x, t) = \frac{B^2}{2\mu} \alpha_1 \left\{ \sum_{n=1}^{\infty} (-1)^n \left[\frac{4}{(B\lambda_n)^3} \right] \cos(\lambda_n x) \exp(-\nu \lambda_n^2 t) + \left(1 - \frac{x^2}{B^2} \right) \right\} \times \left\{ \frac{1}{\alpha_1 [1 - \sum_{n=1}^{\infty} \beta_1 \exp(-\lambda_n^2 \nu t)]} \right\} \frac{dh}{dt}$$

where,

$$\alpha_1 = \frac{\left[(\phi)^4 - 4 \exp -\frac{\phi^2 t}{3} \right]}{\left[(\phi)^4 - 6 \exp -\frac{\phi^2 t}{3} \right]}$$

and $\phi = \lambda_n B$. The velocity dependent terms of the governing equation for capillary transport can be derived with transient velocity profile provided in Eq. 2.10. Pressure forces at the fluid-air interface within the microchannel and at the inlet of the microchannels can be determined by using respective pressure field distributions at the interface and at the inlet of microchannel. Young-Laplace equation (Washburn, 1921) with the fluid surface tension, σ and equilibrium angle, θ is used to determine the pressure at the interface. The radii of the curvature for Young-Laplace equation are $B/\cos\theta$ and W , respectively. The concept of pressure force at the entrance of the capillary was first proposed by Levine et. al (Levine et al., 1976). However, they have reported

the pressure field expression at the entrance of circular capillaries and several researcher have extended this circular capillary expression to parallel plate configuration with a simplified assumption. For parallel plate configuration, the pressure field is investigated by assuming a hemispherical control volume and the radius of the hemisphere is determined from the projected cross sectional area at the capillary entrance. The derived pressure field in such case, as used by several other researchers for rectangular capillaries like flow of liquid coolant (Dreyer et al., 1994), alcohol (Xiao et al., 2006), nanoparticulate slurry (Mawardi et al., 2008), and blood (Chakraborty, 2007), can be written as,

$$p(o, t) = p_{atm} - \left\{ 1.11\rho\sqrt{BW}\frac{d^2h}{dt^2} + 1.58\rho\left(\frac{dh}{dt}\right)^2 + \frac{1.772\mu}{\sqrt{BW}}\frac{dh}{dt} \right\} \quad (2.10)$$

To emphasize and analyze the effect of transient velocity profile, in this part of analysis the pressure field expression from existing literature (i.e.,Eq. 2.10) is used to determine the pressure force at the entrance of the microchannel. An appropriate pressure field expression for rectangular microchannel and the importance of such accurate pressure field expression are presented in the later part of this study. Finally, one can rewrite the momentum equation Eq. 2.1 incorporating the relevant forces, transient and convective terms, where the transient velocity profile is used for calculating the velocity dependent terms. Further, the non-dimensional analysis is performed which results in a generalized non-dimensional governing equation for capillary flow in microchannel which can be written as (Waghmare and Mitra, 2010c),

$$(h^* + C_1)\frac{d^2h^*}{dt^{*2}} + C_2\left(\frac{dh^*}{dt^*}\right)^2 + (C_3 + C_4h^*)\frac{dh^*}{dt^*} + C_5h^* + C_6 = 0 \quad (2.11)$$

The non-dimensional time (t^*) and the penetration depth (h^*) which are defined with respect to the characteristic time, $t_0 = \frac{\rho(2B)^2}{12\mu}$ and the characteristic length $h_0 = 2B$, respectively. Table 2.1 depicts the different constants of Eq. 2.11 for an evolving capillary transport. All coefficients are the function of the velocity profile. In non-dimensional analysis, two non-dimensional numbers are obtained i.e., Bond number(Bo) and Ohnesorge number(Oh). The

Ohnesorge number $\left(Oh = \frac{\mu}{\sqrt{2B\rho\sigma}}\right)$ represents the ratio of viscous to surface tension force, the Bond number $\left(Bo = \frac{\rho g(2B^2)}{\sigma}\right)$ dictates the ratio of gravity to surface tension force and another non-dimensional parameter, i.e., $\gamma(= B/W)$ is the aspect ratio of the microchannel, defined as the ratio of width to depth of the microchannel.

Table 2.1: Constants of the generalized non-dimensional governing equation for a capillary flow in a rectangular microchannel with a developing velocity profile

Constants	Expressions
C_1	$\frac{0.55}{\alpha_1} \sqrt{\gamma}$
C_2	$\frac{\alpha_1}{1.158 + \alpha_1}$
C_3	$\frac{1}{3\alpha_1 \left[\phi^4 - 6e^{-\frac{\phi^2 t^*}{3}} \right]}$ $\times \left[\phi^6 (1 - \alpha_1) - 4\phi^2 e^{-\frac{\phi^2 t^*}{3}} + 3\phi^4 \right]$
C_4	$\frac{0.295 \sqrt{\gamma}}{\alpha_1}$
C_5	$\frac{144\alpha_1 Oh^2}{Bo}$
C_6	$\frac{\gamma - \cos \theta}{72\alpha_1 Oh^2}$

Equation 2.11 is obtained on the basis of the following assumptions:

- (i) The liquid is homogeneous, incompressible, and Newtonian and the capillary flow is studied at a constant temperature.
- (ii) The change in the interface shape, i.e., dynamic variations in the contact angles during the capillary filling process are neglected.
- (iii) The depth ($2W$) is assumed to be much larger than the width ($2B$) of the microchannel.

2.3 Effect of developing velocity profile in capillary transport

It is important to analyze the importance of such transience in velocity during the capillary transport. The variation in the penetration depth with the steady state and unsteady state velocity profile are presented in Figs. 2.2 and

2.3. The bottom left inset of Fig. 2.2 shows penetration depth variations at the beginning of the transport and the attainment of the equilibrium penetration depth is shown in the upper right inset. The equilibrium penetration depth is the length along the microchannel for which the flow front attains a zero velocity. In this analysis, the development of velocity profile from unsteady to steady state is accounted with a developing i.e., transient velocity profile. At the beginning of the channel filling process, the velocity is undeveloped therefore, the magnitude of the penetration depth is smaller than the penetration depth with the developed velocity profile. The lower bottom inset of Fig. 2.2 suggests that within the first $10ms$, there is a difference of $5mm$ in the penetration depth, which has important implications in terms of controlling chemical reactions, antigen-antibody binding, and other bio-MEMS applications. As the flow front approaches towards the equilibrium penetration depth, the transient velocity profile attains the steady state and the quantitative difference in the penetration depth is negligible as depicted in the upper right inset of the Fig. 2.2.

The effect of transient velocity profile with the change in the fluid properties is depicted in Fig. 2.3. For a highly dense and viscous fluid, the effect of transience in the velocity profile is qualitatively same as observed in the previous case. Figure 2.3(a) shows the penetration depth variation with highly dense ($Bo = 0.01$) fluid whereas, similar variations are observed for highly viscous fluid in Fig. 2.3(b). The inset of both the figures shows the enlarged views of the penetration depths with two velocity profiles. The equilibrium penetration depth with a high density fluid is smaller than penetration depth with high viscous fluid. In case of high viscous fluid, a longer time is required to attain the same equilibrium penetration as compared to the case shown in Fig. 2.2. It is important to quantify the difference in penetration depths, even though it may seem to be small, due to the transience in the velocity profiles. Therefore, the difference in the penetration depths with developed and developing velocity profiles for the same time instant is calculated and the

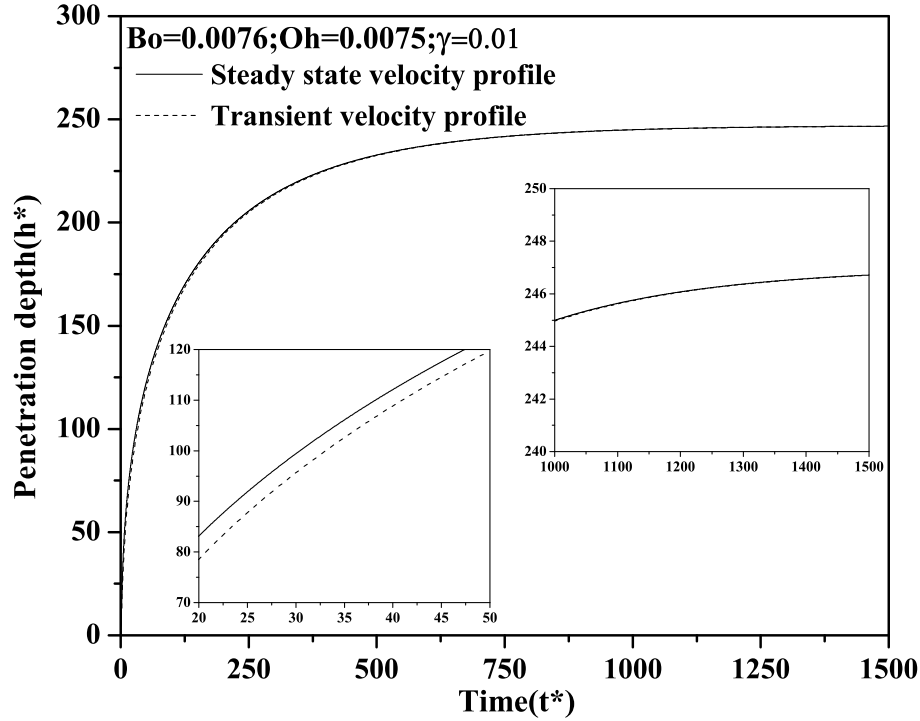
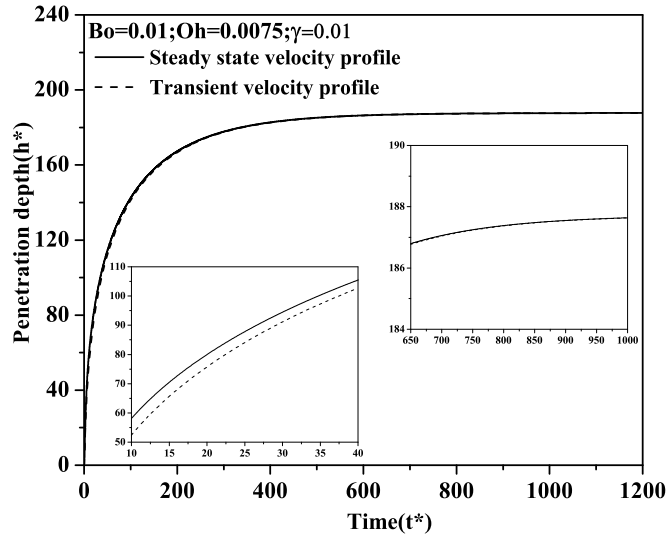
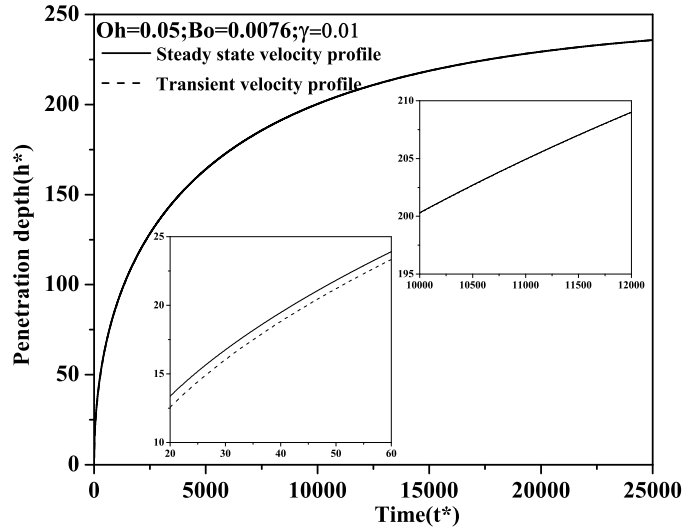


Figure 2.2: Transient response of penetration depth with fully developed (steady state) and developing (unsteady) velocity profile

percentage change in the penetration depth is presented in Fig. 2.4. In this particular case study, the comparison in penetration depths of previous three cases (Figs. 2.2 and 2.3) is presented. The enlarged view in the inset shows that the penetration depth with transient velocity profile deviates up to 16% from the penetration depth value with steady state velocity profile. The boundary layer formation is the effect of no slip at the wall which propagates across the channel and the rate of propagation is decided by the physical properties of fluid, particularly the fluid viscosity. As the viscosity of fluid increases, the boundary layer thickness also increases, which results in retardation of flow within the boundary layer. The density has an opposite effect (Schlichting, 1968). It is observed that for a high viscosity fluid, the percentage difference in the penetration depth is lower (8%) as compared to the difference with the high



(a) Penetration depth variation for fluid with $Bo = 0.01$



(b) Penetration depth variation for fluid with $Oh = 0.05$.

Figure 2.3: Transient response of penetration depth with fully developed (steady state) and developing (unsteady) velocity profile for highly dense and viscous fluid. In both the figures bottom left inset shows the variation in the penetration depth at the beginning of the transport and upper right inset shows the variations in the penetration depth during the attainment of the equilibrium penetration depth.

density fluid (16%). Thus, it can be concluded that the fully developed velocity profile assumption needs to be used carefully in the capillary analysis. It is stated in the literature that (Bhattacharya and Gurung, 2010), the approximation of steady state velocity is a valid assumption for low Reynolds number flows like a creeping flow. Also literature suggests that, the surface driven flow can be considered as a creeping flow and hence the simplified fully developed velocity profile can describe the velocity field across the microchannel in case of a capillary transport. Here, the quantified difference in penetration depth due to such assumption is presented and observed that at the beginning of the capillary transport the transience in the velocity plays a significant role. At micro-scale, such effects need to be considered carefully before designing microfluidic devices particularly for devices, with capillary transport.

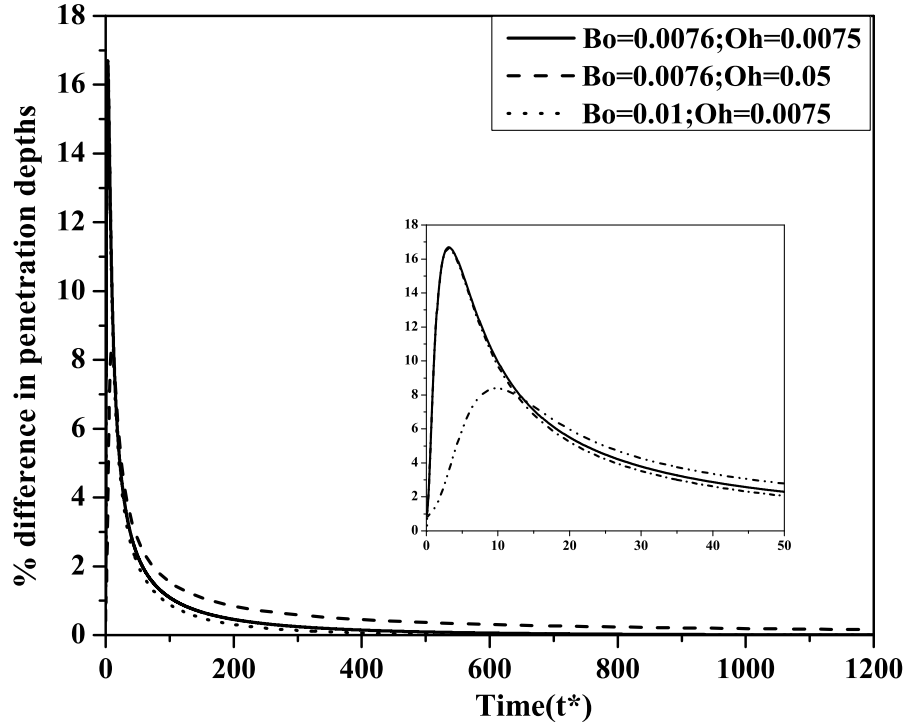


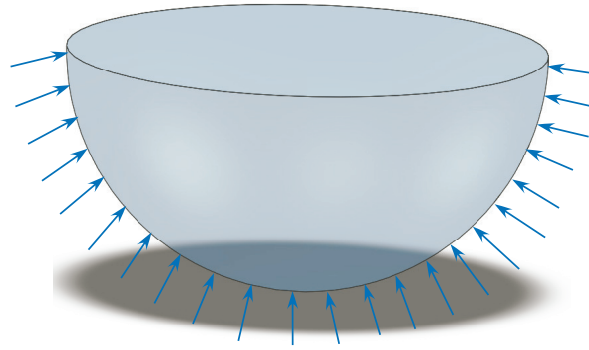
Figure 2.4: Transient response in the difference in the penetration depths with fully developed (steady state) and developing (unsteady) velocity profile under different conditions.

As mentioned earlier, apart from the velocity profile across the microchannel, the pressure field at the inlet of the microchannel is another aspect, which has been considered with some degree of approximation in the existing literature. It is necessary to derive the appropriate pressure field at the entrance of a rectangular microchannel. Therefore, in the next section, the pressure field for a rectangular microchannel is derived. Moreover, the penetration depth with the proposed and approximated pressure field from literature is compared to analyze the importance of the proposed pressure field.

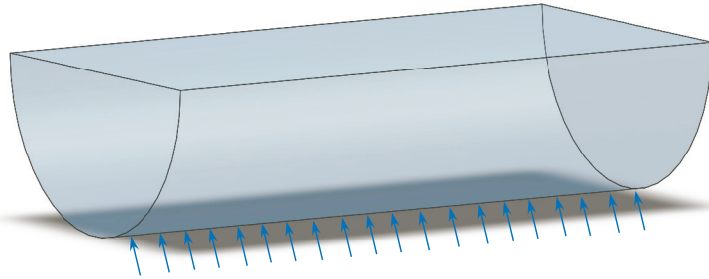
2.4 Pressure field at the entrance of the microchannel

As explained in Section 2.2, the force at the capillary entrance is calculated using the pressure field at the entrance of the capillary. Levine et al. (Levine et al., 1976) reported that the pressure at the entrance of the microchannel is different than the atmospheric pressure. A separate control volume, as shown in Fig. 2.5, at the entrance of the capillary, in addition to the deformable control volume along the microchannel, has been considered for the derivation of the pressure field. A well defined control volume at the entrance, such as a hemispherical fluid volume shown in Fig. 2.5(a), within a large volume of a fluid in contact with capillary is responsible for defining the pressure field at the inlet. For a circular capillary, Levine et al. (Levine et al., 1976) has taken a hemispherical control volume of radius equal to that of the capillary. The velocity components in the hemispherical control volumes are determined and further the momentum balance to the fluid flow in the control volume is applied to calculate the pressure field.

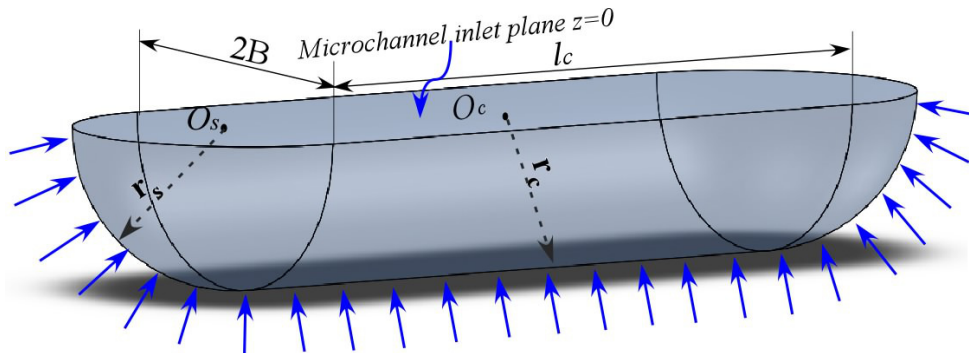
The classical expression proposed for circular capillary has been extended by several researchers for capillaries of different geometries like, parallel plates (Dreyer et al., 1993). In parallel plate arrangement, a hemispherical control volume in the reservoir is assumed, as done by Levine et al. (Levine et al.,



(a) Control volume for circular capillary (Levine et al., 1976)



(b) Control volume for parallel plate arrangement (Waghmare and Mitra, 2010)



(c) Control volume for rectangular microchannel with high aspect ratio

Figure 2.5: The fluid volume from infinite reservoir considered as control volume for pressure field expression analysis. Figure 2.5(a) is the control volume considered for circular capillary, Fig. 2.5(b) represents the appropriate control volume for parallel plate arrangement and for rectangular microchannel Fig. 2.5(c) is the appropriate control volume. Arrow shows the direction of the fluid flow from the reservoir into the microchannel.

1976). The radius of this hemisphere is calculated by equating the projected area of hemisphere to the cross sectional area at the entrance of the paral-

lel plates (Dreyer et al., 1993). Several other researchers have adopted this concept of equivalent radius and performed the capillary flow analysis in rectangular microchannels (Dreyer et al., 1994; Chakraborty, 2007; Mawardi et al., 2008; Xiao et al., 2006). The concept of equivalent radius with an assumption of hemispherical control volume is not a realistic representation of the entrance region in non-circular geometries. For high aspect ratio channels (width \ll depth), the region for the fluid volume or the appropriate control volume for the analysis can not be considered as a hemisphere. For non-circular geometries e.g., rectangular microchannels, a separate shape for the control volume needs to be considered. For the parallel plate arrangement, authors have earlier derived the pressure field expression which only depends on the gap between the two plates and is independent of the depth of the plates (Waghmare and Mitra, 2010). It is necessary to derive the appropriate expression for pressure field with an appropriate control volume at the entrance of non-circular microchannels. In the upcoming section, the appropriate control volume is considered and the pressure field at the entrance of non-circular microchannel is derived.

2.4.1 Pressure field at the entrance of non-circular microchannels

Figure 2.5 shows a representative control volume for different capillary geometries (circular, parallel plate and rectangular), which acts as a fluid source mimicking a sink flow at the microchannel entrance. Further, the same control volume is used for the derivation of the entrance pressure field expression. In the literature, for a circular capillary a hemispherical control volume is assumed (Levine et al., 1976), and for parallel plate arrangements, the semi-cylindrical control volume is considered (Waghmare and Mitra, 2010), as shown in Figs. 2.5(a) and 2.5(b), respectively. It is also assumed that, the control volume at the entrance of capillary aligns with the microchannel at the entrance. In case of rectangular microchannels, neither the hemispherical nor the semi-cylindrical control volume is an appropriate control volume for the

analysis. The hemispherical control volume represents the axi-symmetric sink flow at the entrance whereas, in case of semicylindrical shape(Fig. 2.5(b)), the flow along the length of a semicylinder is considered. Further, in case of a semicylindrical control volume, the fluid volume contained at the two ends of the semicircular cylinder is neglected. This might be a valid assumption for very high aspect ratio microchannels, where the microchannel can be treated as parallel plates for the analysis. But for moderate aspect ratio microchannels, like rectangular microchannels, which are generally used in microfluidic applications, the fluid volumes at the two ends of the semicircular cylinder need to be incorporated. Hence, it is necessary to consider a different shape for the control volume representing rectangular microchannels. Therefore, to account such effects, the combination of the cylindrical and the spherical control volumes, as depicted in Fig. 2.5(c), is considered as an appropriate control volume for the analysis. For the rectangular microchannel of aspect ratio γ , which is the ratio of width to depth of the microchannel, the control volume shown in Fig. 2.5(c) is an appropriate control volume. A cylindrical and a spherical co-ordinate system with origin O_c and O_s , respectively, are considered for cylindrical and spherical regions. One can determine the radial velocity in the corresponding regions by applying the continuity equation to the control volumes. The origin O_c of cylindrical region coincides with the origin of the microchannel at the inlet plane. It is assumed that, v_r is the radial velocity components for both the coordinates.

As mentioned earlier, $\frac{dh}{dt}$ is the penetration rate along the microchannel. The flux of volume in the direction of the capillary flow from the reservoir can be calculated using continuity equation as follow,

$$v_{rc}r_c\pi l_c + 2\pi v_{rs}r_s^2 = -4BW\frac{dh}{dt} \quad (2.12)$$

Here, l_c represents the length of cylindrical control volume. In this analysis, the subscripts c and s are used to represent the cylindrical and spherical regions. From Eq. 2.12 one can deduce the radial velocity component from cylindrical and spherical regions as,

$$v_{r_s} = -\frac{2BW}{\pi r_s^2} \frac{dh}{dt} - \frac{v_{r_c} r_c l_c}{2r_s^2} \quad (2.13)$$

$$v_{r_c} = -\frac{4BW}{\pi r_c l_c} \frac{dh}{dt} - \frac{2v_{r_s} r_s^2}{r_c l_c} \quad (2.14)$$

Now, the pressure field in the radial direction can be determined using the momentum equation in the radial direction. The momentum equation can be written as,

$$\rho \left\{ \frac{\partial v_{r_c}}{\partial t} \right\} = -\frac{\partial p}{\partial r_c} + \mu \left\{ \frac{\partial}{\partial r_c} \left(\frac{1}{r_c} \frac{\partial}{\partial r_c} [r_c v_{r_c}] \right) \right\} \quad (2.15)$$

Using Eq. 2.14 the pressure field in the cylindrical region of the control volume can be expressed as,

$$p(r_c, t) = p_{atm} - \frac{4\rho BW}{\pi l_c} \left(\ln \frac{r_\infty}{r_c} \right) \frac{d^2 h}{dt^2} \quad (2.16)$$

Here, r_∞ is the radial distance far away from the inlet of the microchannel outside the cylindrical region where, the pressure $p(r_c, t)$ approaches to atmospheric pressure p_{atm} and capillary force becomes negligible. Following the same approach, the pressure field for the two end regions i.e., for the spherical domain is given by,

$$p(r_s, t) = p_{atm} - \frac{2BW \rho}{\pi r_s} \frac{d^2 h}{dt^2} \quad (2.17)$$

The velocity field within the control volume is unknown which is necessary to determine the pressure field at the entrance of the microchannel. Such velocity field can be computed by considering the momentum balance which suggests, that the rate of change of total momentum in the control volume is equal to the combination of the net momentum flux and forces acting on the surface of the control volume.

Two major forces are acting on the control volume shown in Fig. 2.5(c); the first one is along the surface of the entire control volume and another one is at the inlet of the microchannel. These forces are determined by calculating the momentum flux and rate of change of momentum within the control

volume. Forces acting along the surface at $r_c = B$ and $r_s = B$ in the direction of capillary flow can be determined by using the stress tensor in the radial direction. The forces on both the surfaces are calculated separately. Using Eqs. 2.14 and 2.16, the stress tensor along the surface of cylindrical region in the radial direction is,

$$\sigma_{r_c, r_c}|_{r_c=B} = -p_{atm} + \frac{2\rho B}{\pi(1-\gamma)} \left(\ln \frac{R_\infty}{B} \right) \frac{d^2h}{dt^2} + \frac{4\mu}{\pi B} \frac{dh}{dt} \quad (2.18)$$

Similarly, using Eqs. 2.13 and 2.17, the stress tensor for the spherical region is,

$$\sigma_{r_s, r_s}|_{r_s=B} = -p_{atm} + \frac{2\rho W}{\pi} \frac{d^2h}{dt^2} + \left(\frac{8\mu}{\pi B} \right) \frac{(2-\gamma)}{\gamma} \frac{dh}{dt} \quad (2.19)$$

From Eqs. 2.18 and 2.19, the total force acting on the surface of the control volume in the direction of the capillary transport is,

$$F_{r=B} = [2\pi B^2 + 4BW(1-\gamma)] p_0 - 4\rho B^2 W \left[1 - \frac{2}{\pi} \ln \frac{R_\infty}{B} \right] \frac{d^2h}{dt^2} - 16\mu W \left[(2-\gamma) + \frac{(1-\gamma)}{\pi} \right] \frac{dh}{dt} \quad (2.20)$$

The other force acting in the direction of the capillary transport from the same control volume is the force at the inlet of the microchannel, i.e., at the plane $z = 0$. This can be calculated as,

$$F_{z=0} = - \int_{-W}^W \int_{-B}^B p(0, t) dx dy \quad (2.21)$$

The total rate of change of momentum within the control volume can be calculated with the instantaneous acceleration within the system. It is difficult to determine the instantaneous acceleration within the system therefore, the mean of accelerations at the curvature of control volume and at the inlet of the microchannel are calculated.

The rate of change of momentum is the product of the mass of the control volume and the total acceleration across the control volume (Levine et al., 1976). The total acceleration can be determined by calculating the acceleration flux within the control volume and the volume flux along the microchannel.

The total acceleration flux at $r = B$ is,

$$4BW \frac{dh}{dt} \left\{ \left[\frac{1}{\pi} + \frac{4}{\pi^2} \right] \frac{d^2h}{dt^2} + \left[\frac{4(2-\gamma)}{B\pi^2} - \frac{8(1-\gamma)}{\pi^3\gamma W} \right] \left(\frac{dh}{dt} \right)^2 \right\} \quad (2.22)$$

which is the combination of acceleration flux at $r_c = B$ and $r_s = B$. The volume flux along the rectangular microchannel can be given as, $4BW \frac{dh}{dt}$.

Using the expression Eq. 2.22 and in conjunction with the volume flux along the rectangular microchannel, the mean acceleration at $r = B$ can be written as,

$$a_{mean_{r=B}} = \left[\frac{1}{\pi} + \frac{4}{\pi^2} \right] \frac{d^2h}{dt^2} + \left[\frac{4(2-\gamma)}{B\pi^2} - \frac{8(1-\gamma)}{\pi^3\gamma W} \right] \left(\frac{dh}{dt} \right)^2 \quad (2.23)$$

Similarly, the mean acceleration at the entrance of the microchannel is (Levine et al., 1976),

$$a_{mean_{z=0}} = \frac{6}{5} \frac{d^2h}{dt^2} \quad (2.24)$$

The mean acceleration of the control volume can be determined by the calculating the average of the mean accelerations over $r = B$ and $z = 0$. Therefore, the rate of change of total momentum can be expressed as,

$$2\pi\rho B^2W \left[\frac{2\gamma + 6(\gamma - 1)}{3} \right] \left\{ \left[\frac{1}{2\pi} + \frac{1}{\pi^2} + \frac{6}{5} \right] \frac{d^2h}{dt^2} + \left[\frac{4(2-\gamma)}{B\pi^2} + \frac{4(1-\gamma)}{\pi^3\gamma W} \right] \left(\frac{dh}{dt} \right)^2 \right\} \quad (2.25)$$

One also needs to find out the total momentum flux across the surface of the control volume. The momentum flux across the curvature is the combination of the flux across the cylindrical and the spherical regions, which can be written as:

$$\dot{M}_{r=B} = \frac{4\rho B^2}{\pi} \left[1 + \frac{4(1-\gamma)}{\gamma\pi} \right] \left(\frac{dh}{dt} \right)^2 \quad (2.26)$$

Eq. 2.26 shows the momentum flux across the curvature. The momentum flux at the microchannel entrance ($z = 0$) is given by (Levine et al., 1976),

$$\dot{M}_{z=0} = \frac{24\rho BW}{5} \left(\frac{dh}{dt} \right)^2 \quad (2.27)$$

Finally, one can write the momentum balance for the control volume using Eqs. 2.20, 2.21, 2.23, 2.25, 2.26 and 2.27 and by rearranging the terms, the pressure field expression for rectangular microchannel is,

$$\begin{aligned} p(0, t) = p_{atm} - \rho B \left\{ \left[\frac{4\gamma + 3(1-\gamma)}{24} \right] \left\{ \pi \left[\frac{1}{2\pi} + \frac{2}{\pi^2} + \frac{6}{10} \right] \right\} \right. \\ \left. + \left[1 - \frac{2}{\pi} \ln \frac{R_\infty}{B} \right] \right\} \frac{d^2 h}{dt^2} \\ + \rho \left\{ \left[\frac{4(1-\gamma)}{\pi^2} - \frac{6}{5} \right] - \left[\frac{4\gamma + 3(1-\gamma)}{6} \right] \left[\frac{(2-\gamma)}{2\pi} - \frac{(1-\gamma)}{\pi^2} \right] \right\} \left(\frac{dh}{dt} \right)^2 \\ - \frac{4\mu}{B} \left[(2-\gamma) + \frac{(1-\gamma)}{\pi} \right] \frac{dh}{dt} \end{aligned}$$

In Eq. 2.28 by substituting $\gamma = 1$, one can readily find the pressure field at the inlet of a square capillary, which can be written as,

$$\begin{aligned} p(0, t) = p_{atm} - \rho B \left\{ \frac{13}{12} + \frac{1}{3\pi} + \frac{\pi}{10} \right\} \frac{d^2 h}{dt^2} \\ - \rho \left\{ \frac{6}{5} + \frac{1}{3\pi} \right\} \left(\frac{dh}{dt} \right)^2 - \frac{4\mu}{B} \frac{dh}{dt} \end{aligned} \quad (2.28)$$

Another limiting case is when the length of the channel is very large compare to its width, i.e., $\gamma \rightarrow 0$, for which the pressure field can be written as,

$$\begin{aligned} p(0, t) = p_{atm} - \left\{ \frac{1}{4\pi} + \frac{3\pi}{40} - \frac{15}{16} + \frac{2}{\pi} \ln \frac{R_\infty}{B} \right\} \frac{d^2 h}{dt^2} \\ - \rho \left\{ \frac{9}{2\pi^2} - \frac{6}{5} - \frac{1}{2\pi} \right\} \left(\frac{dh}{dt} \right)^2 - 4 \left[2 + \frac{1}{\pi} \right] \frac{\mu}{B} \frac{dh}{dt} \end{aligned} \quad (2.29)$$

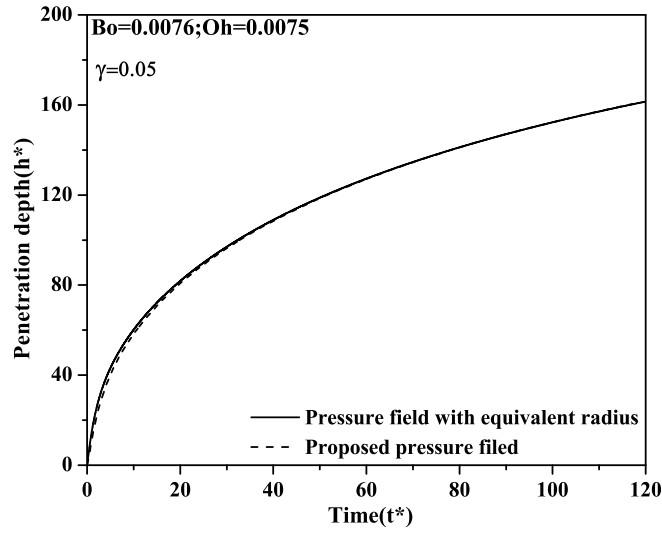
One can re-derive the governing equation Eq.2.11 with the proposed pressure field as presented in Eq. 2.28 instead of Eq. 2.10. It is necessary to

perform the analysis to understand the effect of pressure field on the capillary transport. Therefore, in the upcoming section the penetration depth with the pressure field from the literature is compared with the penetration depth calculated using the proposed pressure field.

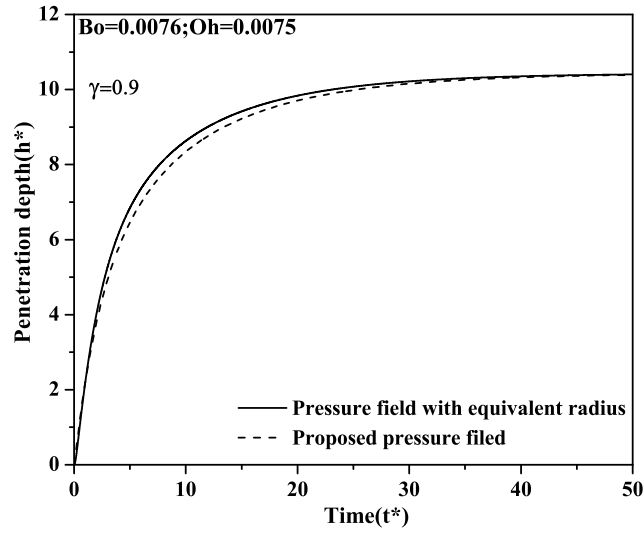
2.5 Effect of appropriate pressure field in the capillary transport

Figure 2.6 shows the variation in the penetration depth with the pressure field from the literature and with the newly proposed pressure field expression. As mentioned earlier, the pressure field expression for rectangular microchannel from literature has been extended from circular capillary expression with an equivalent radius assumption. Hence in Fig. 2.6, the penetration depth obtained using the pressure field from the literature is labeled as the pressure field with equivalent radius. For higher aspect ratio microchannels, the length of the cylindrical region (Fig. 2.5(c)) is much longer than the radius of the spherical region therefore, the fluid volume entering through the spherical region is negligible as compared to the fluid volume entering through the cylindrical region.

Figure 2.6(a) shows the variations in the penetration depths for $\gamma = 0.05$ which represents the microchannel of very small width as compared to its depth. For such arrangements, it is observed that there is a negligible difference between the penetration depths with two different pressure fields. In such cases, the flow from cylindrical region of control volume plays significant role compared to the flow from the spherical region of the control volume, therefore the difference in the penetration depth is negligible. In case of lower aspect ratio microchannels, where the width is comparable with the depth of microchannel, the fluid volume entering from the ends of semicylindrical volumes, i.e., from the spherical regions along with that from cylindrical region can not be neglected. The penetration depth under such condition is depicted in Fig. 2.6(b). The penetration depth with proposed pressure field is significantly different than the penetration depth with pressure field from



(a) Penetration depths with higher aspect ratio microchannel



(b) Penetration depths with lower aspect ratio microchannel

Figure 2.6: The comparison of variations in the penetration depth with equivalent radius and with recently proposed pressure field expressions. Figure 2.6(a) shows the comparison of penetration depth for $\gamma = 0.05$ where Fig. 2.6(b) shows the comparison for $\gamma = 0.9$.

the literature. During the filling of the microchannel, the magnitude of the penetration depth with the proposed pressure field is less than the penetration

depth with the pressure field from literature for the same time instant, which can be attributed to the additional fluid mass from the spherical regions. It is observed that, pressure field from the literature over predicts the penetration depth. Thus, the proposed pressure field expression is an appropriate pressure field expression for the analysis of capillary flow in rectangular microchannel, which is applicable for a wide range of aspect ratios of the microchannel.

2.6 Conclusion

In traditional capillary flow analysis, the velocity across the microchannel and the pressure field at the microchannel entrance are considered with the simplified assumptions. In this study, these assumptions are revisited and modifications in these assumptions are presented. Initially, the analysis emphasize on the nature of the velocity profile across the microchannel. For inherently transient capillary flow analysis, the steady state velocity profile is used in the literature. In this study, the transient developing velocity profile instead of fully developed velocity profile is used to investigate the effect of transience in the velocity profile. The non-dimensional governing equation for penetration depth i.e., flow front movement along the microchannel due to capillary with the transient velocity profile is derived. Further, the penetration depth with the proposed velocity profile is compared with the penetration depth for steady state velocity profile. While deriving the governing equation, different forces like, gravity, viscous and pressure forces acting on the fluid volume are considered. Generally, the pressure force acting at the entrance of the microchannel is deduced from the pressure field expression at the microchannel inlet. In the past studies, for rectangular microchannels, the circular capillary expression is adopted with an equivalent radius assumption. This assumption may not be valid for all cases. An appropriate pressure field for rectangular microchannels is proposed and compared with the pressure field from literature. From the theoretical analysis following important conclusions can be made:

- In capillary flow analysis, transience in the velocity profile need to be considered at the beginning of the transport. The difference in the pene-

tration depth is observed at the beginning of the filling process whereas, this difference is negligible as flow becomes developed or steady state flow.

- For a high density and viscous fluid, transient effect is observed at the beginning of the filling of the microchannel.
- Transience effect is more for high density fluid than high viscosity fluid.
- The flow front progression with the proposed pressure field is slower than the flow front progression with the approximated pressure field from the literature.
- For lower aspect ratio microchannels, where typically the rectangular microchannel geometries approaches towards the square microchannel, it is important to consider the proposed pressure field.

References

- Bhattacharya S. and Gurung D., Derivation of governing equation describing time-dependent penetration length in channel flows driven by non-mechanical forces. *Analytica Chimica Acta*, 666(1-2):51–54, 2010.
- Chakraborty S., Electroosmotically driven capillary transport of typical non-newtonian biofluid in rectangular microchannels. *Analytica Chimica Acta*, 605(2):175–184, 2007.
- Dimitrov D., Milchev A., and Binder K., Capillary rise in nanopores: Molecular dynamics evidence for the lucas-washburn equation. *Phys. Rev. Lett.*, 99(5):054501-1–4, 2007.
- Diotallevi F., Chibbaro L., Biferale S. , Toschi G., Pontrelli F., and Succi S., Lattice boltzmann simulations of capillary filling: Finite vapour density effects. *The European Physical Journal - Special Topics*, 171(1):237–243, 2009.
- Dreyer M., Delgado A., and Path H. J., Capillary rise of liquid between parallel plates under microgravity. *Journal of Colloid And Interface Science*, 163(1): 158–168, 1994.
- Dreyer M., Delgado A., and Rath H. J., Fluid motion in capillary vanes under reduced gravity. *Microgravity Science Technology*, 5(4):203–210, 1993.
- Eijkel J. C. T. and van den Berg A. Young 4ever - the use of capillarity for passive flow handling in lab on a chip devices. *Lab On a Chip*, 6(11): 1405–1408, 2006.

- Juncker D., Schmid H., Drechsler U., Wolf H., Wolf M., Michel B., de Rooij N., and Delamarche E., Autonomous microfluidic capillary system. *Analytical Chemistry*, 74(24):6139–6144, 2002.
- Karniadakis G., Beskok A., and Aluru N., *Microflows and Nanoflows Fundamentals and Simulation*. Springer Berlin, New York, 2005.
- Keh H. and Tseng H., Transient electrokinetic flow in fine capillaries. *Journal of Colloid and Interface Science*, 242(2):450, 2001.
- Levine S., Lowndes J., Watson E., and Neale G., A theory of capillary rise of a liquid in a vertical cylindrical tube and in a parallel-plate channel. *Journal of Colloid and Interface Science*, 73(1):136–151, 1980.
- Levine S., Reed P., and Watson J., A theory of the rate of rise a liquid in a capillary. *Colloid and Interface Science*, 3(1):403–419, 1976.
- Mawardi A., Xiao Y., and Pitchumani R., Theoretical analysis of capillary-driven nanoparticulate slurry flow during a micromold filling process. *International Journal of Multiphase Flow*, 34(3):227–240, 2008.
- Newman S., Kinetics of wetting of surfaces by polymers; capillary flow. *Journal of Colloid and Interface Science*, 26(2):209, 1968.
- Nguyen N. and Wereley S., *Fundamentals and Applications of Microfluidics*. Artech House, New York, 2003.
- Phan V. M., Nguyen N.-T., Yang C., Joseph P., Djeghlaf L., Bourrier D., and A. -M. Gue, Capillary filling in closed end nanochannels. *Langmuir*, 26(16):13251–13255, 2010.
- Phan V. M., Yang C., and Nguyen N.-T., Analysis of capillary filling in nanochannels with electroviscous effects. *Microfluidics and Nanofluidics*, 7(4):519–530, 2009.

- Radiom M., Chan W., and Yang C., Capillary filling with the effect of pneumatic pressure of trapped air. *Microfluidics and Nanofluidics*, 9(1):65–75, 2010.
- Saha A. A. and Mitra S. K., Effect of dynamic contact angle in a volume of fluid (VOF) model for a microfluidic capillary flow. *Journal of Colloid and Interface Science*, 339(2):461–480, 2009a.
- Saha A. A. and Mitra S. K., Numerical study of capillary flow in microchannels with alternate hydrophilic-hydrophobic bottom wall. *Journal of Fluids Engineering, Transactions of the ASME*, 131(6):0612021–06120212, 2009b.
- Saha A. A., Mitra S. K., Tweedie M., Roy S., and McLaughlin J., Experimental and numerical investigation of capillary flow in SU8 and PDMS microchannels with integrated pillars. *Microfluidics and Nanofluidics*, 7(4):451–465, 2009.
- Schlichting D., *Boundary layer theory (translated by Dr. Kestin)*. Mc-Graw Hill Book Company, London, 1968.
- Szekely J., Neumann A. W., and Chuang Y. K., The rate of capillary penetration and the applicability of the Washburn equation. *Journal of Colloid And Interface Science*, 35(2):273–278, 1971.
- Waghmare P. R. and Mitra S. K., Finite reservoir effect on capillary flow of microbead suspension in rectangular microchannels. *Journal of Colloid and Interface Science*, 351(2):561–569, 2010a.
- Waghmare P. R. and Mitra S. K., Modeling of combined electroosmotic and capillary flow in microchannels. *Analytica Chimica Acta*, 663(2):117–126, 2010b.
- Waghmare P. R. and Mitra S. K., On the derivation of pressure field distribution at the entrance of a rectangular capillary. *Journal of Fluid Engineering*, 132(5):Art. No. 054502, 2010.

- Walker G. M. and Beebe D. J., A passive pumping method for microfluidic devices. *Lab on a Chip - Miniaturisation for Chemistry and Biology*, 2(3):131–134, 2002.
- Washburn E., The dynamics of capillary flow. *Physical Review*, 17(3):273-283, 1921.
- White F. M., *Viscous fluid flow*. McGrawhill, 2006.
- Xiao Y., Yang F., and Pitchumani R., A generalized flow analysis of capillary flows in channels. *Journal of Colloid and Interface Science*, 298(2):880–888, 2006.
- Zhang J., Lattice boltzmann method for microfluidics: models and applications. *Microfluidics and Nanofluidics*, 10(1):1–28, 2011.
- Zimmermann M., Schmid H., Hunziker P., and Delamarche E., Capillary pumps for autonomous capillary systems. *Lab on a Chip - Miniaturisation for Chemistry and Biology*, 7(1):119–125, 2007.

Chapter 3

On the derivation of pressure field distribution at the entrance of a rectangular capillary¹

3.1 Introduction

Passive pumping in microfluidic devices has become an area of interest in the last decade (Levine et al., 1976; Zimmermann et al., 2007). Larger surface to volume ratio results in dominant surface forces over body forces. The surface forces can be used to transport fluid with the capillary action i.e., capillarity. The capillary action is an important surface force in microscale which is used in several passive microfluidic devices for transporting the fluid (Karniadakis et al., 2005; Zimmermann et al., 2007). Theoretical analyses of such capillary flows are reported in the literature to predict the capillary flow front transport in the circular and rectangular capillaries (Dreyer et al., 1994, 1993; Washburn, 1921; Xiao et al., 2006). In these analyses, the penetration of the flow front along the microchannel is analyzed with different non-mechanical forces which are acting on the fluid. The magnitude of the flow front penetration along the microchannel depends on several parameters such as pressure at the interface i.e., at the flow front, pressure at the inlet of the microchannel, physical properties of the fluid, etc.

In such analysis, an integral momentum equation in the direction of the

¹A version of this chapter has been published. Waghmare and Mitra, 2010, Journal of Fluid Engineering, 132 (5), 0545021-0545024

capillary front transport is considered. The transient, convective and summation of the forces terms (viscous, gravity, pressure forces at the capillary interface and at the inlet of the capillary) are three main components of the momentum equation. In such integral momentum equations a deformable control volume is considered which extends from the entrance of the capillary to the interface of the capillary front. The forces and the velocity dependent terms in the integral momentum equation are derived to obtain the final form of the governing equation for the variation of the capillary penetration depth with time. The velocity dependent terms are deduced with an assumption of fully developed laminar velocity profile along the channel. Furthermore, pressure force at the flow front, viscous force and other relevant forces in microscale such as electroosmotism (Chakraborty, 2007; Waghmare and Mitra, 2010c) are calculated. Generally, the pressure force at the capillary entrance is determined by the pressure field exerted by the fluid at the entrance of the capillary. Levine et al. (Levine et al., 1976) for the first time reported that the pressure field at the entrance of the capillary can not be considered to be at atmospheric pressure. Hence, the appropriate pressure field at the entrance of the circular capillary is derived meticulously considering a separate control volume at the entrance of the capillary. In their analysis, it is assumed that the fluid enters in the capillary from an infinitely large fluid reservoir placed at the entrance of the capillary, which constitutes an additional control volume for the analysis separate from the deformable control volume mentioned earlier. Such representative control volume, as considered by Levine et al. (Levine et al., 1976), is taken as a hemisphere of radius equal to that of the capillary, whose fluid volume now acts as an infinite reservoir. Further, the pressure field at the entrance is obtained by the momentum balance to the fluid flow in the hemispherical control volume.

Using the classical derivation proposed by Levine et al. (Levine et al., 1976) for circular capillaries, other researchers have adopted the same formulation for capillaries of inherently different geometries like, parallel plates (Dreyer et al., 1993). For parallel plate configuration, the pressure field is investigated

by assuming a hemispherical control volume in the reservoir and the radius of the hemisphere is determined from the projected cross sectional area at the capillary entrance. Such pressure field expression, as derived by Dreyer et al. (Dreyer et al., 1993), has been used by several other researchers for rectangular capillaries such as flow of liquid coolant (Dreyer et al., 1994), alcohol (Xiao et al., 2006), nanoparticulate slurry (Mawardi et al., 2008), and blood (Chakraborty, 2007). The assumption of hemispherical control volume does not represent a realistic situation of capillary flow for non-circular geometries. In particular, for high aspect ratio channels (plate gap \ll width), this simplification is questionable as the infinite reservoir can no longer be considered as a hemisphere. For such geometries, the reservoir will be a semi-circular cylinder. Hence, for a high aspect ratio capillary, the assumption of hemispherical region may not be valid. Therefore, there is a need to evaluate the correct pressure field based on an appropriate control volume representing the infinite reservoir for capillary flows with non-circular geometries.

3.2 Pressure field distribution at the entrance of the parallel plate arrangement

In this section the derivation of the pressure field at the entrance of a parallel plate capillary is presented. Figure 3.1 shows two parallel plates forming the capillary with spacing of $2B$ in between them and width of $2W$, which are placed perpendicular to the free liquid surface from the reservoir. As mentioned earlier, for such arrangement, the semicylindrical volume at the inlet is an appropriate control volume for determining the entrance pressure field. Therefore, a semicylindrical region at the entrance with center ‘ O ’ aligned with the capillary is considered. Introducing a cylindrical co-ordinate system r , θ , and y in the reservoir with origin ‘ O ’, it is assumed that, the velocity component v_r is in the direction of r only for the region $r > B$ from reservoir. The velocity component v_r becomes zero on the plane $z = 0$ due to the no-slip boundary conditions at the entry plane of the channel. The fluid front is moving in the gap between two parallel plates with penetration rate $\frac{dh}{dt}$ where, h

is the position of the flow front measured from the origin ‘ O ’ in the direction of the capillary flow between the plates, i.e., along z - direction, as shown in Fig. 3.1.

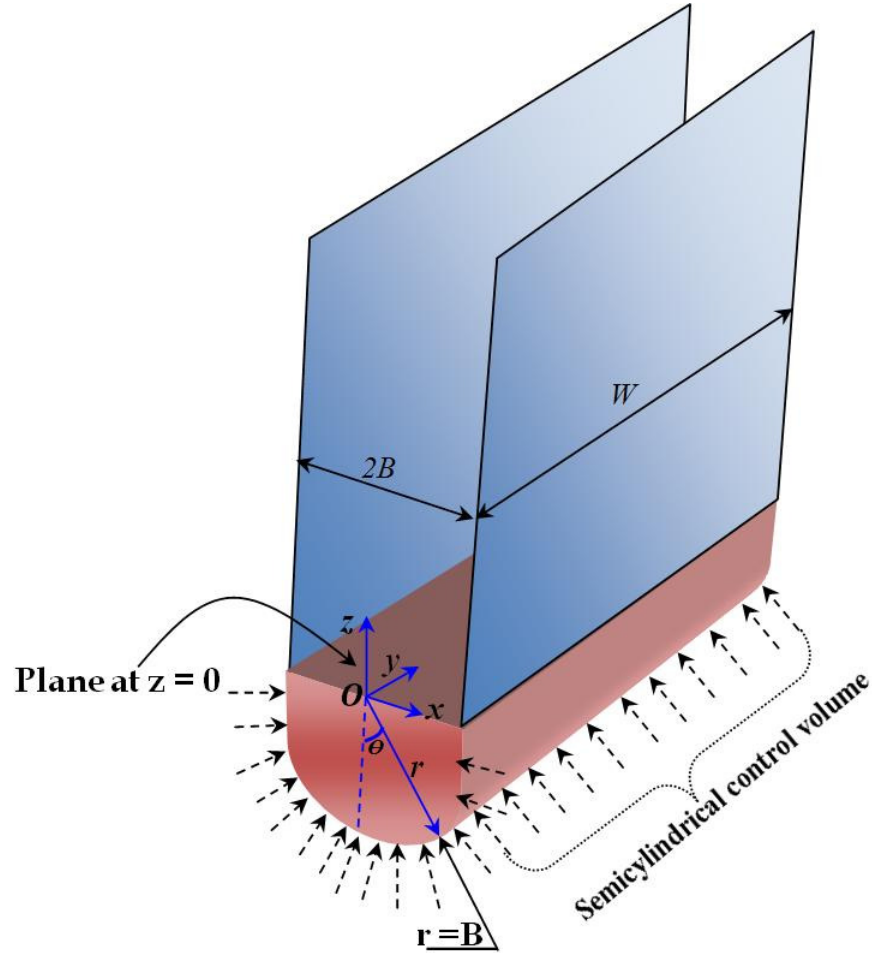


Figure 3.1: Schematic of the capillary flow between parallel plates with the semicylindrical control volume. Arrows indicating the direction of fluid flow into the capillary

The volume flux at $r = B$ in the inward direction can be given by continuity equation as,

$$-\int_{-W}^W \int_0^\pi v_r r d\theta dy = 4BW \frac{dh}{dt} \quad (3.1)$$

which results in an expression for v_r ,

$$v_r = \frac{-2B}{\pi r} \frac{dh}{dt} \quad (3.2)$$

The momentum equation in the radial direction is,

$$\begin{aligned} & \rho \left\{ \frac{\partial v_r}{\partial t} + v_r \frac{\partial v_r}{\partial r} + \frac{v_\theta}{r} \frac{\partial v_r}{\partial \theta} - \frac{v_\theta^2}{r} + v_z \frac{\partial v_r}{\partial z} \right\} \\ = & \rho g_r - \frac{\partial p}{\partial r} + \mu \left\{ \frac{\partial}{\partial r} \left(\frac{1}{r} \frac{\partial}{\partial r} [rv_r] \right) + \frac{1}{r^2} \frac{\partial^2 v_r}{\partial \theta^2} - \frac{2}{r^2} \frac{\partial v_\theta}{\partial \theta} + \frac{\partial^2 v_r}{\partial z^2} \right\} \end{aligned} \quad (3.3)$$

Typically, the capillary flows have very low Reynolds number hence, such flow can be considered to be a creeping flow. Under creeping flow assumption, the inertial terms from Eq. 3.3 drops out. Since, the velocity component in θ direction is zero and the variation in the velocity along θ and z can also be neglected, then Eq. 3.3 reduces to

$$\rho \left[\frac{\partial v_r}{\partial t} \right] = - \frac{\partial p}{\partial r} + \mu \left[\frac{\partial}{\partial r} \left(\frac{1}{r} \frac{\partial}{\partial r} [rv_r] \right) \right] \quad (3.4)$$

Now by combining Eqs. 3.2 and 3.4, the transient pressure field $p(r, t)$ can be written as,

$$p(r, t) = p_{atm} - \frac{2B\rho}{\pi} \frac{d^2 h}{dt^2} \left(\ln \frac{r_\infty}{r} \right) \quad (3.5)$$

Here r_∞ is the radial distance far away from the inlet outside the semicylindrical region, where the capillary forces vanishes and $p(r, t)$ approaches the atmospheric pressure p_{atm} .

The pressure field at the entrance of the capillary is to be determined, for which the knowledge of velocity field within the semicylindrical region ($r \leq B$) is required. For semicylindrical region, the momentum balance can be expressed as the rate of change of total momentum equal to the combination of the net momentum flux and the summation of the forces acting on the control volume. The calculation of the different forces, the momentum flux and the rate of change of momentum required for the momentum balance within a semicylindrical region is presented here.

There are two forces acting on the volume under consideration; one is the force over the surface of the semicylindrical volume and another one is at the

entrance of the capillary. The force exerted on the surface at $r = B$ can be calculated using the stress tensor, as shown here:

$$\sigma_{ij} = -p\delta_{ij} + \sigma_v$$

where, δ_{ij} is the Kronecker delta and σ_v is the viscous stress tensor. The stress tensor σ_{ij} at the semicylinder surface $r = B$ in the direction of r can be written as,

$$\sigma_{rr} = -p(r, t)|_{r=B} + 2\mu \left. \frac{\partial v_r}{\partial r} \right|_{r=B} \quad (3.6)$$

Substituting the pressure field at $r = B$ from Eq. 3.5 and using Eq. 3.2, the stress tensor at the semicylindrical surface can be re-written as,

$$\sigma_{rr} = -p_{atm} + \frac{2B\rho}{\pi} \frac{d^2h}{dt^2} \left[\ln \frac{r_\infty}{B} \right] + \frac{4\mu}{\pi B} \frac{dh}{dt} \quad (3.7)$$

Hence, the force over the semicylindrical surface in the direction of the r with component along θ can be calculated as,

$$F_{r=B} = 2 \int_{-W}^W \int_0^{\frac{\pi}{2}} -\sigma_{rr} \cos \theta r d\theta dy \quad (3.8)$$

The other force exerted by the fluid in the gap between two parallel plates across the base i.e., at the entrance ($z = 0$) in the direction of the fluid front transport is

$$F_{z=0} = - \int_{-W}^W \int_{-B}^B p(0, t) dx dy \quad (3.9)$$

The second part of the momentum balance equation is the net momentum fluxes which can be calculated by determining the momentum fluxes entraining along the semicylindrical surface and leaving the base of the capillary.

The momentum flux entering the semicylindrical region in the direction of capillary transport across the surface can be calculated as,

$$\dot{M}_{r=B} = 2 \int_{-W}^W \int_0^{\frac{\pi}{2}} v_r \cos \theta (\rho v_r) r d\theta dy \quad (3.10)$$

The knowledge of velocity profile across the channel is required to determine the momentum flux at the entrance of the capillary ($z = 0$). For transient solution, time dependent velocity profile is required. Hence, the fluid flow velocity profile as a function of rate of the capillary penetration depth ($\frac{dh}{dt}$) is considered in past analyses (Dreyer et al., 1994, 1993; Levine et al., 1976; Mawardi et al., 2008; Xiao et al., 2006) and it is assumed that, the flow is fully developed laminar flow. In the recent study by Bhattacharya and Gurung (Bhattacharya and Gurung, 2010), they have showed that this assumption introduces an error of the same order as that of neglecting the inertial terms in Eq. 3.3, which may not necessarily hold true for large Reynolds number flow. However, in the present case for microfluidic applications, it is essentially a creeping flow and hence the assumption of the velocity profile provided in Eq. 3.11 holds true as the inertial terms are always neglected in such analysis. The fully developed laminar flow velocity profile as a function of rate of penetration depth ($\frac{dh}{dt}$) can be written as,

$$v_z = \frac{3}{2} \frac{dh}{dt} \left[1 - \left(\frac{x}{B} \right)^2 \right] \quad (3.11)$$

Using Eq. 3.11, the momentum flux leaving at the entrance of the capillary ($z = 0$) can be calculated as,

$$\dot{M}_{z=0} = \int_{-W}^W \int_{-B}^B v_z (\rho v_z) dx dy \quad (3.12)$$

The remaining part of the momentum balance equation is the rate of change of total momentum within the control volume which is related to its mass and its instantaneous acceleration. Hence, the instantaneous acceleration within the control volume is required to determine the rate of change of total momentum, which is somewhat difficult to calculate. Instead of instantaneous acceleration, the mean acceleration is calculated at the two surfaces i.e., at

$r = B$ and $z = 0$ (Levine et al., 1976). The mean acceleration at $r = B$ and $z = 0$ can be determined by calculating the flux of acceleration at respective locations and the volume flux along the capillary.

The flux of acceleration in the direction of the capillary transport i.e., in the z -direction across $r = B$ is given by,

$$2 \int_{-W}^W \int_0^{\frac{\pi}{2}} v_r \cos \theta \left(\frac{Dv_r}{Dt} \right)_{r=B} r d\theta dy \quad (3.13)$$

and the volume flux in the capillary channel is $4BW \frac{dh}{dt}$. Therefore, the mean acceleration at $r = B$ becomes,

$$\frac{8}{\pi^3 B} \left(\frac{dh}{dt} \right)^2 + \frac{4}{\pi^2} \frac{d^2 h}{dt^2} \quad (3.14)$$

At $z = 0$, the flux of acceleration in the direction of the flow front transport can be given as,

$$\int_{-W}^W \int_{-B}^B \frac{dv_z}{dt} v_z dx dy \quad (3.15)$$

The expression provided in Eq. 3.15 can be evaluated by replacing the velocity profile provided in Eq. 3.11, which reduces to

$$\frac{24BW}{5} \frac{dh}{dt} \frac{d^2 h}{dt^2} \quad (3.16)$$

and hence the mean acceleration at $z = 0$ is $\frac{6}{5} \frac{d^2 h}{dt^2}$.

As stated earlier, the mean acceleration in the semicylindrical control volume is considered over the $z = 0$ and $r = B$. Therefore, the rate of change of total momentum can now be written as,

$$\frac{4\rho BW}{\pi^2} \left(\frac{dh}{dt} \right)^2 + \rho\pi B^2 W \left(\frac{3}{5} + \frac{2}{\pi^2} \right) \frac{d^2 h}{dt^2} \quad (3.17)$$

Using Eqs. 3.8, 3.9 3.10, 3.12 and 3.17 one can write the momentum balance and can obtain the pressure field at the entrance of the capillary as,

$$p(0, t) = p_{atm} - \left\{ \rho B \left[\left(\frac{3\pi}{20} + \frac{1}{2\pi} \right) + \frac{2}{\pi} \left(\ln \frac{r_\infty}{B} \right) \right] \frac{d^2 h}{dt^2} + \rho \left[\frac{3}{\pi^2} - \frac{6}{5} \right] \left(\frac{dh}{dt} \right)^2 + \frac{4\mu}{\pi B} \frac{dh}{dt} \right\} \quad (3.18)$$

3.3 Comparison between the pressure field based on the equivalent radius and the exact solution

Equation 3.18 derived in the previous section can be re-written in a generalized form with different coefficients as

$$p(0, t) = p_{atm} - \left\{ \alpha_1 \rho \frac{d^2 h}{dt^2} + \rho \alpha_2 \left(\frac{dh}{dt} \right)^2 + \alpha_3 \mu \frac{dh}{dt} \right\} \quad (3.19)$$

Levine et al. (Levine et al., 1976) reported that, the pressure field expression for a circular capillary of radius ‘a’ is given by,

$$p(0, t) = p_{atm} - \left\{ \frac{37}{36} \rho a \frac{d^2 h}{dt^2} + \rho \frac{7}{6} \left(\frac{dh}{dt} \right)^2 + \frac{2\mu}{a} \frac{dh}{dt} \right\} \quad (3.20)$$

As mentioned earlier, several researchers have replaced the circular capillary radius by an equivalent radius based on a projected area for rectangular capillaries and obtained an expression for the pressure field with modified coefficients, as reported in Table 3.1. In the present analysis, the appropriate assumption for the control volume at the entrance of the parallel plates is made to deduce the exact form of the entrance pressure field and the corresponding coefficients are presented in Table 3.1. It can be observed that, the

Table 3.1: Comparison between the coefficients of the expression used in the literature and proposed expression in the presented analysis

Constants	Literature for rectangular capillary with equivalent radius (Dreyer et al., 1994, 1993) (Xiao et al., 2006) Mawardi et al. (2008) (Chakraborty, 2007)	Proposed analysis
α_1	$1.11\sqrt{BW}$	$0.6304B + 0.636 \ln \left(\frac{r_\infty}{B} \right)$
α_2	1.158	0.245
α_3	$\frac{1.772}{\sqrt{BW}}$	$\frac{1.273}{B}$

coefficients of the pressure field expression are different from each other. It is

to be noted that, the final form of governing equation of a capillary transport is also a partial differential equation of same order as the pressure field expression (Dreyer et al., 1994, 1993; Levine et al., 1976; Mawardi et al., 2008; Xiao et al., 2006). Hence, any change in the expression for the pressure field will produce changes in the final form of the governing equation for the capillary transport in non-circular capillaries. Therefore, for a better theoretical prediction of a capillary transport in the rectangular channels, the proposed expression for the entrance pressure field needs to be considered.

3.4 Conclusion

In the present analysis, the pressure field at the entrance of the parallel plate arrangement for a capillary transport is investigated. In most of the earlier studies, the governing equation for a capillary transport in circular and rectangular capillaries is derived considering the different forces acting on the transporting fluid along the capillary. The pressure field at the entrance of the capillary is the important parameter to deduce the pressure force at the entrance of the capillary. Researchers have used the circular capillary formulation by Levine et al. (Levine et al., 1976) for the rectangular capillary with an equivalent radius assumption. In the circular capillary analysis, the expression for the pressure field is determined by a momentum balance for the hemispherical region of the fluid at the entrance of the capillary. For a rectangular capillary flow analysis presented in the literature, the hemisphere of an equivalent radius corresponding to the rectangle formed by the parallel plates at the entrance is considered. For high aspect ratio capillaries, the semicylindrical control volume is a more appropriate assumption than a hemisphere of an equivalent radius. Hence, the expression for the entrance pressure field with the semicylindrical region at the entrance is deduced in this work. The comparison between the proposed pressure field and those reported in the existing literature suggests that, there exists a significant difference in their respective coefficients. This change in the coefficients of the pressure field expression will change the theoretical predictions of the capillary transport and hence for a

rectangular capillary with high aspect ratio, the proposed expression for the pressure field needs to be considered.

References

- Bhattacharya S. and Gurung D. Derivation of governing equation describing time-dependent penetration length in channel flows driven by non-mechanical forces. *Analytica Chimica Acta*, 666(1-2):51–54, 2010.
- Chakraborty S. Electroosmotically driven capillary transport of typical non-newtonian biofluid in rectangular microchannels. *Analytica Chimica Acta*, 605(2):175–184, 2007.
- Dreyer M., Delgado A., and Path H.-J. Capillary rise of liquid between parallel plates under microgravity. *Journal of Colloid And Interface Science*, 163(1):158–168, 1994.
- Dreyer M., Delgado A., and Rath H.-J. Fluid motion in capillary vanes under reduced gravity. *Microgravity Science Technology*, 5(4):203–210, 1993.
- Karniadakis G., Beskok A., and Aluru N. *Microflows and Nanoflows Fundamentals and Simulation*. Springer Berlin, New York, 2005.
- Levine S., Reed P., and Watson J. A theory of the rate of rise a liquid in a capillary. *Colloid and Interface Science*, 3(1):403–419, 1976.
- Mawardi A., Xiao Y., and Pitchumani R. Theoretical analysis of capillary-driven nanoparticulate slurry flow during a micromold filling process. *International Journal of Multiphase Flow*, 34(3):227–240, 2008.
- Waghmare P. R. and Mitra S. K. Modeling of combined electroosmotic and capillary flow in microchannels. *Analytica Chimica Acta*, 663(2):117–126, 2010.

Washburn E. The dynamics of capillary flow. *Physical Review*, 17(3):273-283, 1921.

Xiao Y., Yang F., and Pitchumani R. A generalized flow analysis of capillary flows in channels. *Journal of Colloid and Interface Science*, 298(2):880–888, 2006.

Zimmermann M., Schmid H., Hunziker P., and Delamarche E. Capillary pumps for autonomous capillary systems. *Lab on a Chip - Miniaturisation for Chemistry and Biology*, 7(1):119–125, 2007.

Chapter 4

Contact angle hysteresis of microbead suspensions¹

4.1 Introduction

Microparticles are widely used as carriers for biomolecules in most of the biomedical devices. Rapid advancement in the microfabrication opened new areas for biomedical devices which are commonly known as micro total analysis system ($\mu - TAS$) or lab-on-a-chip (LOC) devices (Kawaguchi, 2000). In such microscale devices, the higher surface to volume ratio makes surface forces dominant over body forces which results in a large pumping power for pressure driven flows (Nguyen and Wereley, 2003). Hence, attempts are being made to use non-mechanical pumping mechanisms such as passive pumping to transport biomolecules or analytes of interest (Karniadakis et al., 2005). Flow driven by surface tension i.e., capillary flow is one of the popular approaches in passive microfluidics (Waghmare and Mitra, 2010c; Walker and Beebe, 2002). In the capillary flow, wetting properties of the transporting fluid decide the capability of the passive pumping. Therefore, in microfluidic applications lower contact angles are preferred for favorable passive pumping conditions. Generally, in $\mu - TAS$, biomolecules or microbead suspension containing attached biomolecules are transported within the chip. Existing literature suggests that even though there is some understanding of the wetting properties for nanopar-

¹A version of this chapter has been published. Waghmare and Mitra, 2010, Langmuir, 26 (22), 17082-17089

ticle suspensions (Sefiane et al., 2008), there is hardly any in-depth study of the wetting characteristics of microbead suspension. The interaction of suspended particles with the carrier fluid is well understood (Hörvölgyi et al., 1993), but the combined interaction of particle and fluid with the solid surface is yet to be understood fully. Therefore, a detailed experimental study of the wetting properties of the microbead suspensions is required.

Surface tension and contact angle dictate the intermolecular interaction at the interface of different phases. The surface tension represents the magnitude of interaction, whereas the limit to the interaction can be defined by the contact angle (Hiemenz and Rajagopalan, 1997). Static or equilibrium contact angle i.e., θ_e is the angle without any fluid motion on the solid surface, as shown in Fig. 4.1. The determination of an equilibrium contact angle of a sessile drop for different combinations of solid-liquid-air interface is of interest to number of researchers. The interface shape and the magnitude of the equilibrium contact angle are still under development (Sefiane et al., 2008). There are several parameters which affect the equilibrium contact angle like the presence of the three phases, intermolecular interaction among three phases, surface roughness, nature of liquid deposition, etc (Lam et al., 2001). Based on the Young's equation, the equilibrium contact angle can be predicted. For the solid-liquid-vapour system, as shown in Fig. 4.1, there are three interfacial tensions viz., liquid-vapour, solid-vapour and solid-liquid i.e., γ_{LV} , γ_{SV} and γ_{SL} , respectively. Young (Young, 1805) proposed that, at thermodynamic equilibrium, summation of the horizontal components of the surface tension is zero which can be written as,

$$\gamma_{LV} \cos \theta_e = \gamma_{SV} - \gamma_{SL}. \quad (4.1)$$

From Eq. 4.1, one can obtain the equilibrium contact angle. There are several limitations for the pertinency of the Young's equation, for example the surface tension values may not be known for different surface pairs. Furthermore, this equation is applicable under chemically inert environment with smooth substrate, which is not always practical. The Young's equation has also ignored the volume of the drop and the deposition method of the liquid.

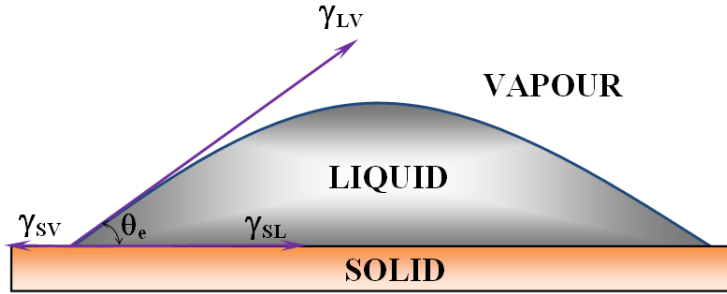


Figure 4.1: Schematic of a symmetric sessile drop on a solid surface with an equilibrium contact angle.

Due to these shortcomings, the equilibrium contact angle obtained by Young's equation cannot be used readily for practical applications, particularly in the present study with microbead suspensions.

The surface tension values required for computing the contact angle can be measured experimentally using pendant drop method (Edgerton et al., 1937). As mentioned earlier, there are several parameters, which can affect the equilibrium contact angle in practice. Therefore, in experimental studies, always there is a variation in the equilibrium contact angle measurement, as reported in the literature (Kwok, 1998). Hence, the dynamic response of the contact angle i.e., hysteresis in the contact angle needs to be considered to calculate the equilibrium contact angle. The characterization of the wetting properties of the microbead suspension with the variation in the concentration of the microbead is an important part of this study. The detailed explanation of the relevant theory for the wetting of the surface is presented in the following section.

In dynamic contact angle measurement, two different types of contact angles are measured. The angle measured during the advancement of a contact line or wetting of the surface is referred as an advancing contact angle (θ_a). The angle measured during the de-wetting of the surface or receding of the contact line is referred as receding contact angle (θ_r) (Extrand, 2002). The difference between θ_a and θ_r is termed as a hysteresis of contact angle which is typically in the range of $5^\circ - 20^\circ$. This hysteresis effect can be substan-

tial for certain cases (Adamson and Gast, 1997; Butt et al., 2003). Effect of roughness, inhomogeneity in the substrate, line tension, etc. may affect the contact angle individually or in combination (Chau et al., 2009). Drelich et al. (Drelich et al., 1996) reported a detailed study on the contact angle hysteresis in conjunction with the surface heterogeneity and also commented on the effect of droplet volume on the contact angle. However, their study is mainly for water and ethylene glycol on rough polythene surfaces.

Existing literature suggests that the contact angle hysteresis is studied initially for surfactants. Sarkar and Gaudin (Sarkar and Gaudin, 1966) studied the contact angle hysteresis with the variation in the surfactant concentration. Further, the contact angle hysteresis has been reported for other areas like in geology (Woche et al., 2005), petroleum (Cho et al., 2008; Hsieh et al., 2009), porous media (Hilpert and Ben-David, 2009), etc. In most of these studies, the contact angle hysteresis is computed either with different solute-solvent concentration (Lam et al., 2002) or with different chemicals (Lam et al., 2002; Wang et al., 2005) or for different substrate materials (Hilpert and Ben-David, 2009). A more detailed coverage of studies related to the contact angle hysteresis can be found elsewhere (Extrand, 2006). However, to the best of authors knowledge, contact angle hysteresis measurement for microbead suspension has not been studied extensively. As mentioned earlier, for μ -TAS and LOC applications, the efficient transport of microbeads within microfluidic devices is required. Therefore, for such cases, it is important to investigate the wetting properties of the microbead suspension on a substrate. Several attempts are being made to investigate the effect of substrate heterogeneity on the dynamic wettability (Rupp et al., 2002) or contact angles of microparticles at the interface (Grigoriev et al., 2007). Studies have been conducted to characterize the variation in contact angle by arranging the nanoparticles of different sizes on a Si substrate (Munshi et al., 2008). In case of nanofluids (nanoparticles in suspension), effects of nanoparticle concentration and its size on the dynamic contact angle are also studied (Sefiane et al., 2008; Vafaei et al., 2006). It is observed that, the concentration of

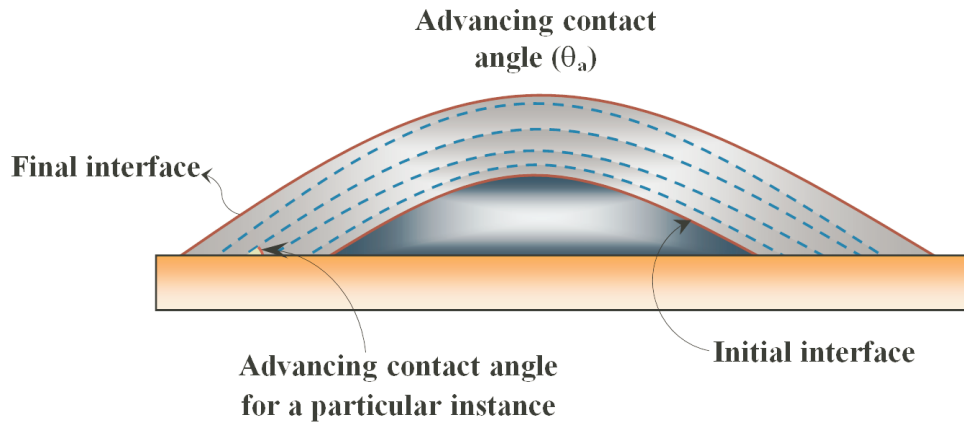
nanoparticles plays a vital role in predicting the wettability of the suspension with nanoparticles. The change in the nanoparticle diameter also affects the variation in the contact angle (Vafaei et al., 2006), which in turn has an impact on the wetting properties. Contact angle and surface tension represent the magnitude and the limit of three phase interaction at the interface. Presence of any foreign material in the fluid changes the intermolecular interaction, which in turn alters the interaction among all three phases. The wetting properties of the microbead suspension on the substrate depend mainly on the particle-particle, particle-fluid and particle-substrate interactions. These interactions are function of the surface properties of nanoparticles, microparticles or biomolecules in some cases. The particle-fluid-substrate interactions will be different for microparticles and nanoparticles. Hence, the wetting behavior of the nanoparticle suspension from the literature cannot be extended for the microparticle suspensions. However, an understanding of microbead suspension wettable properties is important for passive microfluidic devices particularly where the transport of biomolecules is concerned. There is lack of consistent studies about the wettability of the microbead suspension with the variation in the suspension concentration. Hence, in the present study the wettability of the microbead suspension is studied experimentally where the surface tension and the contact angle are measured for different microbead concentration.

The surface tension of the suspension is measured with the pendant drop technique and the equilibrium contact angle is determined with the dynamic contact angle measurements. Detailed explanation on measurement procedure adopted for this present study is given in the experimental measurement section. Different techniques for measurement of dynamic contact angle have been developed in the recent past, details of which can be found elsewhere (Chau, 2009). Three different techniques for dynamic contact angle measurement are popular in practice viz; Wilhelmy plate, inclined plate and sessile drop technique. In Wilhelmy technique, the contact angle of a liquid with particular solid is determined by measuring the height of capillary rise along a vertical

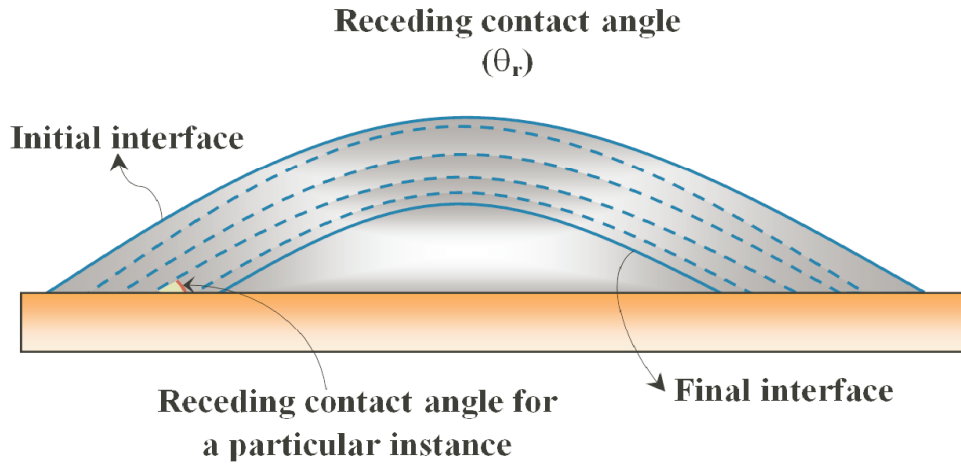
plate (Hayes et al., 1994). This measurement takes place under the relative motion between the solid and the liquid interface. In case of a sessile drop method, an image of the stable drop on the solid surface is captured and the contact angle is measured by positioning the tangent along the interface through the point of the three phase junction (Gu, 2006). In this case, the contact angle is measured with the advancement and the recession of the contact line. This movement of the contact line is achieved by changing the volume of the drop, as shown in Fig. 4.2. The inclined plate technique is another method which is widely used for the measurement of contact angle hysteresis. In case of inclined plate method, θ_a and θ_r are measured for a stationary drop placed on a plate kept at a maximum inclination angle. Beyond this maximum inclination, drop starts moving on the plate. Leading and trailing edge angles of the stationary drop at the maximum inclination of the plate represent advancing and receding contact angles, respectively (Macdougall and Ockrent, 1942). Requirement of a large sample volume for the measurement restricts the scope of the tilting plate and Wilhelmy techniques. Hence, for limited and costly samples, the sessile drop technique is a better option. Therefore, in the present study, the advancing and receding contact angles are measured with sessile drop technique. As depicted in Figure 4.2(a), θ_a is measured with the increase in the drop volume with constant flow rate whereas, θ_r is recorded with the reduction in the volume as shown in Figure 4.2(b). In the next section, the experimental procedure for measurement of contact angles and surface tension with different microbead concentrations is described. Further, the dynamic wetting with microbead suspension is explained and finally, the results and findings of the experiments are elaborated.

4.2 Experimental details

Dynamic contact angles with the sessile drop technique and the surface tension with pendant drop technique are measured using Krüss DSA 100 (Krüss GmbH, Hamburg, Germany). Figure 4.3 shows the schematic of the experimental set-up used for these measurements. A detailed explanation on the



(a) Advancing contact angle



(b) Receding contact angle

Figure 4.2: Pictorial representation of advancing and receding contact angles with initial and final positions of the interface during measurements.

sample preparation and measurement techniques are discussed in the following sections.

4.2.1 Sample preparation

Microbead suspensions with different concentrations are prepared for the analysis. Two different concentrations of microbead suspension are used for the experiments. In both the suspensions, polystyrene microbeads of $10\mu m$ in

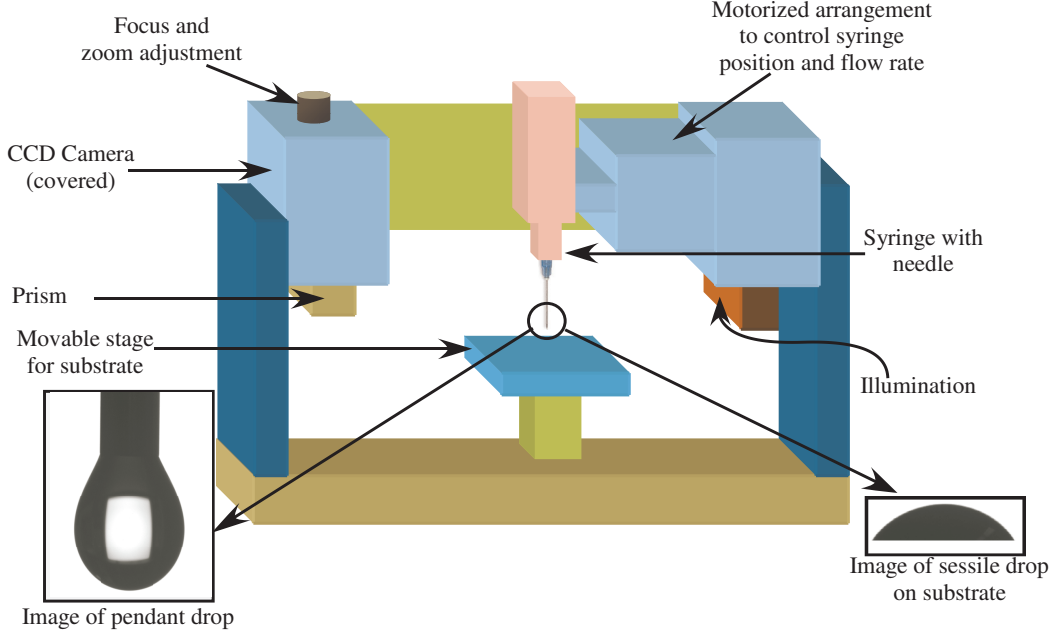


Figure 4.3: Schematic of the experimental set-up used for dynamic contact angle and surface tension measurements. Images of pendant drop and sessile drops in the inset are captured from the CCD camera.

diameter with maximum concentration i.e., of 10% and 5% are selected to prepare the samples. The polystyrene particles are selected based on its application related to the biomolecule transport in microfluidic devices (Verpoorte, 2003). The standard deviation in the particle size for 10% concentration i.e., Suspension A (Bangs Laboratories Inc., USA) and for 5% particles i.e., Suspension B (Discovery Scientific Inc., Canada) is 7.6% and 10.0%, respectively. The measurement of dynamic contact angle and surface tension is performed with Suspension A and Suspension B. Further, the suspension is diluted with deionized water (DI) to get a variation in the suspension concentration. Generally, the microbead suspension concentration ‘C’ containing microparticles of diameter d_p in the suspension is a known quantity. If the density of the microbead and the fluid i.e., ρ_p and ρ_f , respectively are known, the number of particles per ml can be calculated as (Tec, 2008),

$$n_p = \frac{6\rho_f}{\pi d_p^3 \left[\rho_f + \left(\frac{\rho_p}{C} \right) - \rho_p \right]} \quad (4.2)$$

The physical properties of suspensions are mostly expressed in terms of volume fraction, ϕ (Hiemenz and Rajagopalan, 1997), which is defined as the ratio of particle's volume in the suspension to the total suspension volume. For a calculated value of n_p given in Eq. 4.2, one can determine the total volume of the microparticles and subsequently the volume fraction of the sample can be computed. Samples of different volume fractions are prepared from the suspension with maximum concentration. An appropriate volume of DI water is added to obtain a required set of suspensions which has a variation in the volume fraction.

4.2.2 Surface tension measurement

The pendant drop method is used to determine the interfacial tension of the microbead suspension. An image of drop in hydromechanical equilibrium condition is captured. DSA drop shape analysis, an in-built software in the Krüss DSA 100 system is used for the image processing to determine the surface tension of the microbead suspension. The software relies on the derivation of surface tension based on Laplace pressure equation, details of which can be found elsewhere (Girault et al., 1984; Ham, 2004). Since, hydromechanical equilibrium condition of the pendant drop is an important parameter than the drop volume, the change in the drop volume is ignored during the surface tension measurement. For surface tension measurement, the optimum image of the pendant drop is obtained by slowly increasing the drop volume. Further, an image of the entire pendant drop with the needle is selected for the magnification and measurement purpose as depicted in the bottom left inset of Fig. 4.3. A sharp image of the pendant drop with the needle is used to determine the pixels/mm in the captured image. The diameter of the needle used for the experiments and number of pixels/mm from the captured image are further used to determine the shape of the pendant drop. Five measurements on each sample of specific volume fraction are taken and the average surface tension of the corresponding suspension is determined.

4.2.3 Dynamic contact angle measurement

For the dynamic contact angle measurement, the sessile drop technique with the tangent method is used. In the tangent method, a mathematical expression is fitted to the interface of the sessile drop image and the contact angle for corresponding image is determined by the slope at the gas-solid-liquid interface (Ham, 2004). Although Young-Laplace fitting is a better option than the tangent method, the assumption of a symmetric drop is not necessarily fulfilled for the dynamic drop disposed from the needle. Hence, the tangent method with the polynomial curve fitting is used for the dynamic contact angle measurement. The dosing flow rate of the suspension to change the droplet volume is selected such that the equilibrium interface formation can take place. All experiments are performed under same environmental and operating conditions, with Borosilicate glass as the substrate material.

Advancing contact angle is measured with the increase in the volume of the drop as depicted in Fig. 4.2. The continuous increment in the drop volume is achieved by adding the microbead suspension with a constant dosing with help of a motorized syringe. During the entire measurement the needle remains attached to the drop. The portion of the needle inside the drop is maintained as small as possible so that, adhesion of microbead suspension particles to the needle surface is minimized. After setting up the DSA system for the contact angle measurements, the CCD camera is adjusted for an optimum image setting by obtaining a sharp needle image. A $10\mu\text{l}$ sessile drop, as shown in the bottom right inset of Fig. 4.3, is formed on the glass substrate prior to the measurement of the advancing contact angle. Further, the needle is inserted into the sessile drop and the microbead suspension is supplied with a constant flow rate of $150\mu\text{l}/\text{min}$. The advancement of the interface is captured with an in-built high speed CCD camera in the DSA system.

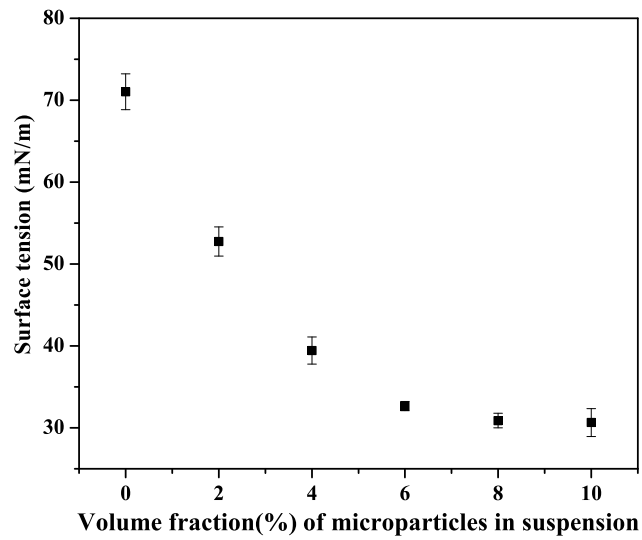
Receding contact angle is achieved by reducing the volume of the drop with the same dosing flow rate which is used in the advancing contact angle measurement. But the flow direction of the motorized syringe is reversed to obtain the reduction in the droplet volume. While selecting the maximum

size of the drop at the beginning of the measurement, the effect of gravity for the microbead suspension is neglected. It has been reported that, the contact angle with glass substrates is very sensitive with operating parameters, wetting conditions and the cleanliness of the glass (Bouaidat et al., 2005). Therefore, the glass substrate is cleaned with DI water and acetone and further dried with the nitrogen before the start of every set of experiment.

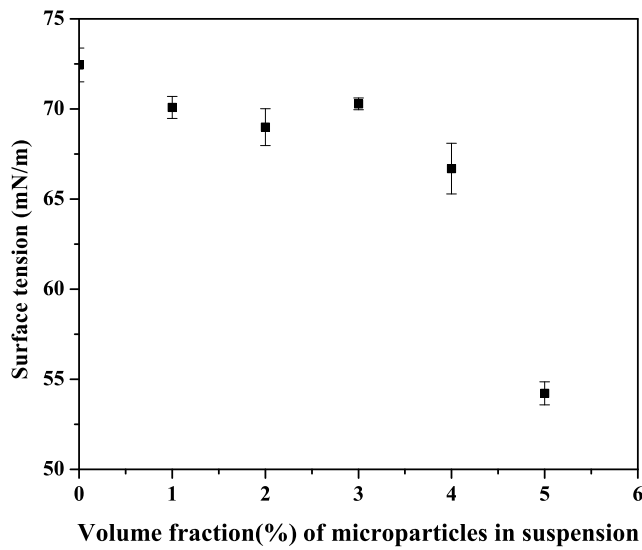
4.3 Results and discussion

The variation in the surface tension with the change in the microbead volume fraction is presented in Figs. 4.4(a) and 4.4(b) for Suspension A and Suspension B, respectively. Suspension A has a maximum 10% volume fraction whereas, for Suspension B it is 5%. In case of a Suspension A, exponential decay in the surface tension with an increment in the volume fraction is observed. Whereas, for Suspension B, beyond 3% volume fraction sudden decrement in the surface tension is observed. The decrease in the surface tension with the increment in the suspension volume fraction has also been observed in the existing literature for slurries (Brian and Chen, 1987; Kihm and Deignan, 1995). These current measurements suggest that, the surface tension of the microbead suspension decreases as the microbead volume fraction increases but the nature of the decrease varies from case to case. The error bars in Fig. 4.4 are generated based on the maximum and the minimum variation in the surface tension at a given volume fraction. This method generally over predicts random uncertainty but can be accepted as a conservative approach. The variation in the surface tension for a fixed volume fraction may be due to measurement error, instrumental error, local variation in the concentration of the microparticles, etc.

Although selected set of particles are of same diameter with a marginal difference in the standard deviation, the nature of decrement in the effective surface tension with the increment in the volume fraction is different from each other.



(a) Suspension A



(b) Suspension B

Figure 4.4: Variation in the surface tension with the change in the microbead volume fraction. Error bar reveals the range of maximum and minimum surface tension for corresponding measurement series.

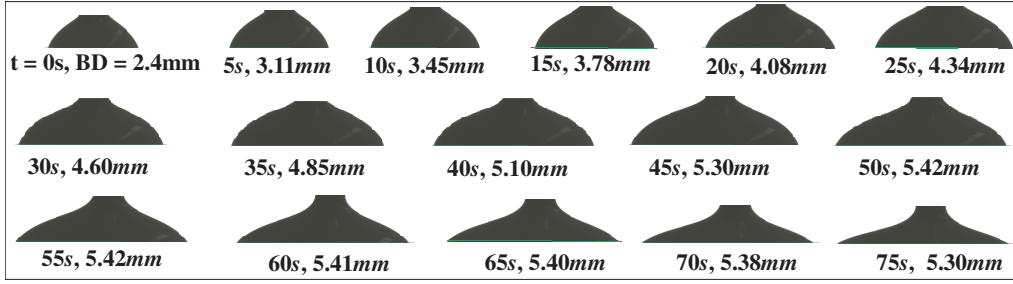


Figure 4.5: Images during the advancement and the recession of sessile drop on the glass substrate. Underneath numbers represent the corresponding time in seconds at which the image has been captured and the respective base diameter in millimeters.

This variation can be comprehended by understanding the rearrangement of microparticles at the fluid interface. As mentioned earlier, hydromechanical equilibrium condition of the pendant drop is a prior requirement for the measurement. Increase in the volume fraction changes the physical properties of the microbead suspension. In the pendant drop measurement technique, the surface tension is calculated based on the profile shape and physical properties particularly density of the hanging drop (del Río and Neumann, 1997). The increase in the volume fraction changes the density and size of the equilibrium drop. These changes in the density and the drop shape profile modify the surface tension. The difference in the nature of surface tension decrement curves needs to be understood from several other perspectives like interaction of the microparticle on the surface, preparation method of suspension, etc. The reduction in the surface tension may be due to the adsorption of microbeads on the drop surface. It is known that, under laboratory conditions, the adsorption of vapor and air at the interface tends to reduce the surface tension (Israelachvili, 1998). The change in the nature of decrease in the effective surface tension seems to be different because of difference in the cohesive and adhesive interaction between fluid molecules and microparticles (Bresme and Oettel, 2007). In case of Suspension A, when the volume fraction of microparticle reaches up to 6%, there is a strong probability of particles appearing at the air-fluid interface, which affects the interface profile. Further increase in

the volume fraction reduces the size of the equilibrium pendant drop. At the same time, such increase in volume fraction also reduces the available surface area at the interface for the microbeads to agglomerate, which limits the presence of microbeads at the interface. Therefore, marginal decrement in the effective surface tension has been observed beyond 6% which can be mainly contributed to the change in the density of the suspension. For Suspension B, up to volume fraction of 3%, the microparticle present in the suspension are not sufficient enough to agglomerate at the interface and hence insignificant amount of change in the equivalent surface tension has been observed. Beyond 3% volume fraction, particle concentration is sufficient enough to cause such agglomerate at the interface, which has a noteworthy effect on the surface tension. Further detailed investigation based on the theoretical analysis is needed to explore the nature of such decrement (Mi et al., 2009). In the present study, the emphasis is directed towards finding appropriate expressions for the effective wetting properties as a function of the microbead suspension volume fraction. Such expressions can then be readily incorporated in the theoretical analysis of capillary flow in microchannels and nanochannels.

The study of the change in the contact angle with the variation in the volume fraction is required to understand the wetting properties of the microbead suspension. Therefore, dynamic contact angle experiments are performed to measure the advancing and receding contact angles and subsequently the equilibrium contact angle is determined. Fig. 4.5 shows the contact line advancement and recession of Suspension A. For each image, the time instant and the corresponding base diameters are recorded. The advancement in the contact line can be observed up to 50s. Further, the flow is reversed but with the same flow rate as used for the advance contact angle measurements. In Fig. 4.5 the recession of the contact line can be observed between 50s and 75s. During the advancement of the drop, one can observe that the change in the base diameter is $1.08mm$ over time interval of $25sec.$, which roughly translates into a contact line velocity of $21.6\mu m/s$. Whereas during the recession, for the same time interval and flow rate, the decrement in the base diameter is $0.12mm$,

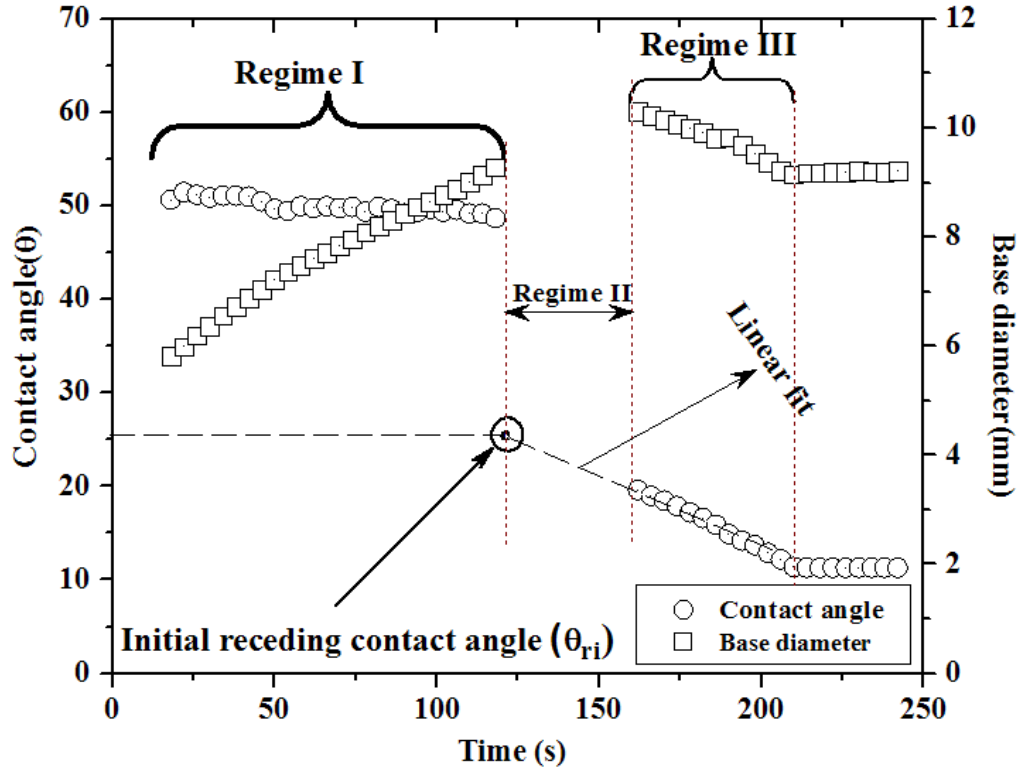


Figure 4.6: Measurement of average advancing and initial receding contact angle corresponding to the variation in the base diameter for Suspension B of 5% microbead volume fraction on the glass substrate.

which results in the contact line velocity of $2.4\mu\text{m}/\text{s}$. Hence, the contact line moves at a faster rate during the advancement as compared to the recession of the drop.

Neumann and co-workers (Lam et al., 2001, 2002; Hoorfar and Neumann, 2006), have extensively studied the contact angle hysteresis with different chemicals and surface combinations. In these reported studies, the measurement of dynamic contact angle is divided in three different transient regimes. Figure 4.6 shows the measurement of the dynamic contact angle and corresponding base diameter of Suspension B droplet with 5% volume fraction, where such trends are observed. These measurements are performed by processing the captured images, similar to those illustrated in Figure 4.5. The

variation in the base diameter of the sessile drop represents the change in the volume. Such distinct regime can be obtained by performing experiments at higher flow rate viz., $1000\mu l/min$ as done for this case. The first regime corresponds to the advancing contact angle in which an increase in the volume and subsequently in the base diameter of the droplet is observed until the flow direction is reversed. The advancing contact angle can be deduced by computing the average of the measured contact angle over the domain in which base diameter of the droplet increases temporally with the marginal change in the contact angle. A linear increment of the base diameter and corresponding advancing contact angle for Suspension B is observed in this case. The advancing contact angle can be determined by averaging the measured contact angles over the period of the increment in the base diameter i.e., over the Regime I as depicted in Fig. 4.6.

The receding contact angle measurement is performed by reversing the direction of the flow. During this process, initially the base diameter of the droplet remains same up to a certain time, beyond which the base diameter of the droplet starts decreasing. The Regime II is the domain in which the base diameter is unchanged in spite of the reduction in the suspension volume. In Regime III, simultaneous reduction in the base diameter and the change in the contact angle can be observed. In Fig. 4.6, the contact angles and the base diameters for the Regime II are not presented because of the random fluctuations in contact angles. It is to be noted that, for Regime II, Neumann and co-workers (Lam et al., 2001, 2002; Hoorfar and Neumann, 2006) have observed a constant base diameter. However, in this present study, it is observed that there is a difference between the base diameters at the beginning of Regime III and at the end of Regime I. This may be due to the fact that the drop volume does not decrease immediately after reversing the flow direction. The mechanical delay in the response of the instrument creates the time lag during which the volume of the drop might have increased in the Regime II and subsequently there is an increment in the the base diameter. In case of receding contact angles, different variations are observed in literature (Lam

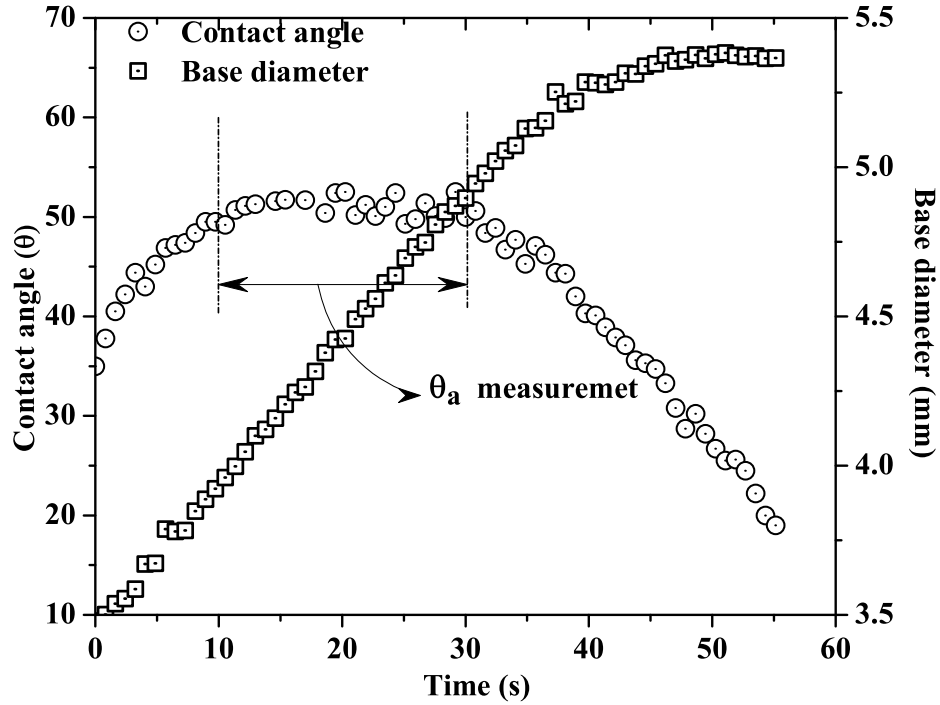


Figure 4.7: Measurement of an average advancing and minimum receding contact angle with corresponding to the variation in the base diameter for the Suspension A of 10% microbead volume fraction on the glass substrate.

et al., 2001, 2002), viz; fluctuating, constant and no receding contact angles. Hence, it is difficult to determine the precise value of the average receding contact angle. Therefore for such cases (Lam et al., 2001, 2002), the initial receding contact angles i.e., θ_{ri} is measured to determine the hysteresis. In case of dynamic receding contact angles, as shown in Fig. 4.6, θ_{ri} can be determined by extrapolating the line which approximately fits the receding contact angle trend for the Regime III to the point where it intersects the Regime I (Lam et al., 2002). It is to be noted that the illustration of θ_{ri} in Fig. 4.6 is to demonstrate the similar trend as observed by Neumann and co-workers (Lam et al., 2001, 2002; Hoorfar and Neumann, 2006) and is not being incorporated in the calculation of the equilibrium contact angle.

The main purpose of the present study is to investigate the variation in the equilibrium contact angle with the change in the microbead suspension volume fraction. There are several parameters which can affect the contact angle hysteresis and hence it is difficult to determine the average receding contact angle (Extrand, 2006), but one can obtain the minimal contact angle during the recession of the contact line. An equilibrium contact angle for a suspension of particular volume fraction can be determined from the knowledge of an average advancing contact angle and a minimal receding contact angle (Tadmor, 2004). Figure 4.7, shows the variation in the contact angle of Suspension A with 10% volume fraction corresponding to the change in the volume of the drop. Similar behavior in the dynamic contact angle variations is observed for all selected samples under same experimental operating conditions. Three sets of experiments on same volume fraction suspension are performed and an average of these three results are considered for further calculations.

The change in the advancing and receding contact angles for Suspension B with the variation in the volume fraction is presented in the Fig. 4.8. The decrement in the advancing and receding contact angles with an increment in the volume fraction is observed. Similar procedure is followed for the Suspension A and the average advancing and receding contact angles are determined for each volume fraction. Further, the equilibrium contact angle is determined based on the average advancing and receding contact angles (Tadmor, 2004). Figures 4.9(a) and 4.9(b) demonstrate the variation in the equilibrium contact angle of Suspension A and Suspension B, respectively. As observed for advancing and receding contact angles, the equilibrium contact angle also decreases with the increase in the volume fraction. In case of a nanoparticle suspension, the combination of increment and decrement in the contact angle is observed in the literature (Sefiane et al., 2008; Vafaei et al., 2006). The ‘lubricating effect’ and the concept of ‘structural disjoining pressure’ are introduced to support the increment and decrement in the contact angle. In the present study, wettability of the suspension increases as the suspension volume fraction increases which can be attributed to the three different interactions

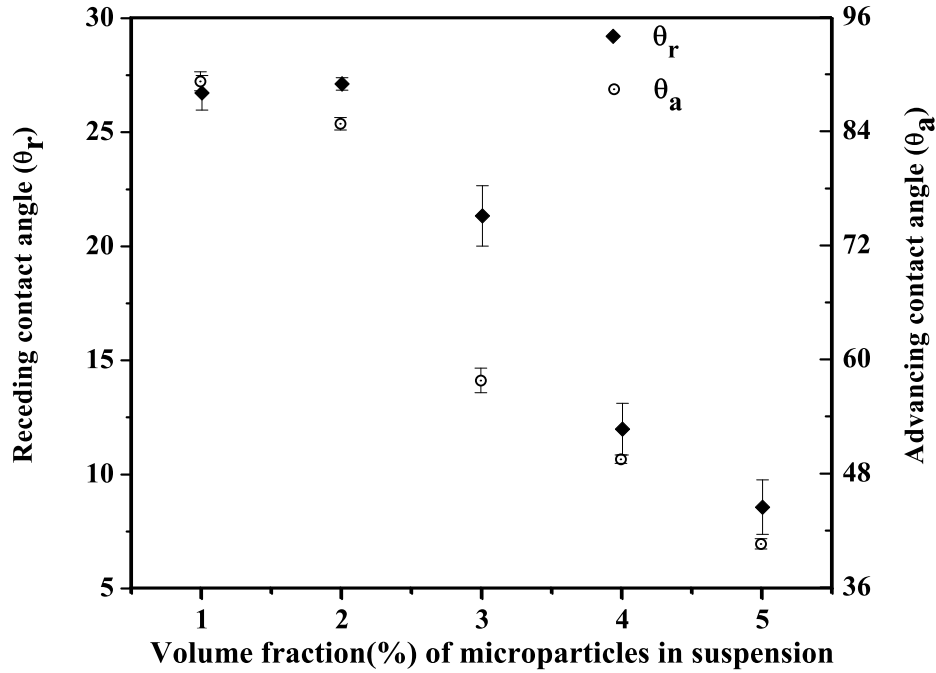
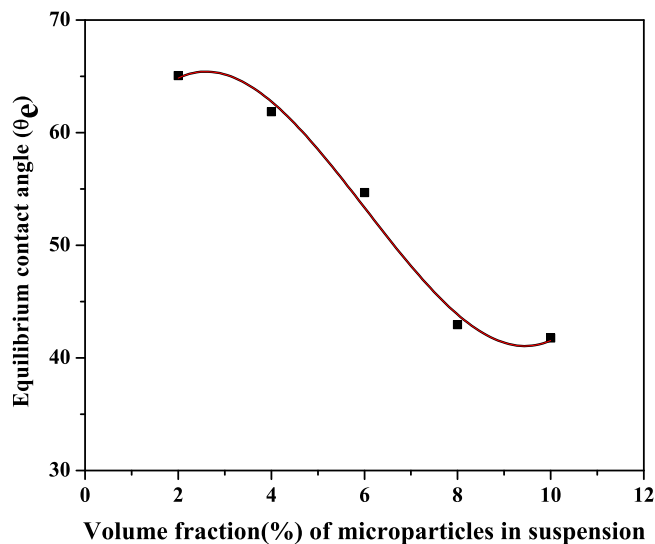


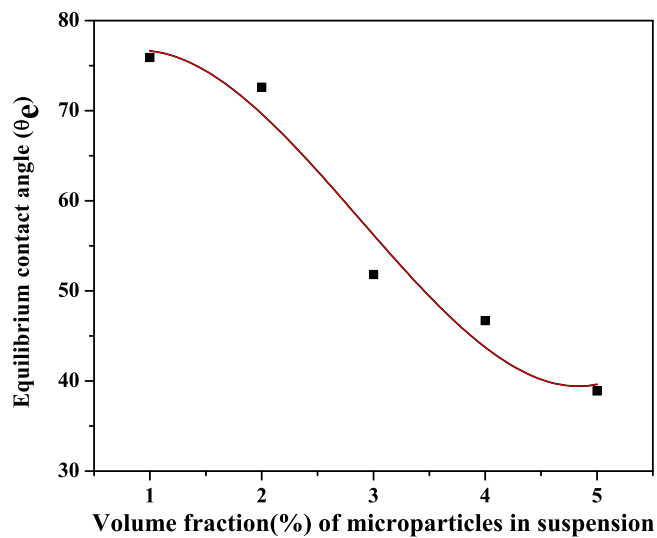
Figure 4.8: Variation in the advancing and receding contact angle of Suspension B with the change in the microbead volume fraction on the glass substrate. Error bar reveals the range of maximum and minimum contact angles for corresponding measurement series.

viz; particle-particle, particle-substrate and particle-fluid interactions.

In the case of a microbead suspension, during the advancement and the recession of the contact line, the three types of interactions might take place. For the perfect wetting condition, the fluid and the substrate interaction has least resistance. The microbead suspension wetting is not only governed by the fluid-substrate interaction but also the interaction between microbeads can play an important role. The present experimental results suggest that, the suspension with low volume fraction of microbeads retards the contact line motion. Whereas, an increment in the volume fraction of the microbead suspension results in an increment in the advancement of the contact line. Hence, for observed combination of microbead suspension and substrate, the



(a) Suspension A



(b) Suspension B

Figure 4.9: Variation in the equilibrium contact angle with the microbead volume fraction on the glass substrate for two different microbead suspensions. Solid lines represent the corresponding curve fitted expressions, reported in Table 4.1

microbead-substrate interaction provides less resistance to the advancement or recession of the contact line as compared to the fluid-surface interaction.

Table 4.1: Correlations for contact angle and surface tension using curve fitting to the measurement values over the range of the volume fraction expressed in percentage. The values in the parenthesis represent the corresponding coefficient of determination of the curve.

Range of volume fraction(ϕ) of microbeads	Expression	
	σ	θ
$\underbrace{0 - 0.1}_{\text{Suspension A}}$	$44.89 \exp\left(\frac{-\phi}{2.95}\right)$ $+27.41_{(0.9879)}$	$0.152\phi^3 - 2.74\phi^2$ $+11.13\phi + 52.31_{(0.9863)}$
$\underbrace{0 - 0.05}_{\text{Suspension B}}$	$-0.005 \exp\left(\frac{-\phi}{0.611}\right)$ $+70.71_{(0.9923)}$	$1.24\phi^3 - 10.63\phi^2$ $+16.29\phi + 69.75_{(0.9863)}$

In passive microfluidic applications, which are mainly based on the capillary flow phenomena, the contact angle plays a vital role while predicting the performance of the device. Passive microfluidic devices are becoming emerging options in LOC and MEMS devices (Lim et al., 2007). Transport of several biomolecules in such microfluidic devices is generally achieved with biomolecule coated microbeads (Yun et al., 2009). Hence, it is important to know the change in the physical properties due to inclusion of the microbeads in the suspension. The viscosity and the density of suspensions can be determined with the available expressions from the literature (Hiemenz and Rajagopalan, 1997), but no such expressions for modified or equivalent surface tension and equilibrium contact angle are readily available. From the current experimental data, one can extract such expressions for surface tension and contact angle by using an appropriate curve fitting to the measured values over the range of the volume fraction under consideration. For the range of volume fraction and microbead suspensions used in the present study, the appropriate correlations for contact angle and surface tension are provided in Table 4.1. For representing the agreement between the curve fitted polynomial expressions and experimentally reported values, the coefficient of the determi-

nation (COD) is calculated and reported in Table 4.1. The CODs for different types of curve fittings like exponential, second order, third order polynomial, etc., are determined and the best-fit with the maximum COD is selected to depict the correlations. Such expressions for the variation in contact angle and the surface tension with volume fraction can be readily used in modeling of transport processes of microbead suspensions in micro-capillaries used in LOC devices (Waghmare and Mitra, 2010b). It is to be noted that, correlations presented in the Table 4.1 are case specific but can be used for the combination of polystyrene microparticles suspension and glass for the given range of volume fraction.

4.4 Conclusion

The present study reports an experimental investigation of equilibrium contact angles and surface tension of microbead suspensions. The variation in the advancing and receding contact angles are measured for suspensions of different microbead volume fractions. Further the variation in the equilibrium contact angle with the change in the microbead volume fraction is observed. The effect of microbead volume fraction on the surface tension is also studied. From the experimental results following important conclusions can be made:

- The surface tension of the microbead suspension decreases as the microbead volume fraction in the suspension increases.
- The advancement of the microbead suspension drop is higher as compared to the recession of the drop under same operating condition and time interval.
- The equilibrium contact angle based on advancing and receding contact angles decreases as the microbead volume fraction increases in the suspension.
- For the considered combination of the microbead suspension and the substrate, microbeads in the suspension assist to the advancement and

the recession of the contact line.

- These measurements confirms that the contact angle and the surface tension depends on the volume fraction of the microbeads in suspensions.
- Empirical correlations for surface tension and contact angle are proposed in terms of microbead volume fraction.

References

- Adamson A. W. and Gast A. P., *Physical Chemistry of Surfaces, Sixth Edition*. John Wiley, 1997.
- Bouaidat S., Hansen O., Bruus H., Berendsen C., Bau-Madsen N. K., Thomsen P., Wolff A., and Jonsmann J., Surface-directed capillary system; theory, experiments and applications. *Lab on a Chip - Miniaturisation for Chemistry and Biology*, 5(8):827–836, 2005.
- Bresme F. and Oettel M., Nanoparticles at fluid interfaces. *Journal of Physics Condensed Matter*, 19(141):413101, 2007.
- Brian B. and Chen J., Surface tension of solid-liquid slurries. *American Institute of Chemical Engineers*, 33(2):316–318, 1987.
- Butt J.-H., Graf K., and Kappl M., *Physics and Chemistry of Interfaces*. Wiley-VCH, Weinheim-VCH GmbH & Co. KGaA, 2003.
- Chau T. T., A review of techniques for measurement of contact angles and their applicability on mineral surfaces. *Minerals Engineering*, 22(3):213–219, 2009.
- Chau T. T., Bruckard W. J., Koh P. T. L., and Nguyen A. V., A review of factors that affect contact angle and implications for flotation practice. *Advances in Colloid and Interface Science*, 150(2):106–115, 2009.
- Cho E., Kim D., and Cho K., Contact angles of oils on solid substrates in aqueous media: Correlation with afm data on protein adhesion. *Langmuir*, 24(18):9974–9978, 2008.

- del Río O. and Neumann A., Axisymmetric drop shape analysis: Computational methods for the measurement of interfacial properties from the shape and dimensions of pendant and sessile drops. *Journal of Colloid and Interface Science*, 196(2):136–147, 1997.
- Drelich J., Miller J. D., and Good R. J., The effect of drop (bubble) size on advancing and receding contact angles for heterogeneous and rough solid surfaces as observed with sessile-drop and captive-bubble techniques. *Journal of Colloid and Interface Science*, 179(1):37–50, 1996.
- Edgerton H. E., Hauser E. A., and Tucker W. B., Studies in drop formation as revealed by the high-speed motion camera. *Journal of Physical Chemistry*, 41(7):1017–1028, 1937.
- Extrand C. W., Water contact angles and hysteresis of polyamide surfaces. *Journal of Colloid and Interface Science*, 248(1):136–142, 2002.
- Extrand C. W., Hysteresis in contact angle measurements. *Encyclopedia of Surface and Colloid Science*, 1(1):2876–2891, 2006.
- Girault H. H. J., Schiffrin D. J., and Smith B. D. V., The measurement of interfacial tension of pendant drops using a video image profile digitizer. *Journal of Colloid And Interface Science*, 101(1):257–266, 1984.
- Grigoriev D. O., Krägel J., Dutschk V., Miller R., and Möhwald H., Contact angle determination of micro- and nanoparticles at fluid/fluid interfaces: The excluded area concept. *Physical Chemistry Chemical Physics*, 9(48):6447–6454, 2007.
- Gu P. Y., Contact angle measurement techniques for determination of wettability. *Encyclopedia of Surface and Colloid Science*, 1(1):1525–1539, 2006.
- DSA 100 drop shape analysis, software manual, Krüss GmbH Hamaburg.* Hamaburg, 2004.

- Hayes R. A., Robinson A. C., and Ralston J., A wilhelmy technique for the rapid assessment of solid wetting dynamics. *Langmuir*, 10(8):2850–2852, 1994.
- Hiemenz P. C. and Rajagopalan R., *Principles of Colloid and Surface Chemistry*. CRC Press,, 1997.
- Hilpert M. W. and Ben-David A. W. Infiltration of liquid droplets into porous media: Effects of dynamic contact angle and contact angle hysteresis. *International Journal of Multiphase Flow*, 35(3):205–218, 2009.
- Hoorfar M. and Neumann A., Recent progress in axisymmetric drop shape analysis (ADSA). *Advances in Colloid and Interface Science*, 121(1):25–49, 2006.
- Hörvölgyi Z., Németh S., and Fendler J. H., Spreading of hydrophobic silica beads at water-air interfaces. *Colloids and Surfaces A: Physicochemical and Engineering Aspects*, 71(3):327–335, 1993.
- Hsieh C. T., Wu F. L., and Chen W. Y., Contact angle hysteresis and work of adhesion of oil droplets on nanosphere stacking layers. *Journal of Physical Chemistry C*, 113(31):13683–13688, 2009.
- Israelachvili J. N., *Intermolecular and surface forces*. Academic Press, 1998.
- Karniadakis G., Beskok A., and Aluru N., *Microflows and Nanoflows Fundamentals and Simulation*. Springer Berlin, New York, 2005.
- Kawaguchi H. ., Functional polymer microspheres. *Progress in Polymer Science*, 25(8):1171–1210, 2000.
- Kihm K. D. and Deignan P., Dynamic surface tension of coal-water slurry fuels. *Fuel*, 74(2):295–300, 1995.
- Kwok D. Y., *Contact angles and surface energetics*. PhD thesis, University of Toronto, 1998.

- Lam C. N. C., Kim N., Hui D., Kwok D., Hair M. L., and Neumann A. W., The effect of liquid properties to contact angle hysteresis. *Colloids and Surfaces A: Physicochemical and Engineering Aspects*, 189(1-3):265–278, 2001.
- Lam C. N. C., Wu R., Li D., Hair M. L., and Neumann A. W., Study of the advancing and receding contact angles: Liquid sorption as a cause of contact angle hysteresis. *Advances in Colloid and Interface Science*, 96(1-3):169–191, 2002.
- Lim C. T., and Zhang Y., Bead-based microfluidic immunoassays: The next generation. *Biosensors and Bioelectronics*, 22(7):1197–1204, 2007.
- Macdougall G. and Ockrent C., Surface energy relations in liquid/solid systems- i. the adhesion of liquids to solids and a new method of determining the surface tension of liquids. *Proceedings of Royal Society A*, 180(981):151–173, 1942.
- Mi J., He Y., and Zhong C., Theoretical study of wetting behavior of nanoparticles at fluid interfaces. *AIChE Journal*, 55(3):747–755, 2009.
- Munshi A. M., Singh V. N., Kumar M., and Singh J. P., Effect of nanoparticle size on sessile droplet contact angle. *Journal of Applied Physics*, 103(8):084315, 2008.
- Nguyen N. and Werely S., *Fundamentals and Applications of Microfluidics*. Artech House, New York, 2003.
- Rupp F., Scheideler L., and Geis-Gerstorfer J., Effect of heterogenic surfaces on contact angle hysteresis: Dynamic contact angle analysis in material sciences. *Chemical Engineering and Technology*, 25(9):877–882, 2002.
- Sarkar N. and Gaudin A. M., Hysteresis of contact angle in the galena-water-nitrogen system. *Journal of Physical Chemistry*, 70(8):2512–2517, 1966.
- Sefiane K., Skilling J., and MacGillivray J., Contact line motion and dynamic wetting of nanofluid solutions. *Advances in Colloid and Interface Science*, 138(2):101–120, 2008.

- Tadmor R., Line energy and the relation between advancing, receding, and young contact angles. *Langmuir*, 20(18):7659–7664, 2004.
- Derivation of Count per Millimeter from Percentage of Solids*. Technical Note: TN-017.04, Thermo Fisher Scientific, 2008.
- Vafaei S., Borca-Tasciuc T., Podowski M. Z. , Purkayastha A., Ramanath G., and Ajayan P. M., Effect of nanoparticles on sessile droplet contact angle. *Nanotechnology*, 17(10):2523–2527, 2006.
- Verpoorte E., Beads and chips: New recipes for analysis. *Lab-on-a-chip*, 3(4): 60–68, 2003.
- Waghmare P. R. and Mitra S. K., Finite reservoir effect on capillary flow of microbead suspension in rectangular microchannels. *Journal of Colloid and Interface Science*, 351(2):561–569, 2010a.
- Waghmare P. R. and Mitra S. K., Modeling of combined electroosmotic and capillary flow in microchannels. *Analytica Chimica Acta*, 663(2):117–126, 2010b.
- Walker G. M. and Beebe D. J., A passive pumping method for microfluidic devices. *Lab on a Chip - Miniaturisation for Chemistry and Biology*, 2(3): 131–134, 2002.
- Wang X., Chen Z., and Shen Z., Dynamic behavior of polymer surface and the time dependence of contact angle. *Science in China, Series B: Chemistry*, 48(6):553–559, 2005.
- Woche S. K., Goebel M. O., Kirkham M. B., Horton R., Van-der Ploeg R. R., and Bachmann J., Contact angle of soils as affected by depth, texture, and land management. *European Journal of Soil Science*, 56(2):239–251, 2005.
- Young T., An essay of the cohesion of fluids. *Philosophical Transaction of the Royal Society of London*, 95:65–87, 1805.

Yun K., Lee D., Kim H.-S. , and Yoon E., Multifunctional microwell plate for on-chip cell and microbead-based bioassays. *Sensors and Actuators B-Chemical*, 143(1):387-394, 2009.

Chapter 5

Contact angle hysteresis of Bovine Serum Albumin (BSA) solution/metal (Au-Cr) coated glass substrate¹

5.1 Introduction

The multifunctional capability of microfabricated devices introduced a new era in immunosensing devices. These microfabricated immunosensing devices are generally known as lab-on-chip (LOC) or micro total analysis system ($\mu - TAS$). In such LOC or $\mu - TAS$ the biomolecules are mainly transported for separation, mixing or detection purposes (Lim et al., 2007). In microscale devices surface forces are dominant compared to the body forces which can be utilized to transport the biomolecules along the microchannels (Waghmare and Mitra, 2012, 2010b,c; Nguyen and Werely, 2003; Saha and Mitra, 2009a; Saha et al., 2009; Stone et al., 2004). The pumping based on the capillary flow has been successfully used to transport biomolecules in microfluidic applications, which is widely termed as passive pumping or autonomous pumping approach (Juncker et al., 2002; Walker and Beebe, 2002; Zimmermann et al., 2007). Wetting properties like interfacial surface tension and contact angle of fluid depict the limit of passive pumping. Hence, it is important to know about

¹ A version of this chapter has been published. Waghmare and Mitra, 2012, Colloid and Polymer Science, DOI: 10.1007/s00396-012-2756-1

the wetting properties of biomolecules suspensions relevant to immunosensing or LOC devices.

Albumin is a plasma protein which is abundantly available in human blood. Bovine Serum Albumin (BSA) is often used in experiments as a substitute for actual human body fluids like blood. Hence, it is often easier to perform microfluidic experiments with BSA rather than actual bio-fluids, like blood, which can cause blockage of the narrow microfluidic channels (Peters, 1995). If the passive pumping with capillarity is the pumping mechanism, then wetting properties need to be understood. Existing literature suggests that there is a detailed study on interactions of proteins at the liquid-air interface. Neumann and co-workers (Chen et al., 1998) reported that the surface tension of protein solution varies with the temperature and concentration of protein solution. They have used a wide range of concentration to study the variation in the equilibrium surface tension which decreases as the concentration of protein increases. Even though the interaction of proteins with the fluid is well developed, but the quantification of the contact angle with the change in the concentration of the protein is still limited. Therefore, in this work the wetting properties of BSA solutions with the variation in the BSA concentration are studied in detail.

Different techniques are used to determine the contact angle and surface tension. Most commonly adopted and reliable techniques are pendant and sessile drop techniques for surface tension and contact angle measurements respectively (Israelachvili, 1998; Lam et al., 2001). The intermolecular interaction at the three-phase contact line of the sessile drop is dictated by the surface tension and contact angle. The three-phase contact line is the locus where all three phases - gas, liquid and solids co-exist. The surface tension represents the magnitude of intermolecular interaction at the contact line, whereas the contact angle represents the direction of the intermolecular interaction (Hiemenz and Rajagopalan, 1997). At an equilibrium condition, the contact angle is termed as a static or equilibrium contact angle (Young, 1805). The chemical composition, roughness and orientation of surface also af-

fect the equilibrium contact angle and describing wetting of liquid under such conditions has been an area of research over the last decade. Currently, the exact determination of an equilibrium contact angle under such conditions with different solid-liquid combinations is of interest to a number of researchers. Recently, Bormashenko (Bormashenko, 2011) has presented the general equation for wetting of rough surfaces. The magnitude of contact angle can also be affected by several other parameters like intermolecular interactions among three phases, surface heterogeneity, mode of liquid deposition, etc. (Lam et al., 2001). These parameters affect the contact angle, hence in experimental studies, there is always an inconsistency in the magnitude of the contact angle (Waghmare and Mitra, 2010a; Kwok, 1998). Therefore, the dynamic contact measurements, i.e., the hysteresis in the contact angle needs to be considered during the measurement of the equilibrium contact angle.

The characterization of the wetting behavior of the BSA solution with dynamic contact angle measurements is the key part of this study. The detailed coverage of studies and development in the use of contact angle hysteresis for multicomponent systems can be found elsewhere (Chau, 2009; Waghmare and Mitra, 2010a; Extrand, 2006). In most of these reported studies, the contact angle hysteresis is computed for different combinations of liquid solutions with different substrates. As mentioned earlier, in most of the LOC and μ -TAS applications the biomolecules are carried with BSA solution. Therefore, it is important to investigate the wetting properties of BSA solution with the variation in the concentration of the BSA. In the next section, the experimental details for contact angles and surface tension measurements are described. The contact angle hysteresis with BSA solution is presented in the next section and finally the findings of this experimental study are reported.

5.2 Experimental details

A Krüss DSA 100 (Krüss GmbH, Hamburg, Germany) system was used to measure the contact angles and surface tension. The static and dynamic contact angles of BSA solutions on the metal (Au-Cr) coated glass substrate were

measured and the BSA solution interfacial surface tension was also determined. The BSA solutions with the variation in the BSA concentration were prepared by adding the BSA powder (A7906, Sigma-Aldrich, USA) into the DI water. The BSA concentration was varied by varying the amount of the BSA powder in the DI water, which varied from 2 mg/ml to 10 mg/ml.

5.2.1 Surface characterization

The roughness of metal coated glass substrate was measured using an optical profilometer (Zygo). Figure 5.1 shows the surface profile and surface roughness of the substrate obtained with the optical profilometer. The profilometer is operated with 10X lens and has 0.1nm (root mean square) roughness resolution. An approximate area of $750\mu m \times 550\mu m$ was scanned at 5 random locations of the substrate. It was observed that the length scale of surface roughness was in the order of a few nm (maximum valley depth 0.95 nm and maximum peak height 1.75 nm). The aim of the present study was to determine the variations in the contact angle as the BSA concentration increased. Hence, the effect of nanoscale roughness on the contact angle was neglected in the present analysis.

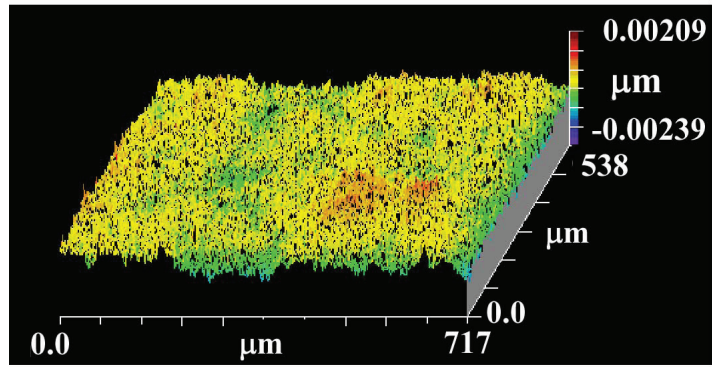
5.2.2 Surface tension and contact angle measurements

The interfacial tension of BSA solution was measured with the pendant drop technique whereas for the contact angle measurements, a sessile drop was deposited on the glass substrates. Images of sessile and pendant drops in equilibrium conditions were captured and the contact angle and surface tension values were determined using an image processing software. An in-built software in the Krüss DSA 100 system was used for image processing (Girault et al., 1984; Ham, 2004). The shape factor for pendant drop profile from image processing was determined, which was further used to determine the surface tension. Whereas, from a captured sessile drop image the corresponding contact angle was determined by positioning the tangent along the interface through the point of the three-phase junction. Experimental method-

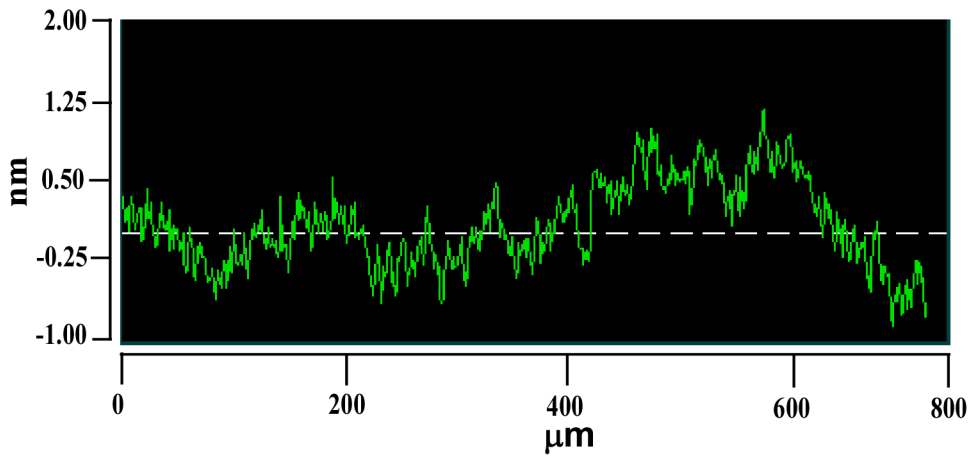
ology and corresponding details have been given elsewhere (Waghmare and Mitra, 2010a).

5.3 Results and discussion

Figure 5.2 shows the variation in the surface tension of the BSA solution with respect to the change in the concentration of the BSA in the solution. Five measurements on each BSA solution of specific concentration were taken and the average surface tension of the corresponding solution is presented with the error bars. It is observed that the BSA in the DI water affects the air-liquid interface, which, in turn, reduces the surface tension. It is reported in the literature that adsorption at the interface has a significant role on the surface tension and this has also been experimentally demonstrated (Israelachvili, 1998). These measurements suggest that surface tension of the BSA solution decreases as the concentration of solution increases, which represents the surface activity of BSA. Similar observation for Human Serum Albumin (HSA) has been reported by Neumann and co-workers (Chen et al., 1998). In their study, the variations in the surface tension for 15 concentrations from 1×10^{-4} to 10 *mg/ml* were studied. The decrement in the surface tension with the increment in concentration was observed. It was also reported that the surface tension remains unchanged above 0.05*mg/ml*. Figure 5.2 shows that mostly the surface tension decreases linearly for a wide range of concentration whereas for a smaller range, the nature of the decrement is nonlinear. It is to be noted that in case of BSA the surface tension does not remain constant for higher concentrations as observed for HSA. The diffusion of protein to the interface increases as the protein concentration increases which contributes towards the decrement in the surface tension. Young proposed the relationship between the surface tension of liquid and the contact angle (Young, 1805) and if the Young's hypothesis is applied to a given system, then the decrement in the surface tension may affect the contact angle as well. Therefore, it is interesting to study the variation in the contact angle with the change in the concentration of BSA solution.



(a) Surface profile



(b) Surface roughness

Figure 5.1: The surface roughness measurements of the metal coated glass substrate with an optical profilometer. The surface profile of the scanned area is presented in (a) and, (b) represents the surface roughness of the corresponding area of the substrate.

The variation in the static contact angle with the variation in the BSA concentration is presented in Fig. 5.3. The static contact angle of BSA solution decreases with the increment in the concentration of BSA. As mentioned earlier, the diffusion of protein towards the interface increases with the increase in the bulk concentration. It is demonstrated in the literature that during the evaporation process, biomolecules like proteins and cells deposit at the contact line, which is explained as another form of “coffee ring effect” (Wong et al., 2011). In case of BSA solution, the deposition of protein at the contact line might have increased with the increment in the concentration. This

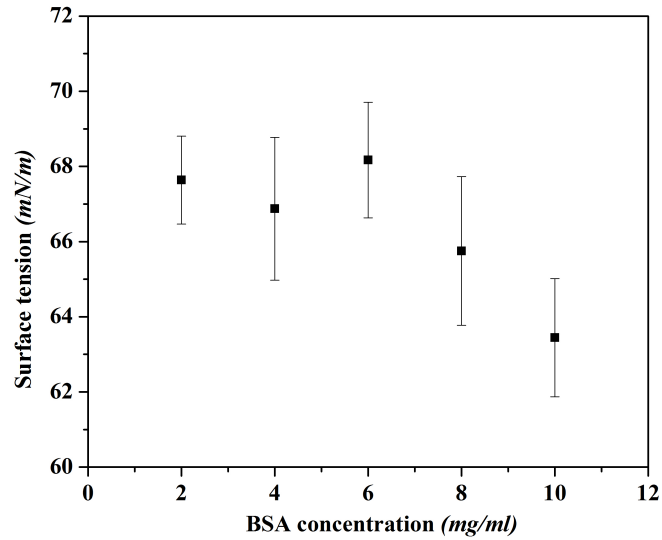


Figure 5.2: The variation in the surface tension with the change in the BSA concentration. Error bar reveals the range of maximum and minimum surface tension for the corresponding measurement series.

cluster of deposited protein at the contact line can be considered as a hurdle for further motion of the contact line. Therefore, the increment of the contact angle with the increase in BSA concentration is observed. Five measurements on each sample of specific concentration were taken and the average static contact angle of the corresponding concentration was determined. The error bar represents the maximum and minimum static contact angle for the corresponding measurement series. It is to be noted that the error bar of each measurement series overlaps on the successive measurement series error bar. The minimum static contact angle obtained for 6 mg/ml concentration is lower than the average static contact angle of 4mg/ml concentration solution. Hence, the static contact angle measurements are not the exact representation of the actual wettability conditions. Therefore, it is necessary to study the contact angle hysteresis from dynamic contact angle measurements. One may argue that the error bars presented in Fig. 5.2 also overlap with each other. Therefore, for surface tension measurements, the dynamic measurements also

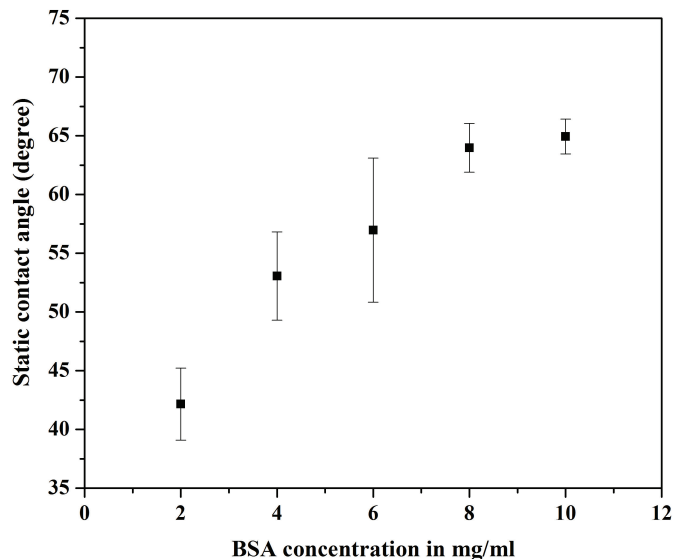


Figure 5.3: The variation in the static contact angle with the change in the BSA concentration. Error bar reveals the range of maximum and minimum static contact angle for the corresponding measurement series.

need to be performed. The equilibrium surface tension along with dynamic surface tension measurement for albumin have already been reported in the literature (Chen et al., 1998). However, to the best of authors' knowledge, the equilibrium contact angle along with the dynamic contact angle measurements have not been reported in the literature. Hence, in this study the emphasis has been given to the measurement of equilibrium contact angle considering the contact angle hysteresis.

Different techniques for measurement of dynamic contact angle or contact angle hysteresis have been developed (Chau, 2009). There are different techniques used to measure the contact angles viz., Wilhelmy plate, inclined plate and sessile drop technique. The advantages, disadvantages and appropriate applications for these techniques can be found in detail elsewhere (Gu, 2006; Hayes et al., 1994; Macdougall and Ockrent, 1942). In the Wilhelmy technique, the height of liquid rise due to capillarity along a vertical plate of a particular solid represents the static contact angle (Hayes et al., 1994), whereas the drop

on the inclined plate provides the advancing and receding contact angles which are essentially static ones (de Gennes et al., 2003; Marmur, 2009). The dynamic contact angles are always associated with the moving drops. Therefore, in this study, sessile drop or needle-in-drop technique is used to analyze the contact angle hysteresis. In such measurements the advancing and receding contact angles of the sessile drop are measured with the advancement and recession of the contact line. The advancement and recession of the contact line is achieved by increasing and decreasing the sessile drop volume, respectively. This change in the drop volume is obtained with the help of a motorized syringe where the needle of the syringe is always kept inside the sessile drop. For the increment in the drop volume, the liquid is pumped into the drop whereas for the decrement in the drop volume the liquid is pumped out from the drop. The magnitude of the flow rate is the same during the increment and decrement of the drop volume. One can find more experimental details, like initial drop volume, volume flow rate, etc., for such measurements in our previous study (Waghmare and Mitra, 2010a).

One measurement series of dynamic contact angle for BSA solution of concentration 6mg/ml is presented in Fig. 5.4. The transient variations in the base diameter, contact angle and drop volume of sessile drop are presented in Figures 5.4 (a), (b) and (c), respectively. Generally, such transient variations are divided into three different domains viz., advancing domain, transition domain, and receding domain. The advancing domain is characterized by the contact angle whereas the base diameter is used to characterize other two domains. It has also been reported that in such dynamic contact angle measurements, four types of patterns can be obtained, which are typically dependent on the type of liquid and solid surface on which measurements are performed. These four patterns are categorized based on the transient response of the receding contact angle and these four patterns are: decrement in the contact angle, constant receding contact angle, stick/slip pattern, and non-receding contact angle (Chen et al., 1998; Lam et al., 2002). The ‘extrapolation approach’ is generally used to determine the receding contact angle in the needle-in-drop

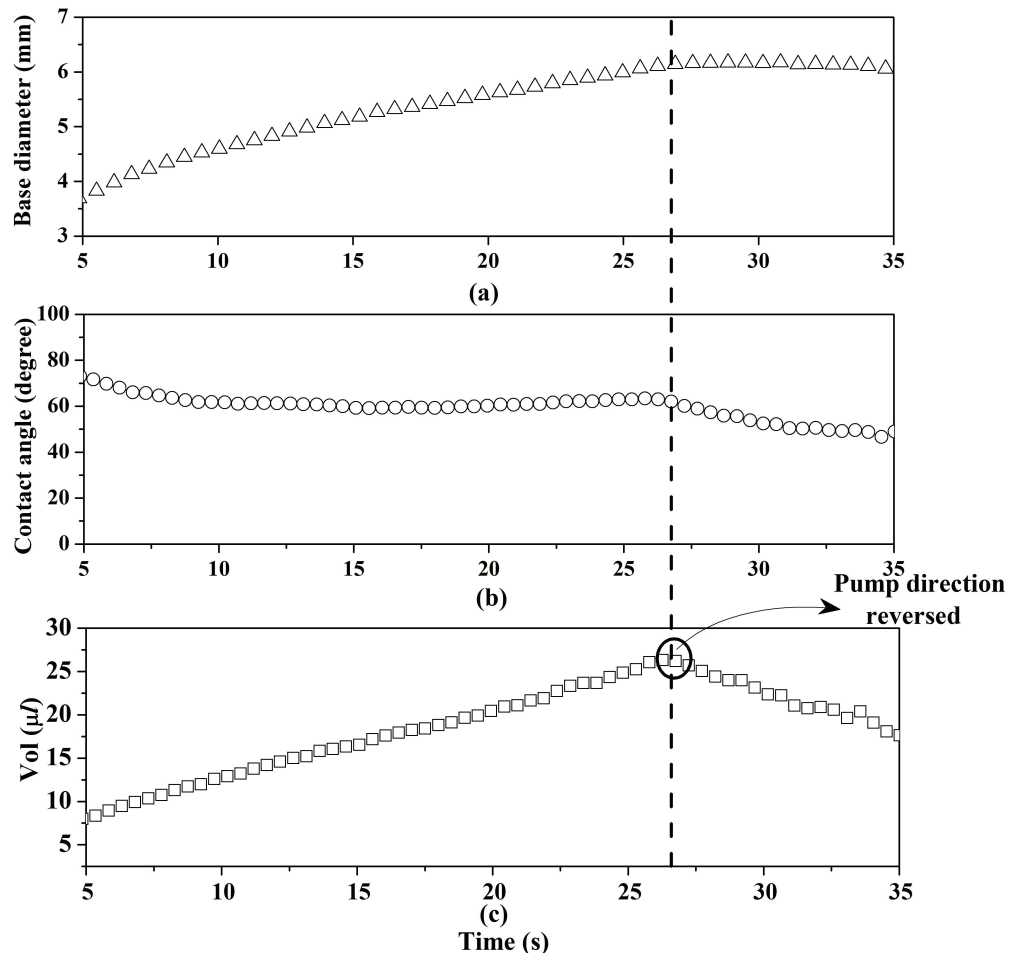


Figure 5.4: The variations in the base diameter, contact angle, and volume of the sessile drop corresponding to the particular measurement series. The encircled point represents the time at which decrement in the drop volume starts.

dynamic contact angle measurements. In this approach the receding contact angle pattern is curve fitted and the fitted curve is extrapolated back to the point where the receding of the contact line is initiated in experiments, i.e. at the point where the pump direction is reversed (Waghmare and Mitra, 2010a; Lam et al., 2002). This angle is considered as the initial receding contact angle and is further used for the calculation of equilibrium contact angle. The equilibrium contact angle can be determined from the knowledge of average advancing and receding contact angles, based on the analysis reported by Tadmor (Tadmor, 2004). The expression for the equilibrium contact angle presented by Tadmor (Tadmor, 2004) is derived similarly to the Young's thermodynamic approach. Instead of the equilibrium contact angle, an arbitrary contact angle from a spectrum of contact angles between advancing and receding contact angles is considered for the analysis. For attaining an arbitrary contact angle an additional energy along the contact line is considered for the minimization of the energy and the expression for an equilibrium contact angle based on the advancing and receding contact angles is derived. The proposed expression is validated with the experimental results of advancing and receding contact angles (Lam et al., 2002).

The variations observed in Fig. 5.4 represent non-receding contact angle pattern where the base diameter remains approximately the same in spite of the reduction in the drop volume as depicted in Fig. 5.4 (a). The encircled point in Fig. 5.4 (c) shows the instant at which the decrement in the drop volume is achieved by reversing the pump direction. Since there is non-receding contact angle pattern, the extrapolation approach cannot be used in this case. The contact angle hysteresis using the needle-in-drop using axis symmetric drop shape analysis-profile (ADSA-P) technique has been extensively studied by Neumann and co-workers (Chen et al., 1998; Kwok, 1998; Lam et al., 2001, 2002). It has been concluded that in case of non-receding contact angle pattern, the contact angle hysteresis is only dictated by advancing contact angle. Therefore, the average advancing contact angle is used as the equilibrium contact angle for the surface energy calculations in conjunction with

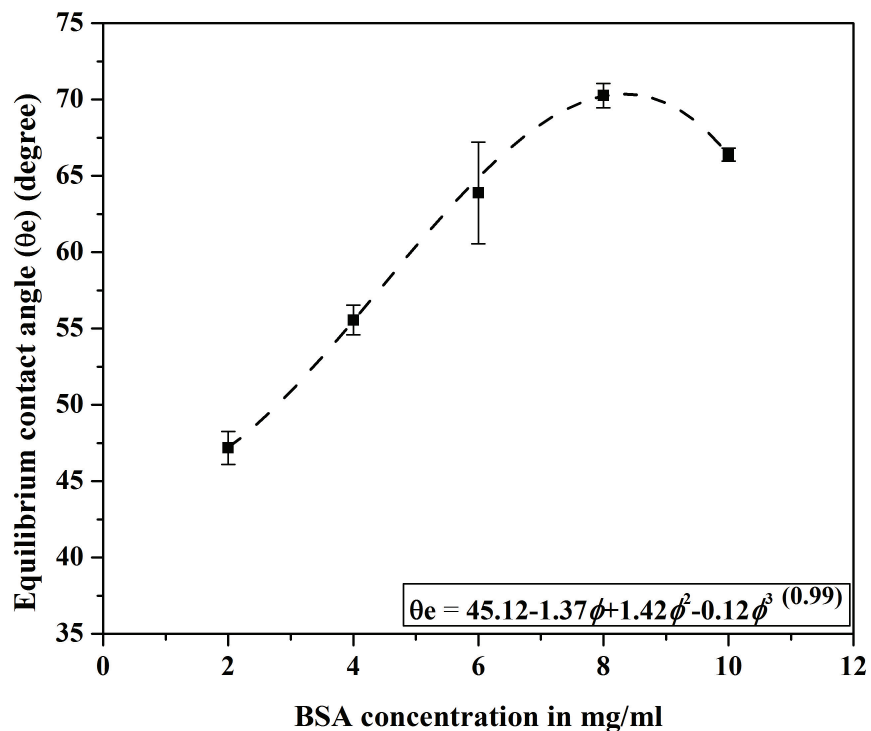


Figure 5.5: Variation in the equilibrium contact angle (θ_e) with the change in the BSA concentration (ϕ). Error bar reveals the range of maximum and minimum equilibrium contact angle for corresponding measurement series. Dotted line represents the corresponding curve fitted expression presented at the bottom right corner and the value in parentheses represents the corresponding coefficient of determination of the curve.

Young's equation (Kwok, 1998; Kwok and Neumann, 1998; Lam et al., 2001; Li and Neumann, 1992a,b). Hence, in this case the equilibrium contact angle is determined by averaging the advancing contact angle over the advancing domain. In the case of protein solution, it is speculated that the deposited molecules at the contact line do not respond to the bulk motion inside the drop during the receding of the drop.

Figure 5.5 represents the variation in the equilibrium contact angle of the BSA solution with the variation in the BSA concentration. The equilibrium contact angle is determined by averaging advancing contact angles over the five measurements using the same concentration. It is observed that the equilibrium contact angle magnitude is higher than the static contact angle, observed in Fig. 5.3. Moreover, the equilibrium contact angle also decreases as the BSA concentration decreases. The error bars with the dynamic contact angle measurements are much smaller as compared to the static contact angle measurements. Therefore, one can say that the wettability obtained with contact angle hysteresis is more realistic than the wettability obtained with the static contact angle measurements. In case of BSA solution, it has been observed from the surface tension measurements that the protein diffusion towards the interface increases as the BSA concentration increases. It is believed that the presence of the protein at the three-phase contact line might be the reason for non-receding contact angle pattern. It is also observed that the equilibrium contact angle increases as the BSA concentration increases. The protein concentration at the contact line also plays an important role during the advancing of contact angle. The increment in the concentration of bulk liquid also increases the protein concentration at the contact line. This contributes towards the resistance to the advancement of the contact line. Therefore, with the increment in the BSA concentration, the decrement in the advancing contact is observed, which, in turn, also decreases the equilibrium contact angle.

In microfluidic applications, based on the capillary flow, the liquid wetting properties, particularly the contact angle, play a vital role in predicting

the device performance. The passive pumping or autonomous pumping using capillarity has become a promising option in LOC and μ -TAS devices (Lim et al., 2007). In the laboratory conditions, to mimic the real blood sample, the transport of biomolecules is generally achieved with the BSA solution. Therefore, it is important to understand changes in the physical properties due to inclusion of the BSA in the working liquid. The viscosity and the density of BSA solution can be obtained with the available expressions from the literature (Hiemenz and Rajagopalan, 1997), but no such expressions for wetting properties, like surface tension and contact angle, are available. In the literature, the expressions for contact angle and surface tension for microbead suspensions are proposed on the basis of experimental observations (Waghmare and Mitra, 2010a). In a similar way such expressions for BSA solution can be proposed based on the experiments performed in this study. One of such expressions for equilibrium contact angle is provided at the right bottom corner of Fig. 5.5 where ϕ is the BSA concentration and the value in the parentheses represents the corresponding coefficient of determination of the curve. Such expressions which represent the variations in contact angle and the surface tension with the variation in the concentration can be further used in the modeling of passive pumping or autonomous flow transport processes (Waghmare and Mitra, 2010b).

5.4 Conclusion

The present chapter reports an experimental study of equilibrium contact angle and surface tension of BSA solution. The variations in the static contact angle and the surface tension are measured for BSA solutions of different concentrations. Further, the hysteresis in the contact angle is studied with the dynamic contact angle measurements. From the performed experimental study, it is observed that the surface tension of the BSA solution decreases nonlinearly as the concentration of the BSA in the solution increases. The variation in the static contact angle with the variation in the BSA concentration is not consistent, therefore dynamic contact angle measurements are performed. For the

considered combination of BSA solution and the substrate, non-receding contact angle pattern is observed. The equilibrium contact angle obtained from dynamic contact angle measurement decreases as the concentration of BSA increases. It is evident from these measurements that not only the surface tension but also the contact angle depends on the concentration of BSA in the solution. Finally, one can obtain an empirical correlation for the variations in contact angle and surface tension from these experimental results, which further can be used in the theoretical modeling of capillary flow in microfluidic devices for transporting different biomolecules of interest.

References

- Bormashenko E., General equation describing wetting of rough surfaces. *Journal of Colloid and Interface Science*, 360(1):317–319, 2011.
- Chau T. T., A review of techniques for measurement of contact angles and their applicability on mineral surfaces. *Minerals Engineering*, 22(3):213–219, 2009.
- Chen P., Prokop R. M., Susnar S. S., and Numann A. W., *in: Proteins at Liquid Interfaces, D. Möbius and R. Miller(Ed.)*, volume 7. Elsevier, 1998.
- de Gennes P. -G. , Brochard-Wyart F., and Qüéré D., *Capillarity and Wetting Phenomena: Drops, Bubbles, Pearls, Waves*. Springer, Berlin, 2003.
- Extrand C. W., Hysteresis in contact angle measurements. *Encyclopedia of Surface and Colloid Science*, 1(1):2876 –2891, 2006.
- Girault H. H. J., Schiffrin D. J., and Smith B. D. V., The measurement of interfacial tension of pendant drops using a video image profile digitizer. *Journal of Colloid And Interface Science*, 101(1):257–266, 1984.
- Gu Y. P., Contact angle measurement techniques for determination of wettability. *Encyclopedia of Surface and Colloid Science*, 1(1):1525–1539, 2006.
- DSA 100 drop shape analysis, software manual, Krüss GmbH Hamaburg*. Hamaburg, 2004.
- Hayes R. A., Robinson A. C., and Ralston J. A., A wilhelmy technique for

- the rapid assessment of solid wetting dynamics. *Langmuir*, 10(8):2850–2852, 1994.
- Hiemenz P. C. and Rajagopalan R., *Principles of Colloid and Surface Chemistry*. CRC Press,, 1997.
- Israelachvili J. N., *Intermolecular and surface forces*. Academic Press, 1998.
- Juncker D., Schmid H., Drechsler U., Wolf H., Wolf M., Michel B., de Rooij N., and Delamarche E., Autonomous microfluidic capillary system. *Analytical Chemistry*, 74(24):6139–6144, 2002.
- Kwok D. Y., *Contact angles and surface energetics*. PhD thesis, University of Toronto, 1998.
- Kwok D. Y. and Neumann A. W., Contact angles and surface energetics. In Lagaly, G , editor, *Horizon 2000- Aspects of Colloid and Interface Science at the Turn of the Millenium*, volume 109 of *Progress in COLloid and Polyemer Science*, pages 170–184, 1998.
- Lam C. N. C. , Kim N., Hui D., Kwok D. Y. , Hair M. L., and Neumann A. W., The effect of liquid properties to contact angle hysteresis. *Colloids and Surfaces A: Physicochemical and Engineering Aspects*, 189(1-3):265–278, 2001.
- Lam C. N. C., Ko R. H. Y., Yu L. M. Y. , Ng A., Li D., Hair M. L. , and Neumann A. W., Dynamic cycling contact angle measurements: Study of advancing and receding contact angles. *Journal of Colloid And Interface Science*, 243(1):208–218, 2001.
- Lam C. N. C., Wu R., Li D., Hair M. L., and Neumann A. W., Study of the advancing and receding contact angles: Liquid sorption as a cause of contact angle hysteresis. *Advances in Colloid and Interface Science*, 96(1-3):169–191, 2002.

- Li D. and Neumann A. W., Contact angles on hydrophobic solid-surfaces and their interpretation. *Journal of Colloid And Interface Science*, 148(1): 190–200, 1992a.
- Li D. and Neumann A. W., Equation of state for interfacial-tension bands of solid-liquid system. *Advances in Colloid and Interface Science*, 39(C): 299–345, 1992b.
- Lim C. T., and Zhang Y., Bead-based microfluidic immunoassays: The next generation. *Biosensors and Bioelectronics*, 22(7):1197–1204, 2007.
- Macdougall G. and Ockrent C., Surface energy relations in liquid/solid systems- i. the adhesion of liquids to solids and a new method of determining the surface tension of liquids. *Proceedings of Royal Society A*, 180 (981):151–173, 1942.
- Marmur A., *Contact Angle, Wettability and Adhesion, Volume 6*, volume 6, chapter A Guide To The Equilibrium Contact Angles Maze, Kash Mittal, pages 3–18. Hotei, Leiden, The Netherlands, 2009.
- Nguyen N. and Wereley S., *Fundamentals and Applications of Microfluidics*. Artech House, New York, 2003.
- Peters T., *All About Albumin*. Elsevier Inc., 1995.
- Saha A. A. and Mitra S. K., Effect of dynamic contact angle in a volume of fluid (VOF) model for a microfluidic capillary flow. *Journal of Colloid and Interface Science*, 339(2):461–480, 2009.
- Saha A. A., Mitra S. K., Tweedie M., Roy S., and McLaughlin J., Experimental and numerical investigation of capillary flow in su8 and pdms microchannels with integrated pillars. *Microfluidics and Nanofluidics*, 7(4):451–465, 2009.
- Stone H. A., Stroock A. D., and Ajdari A., Engineering flows in small devices: Microfluidics toward a lab-on-a-chip. *Annual Review of Fluid Mechanics*, 36:381–411, 2004.

- Tadmor R., Line energy and the relation between advancing, receding, and young contact angles. *Langmuir*, 20(18):7659–7664, 2004.
- Waghmare P. R. and Mitra S. K., Contact angle hysteresis of microbead suspensions. *Langmuir*, 26(22):17082–17089, 2010a.
- Waghmare P. R. and Mitra S. K., Finite reservoir effect on capillary flow of microbead suspension in rectangular microchannels. *Journal of Colloid and Interface Science*, 351(2):561–569, 2010b.
- Waghmare P. R. and Mitra S. K., Modeling of combined electroosmotic and capillary flow in microchannels. *Analytica Chimica Acta*, 663(2):117–126, 2010c.
- Waghmare P. R. and Mitra S. K., A comprehensive theoretical model of capillary transport in rectangular microchannels. *Microfluidics and Nanofluidics*, 12(1-4):53–63, 2012.
- Walker G. M. and Beebe D. J., A passive pumping method for microfluidic devices. *Lab on a Chip - Miniaturisation for Chemistry and Biology*, 2(3):131–134, 2002.
- Wong T. S., Chen T. H., Shen X., and Ho C. M., Nanochromatography driven by the coffee ring effect. *Analytical Chemistry*, 83(6):1871–1873, 2011.
- Young T., An essay of the cohesion of fluids. *Philosophical Transaction of the Royal Society of London*, 95:65–87, 1805.
- Zimmermann M., Schmid H., Hunziker P., and Delamarche E., Capillary pumps for autonomous capillary systems. *Lab on a Chip - Miniaturisation for Chemistry and Biology*, 7(1):119–125, 2007.

Chapter 6

Finite Reservoir Effect on Capillary Flow of Microbead Suspension in Rectangular Microchannels¹

6.1 Introduction

Lab-on-a-Chip (LOC) devices are increasingly become popular as a point-of-care system (Geschke et al., 2004). In a typical LOC, the analytes containing biomolecules flow through the complex microchannel network, performing different functions. The transport of such analytes is a major concern while predicting the optimum functionality of the device. In microscale devices, the surface to volume ratio is very high which results in surface forces being dominant over body forces (Karniadakis et al., 2005; Nguyen and Wereley, 2003). Higher surface forces require a large pressure drop for conventional fluid transport especially with pressure driven flows. Hence, researchers have focused on different mechanisms for transport of the fluid with non-mechanical approach or with combination of mechanical and non-mechanical pumping mechanisms. Attempts are being made to establish flow in microchannels without external means, where the flow rate is achieved by controlling the microchannel geometries, surface chemistry, and fluid surface tension (Walker and Beebe, 2002).

¹A version of this chapter has been published. Waghmare and Mitra, 2010, Journal of Colloid and Interface Science, 351 (2), 561-569

Capillarity is one such approach, which is widely termed as passive pumping in microfluidic devices. It has been successfully attempted in LOC (Juncker et al., 2002; Zimmermann et al., 2007).

Theoretical understanding of capillarity has been conducted over the past century. From Washburn (Washburn, 1921) to till date (Waghmare and Mitra, 2010c), the flow transport due to capillarity with infinite reservoir at the microchannel inlet is investigated. In theoretical investigations, the dominance of several forces such as viscous, surface tension and gravity forces is considered for modeling. Washburn (Washburn, 1921) performed experiments in round capillaries of few millimeters to validate the closed form solution for the time required to attain the steady state capillary rise generally termed as equilibrium penetration depth. Further, similar model for polymer transport considering the dynamic contact angle along the slit of vertical plates is proposed by Newman (Newman, 1968). Rather than using quasi-steady state approximation of Washburn (Washburn, 1921) and Newman (Newman, 1968), Szekeley et al. (Szekely et al., 1971) used a microscopic energy balance to a control volume of liquid rising in a channel. The kinetic energy, potential energy, work done against surroundings and frictional force are calculated and rearranged, which results into a second order differential equation. Szekeley et al. (Szekely et al., 1971) claimed that the Washburn approach (Washburn, 1921) is not applicable for short capillary transport and thus proposed a characteristic time which dictates the applicability of the Washburn equation. Levine et al. (Levine et al., 1976) proposed the expression for an additional suction force at the inlet of a circular capillary with the quasi-steady state approximation. Similar nature of the governing equation, as proposed by Szekeley et al. (Szekely et al., 1971), is obtained by Levin et al. (Levine et al., 1976) with an integral momentum approach. Pressure field proposed by Levine et al. (Levine et al., 1976) has been further used for rectangular capillaries with an equivalent radius assumption (Dreyer et al., 1993). This equivalent radius assumption may not be appropriate for realistic situation of capillary flow in noncircular geometries. In particular, for high as-

pect ratio channels one needs to consider modified pressure field as proposed by Waghmare and Mitra (Waghmare and Mitra, 2010). Development of such theoretical approaches for predicting the capillary transport can be seen elsewhere (Xiao et al., 2006). In recent years, analytical solutions for parallel plate and circular capillary are presented by Xiao et al. (Xiao et al., 2006). Finite volume approach for capillary transport has also been reported by Saha and Mitra (Saha and Mitra, 2009a) where they have meticulously demonstrated the applicability of different dynamic contact models at the beginning of the microchannel filling process.

For many years, researchers have tried to validate the Washburn's (Washburn, 1921) close form solution for different operating conditions (Jeje, 1979; Stange et al., 2003). Jeje (Jeje, 1979) performed a series of experiments with microscale circular tubes ($266\mu m$ and $1191\mu m$ in diameter). It is demonstrated that at the beginning of the filling process of the capillaries, the theoretical predictions with Poiseuille flow approximation deviates from experimental observations. Such departure from the quasi-steady state approximation i.e., Poiseuille flow for predicting the capillary transport is also summarized by Levine et al. (Levine et al., 1980). The rate of capillary penetration for a slit capillary is studied by Dreyer et al. (Dreyer et al., 1994, 1993). In their study also an assumption of infinite reservoir is made to develop similar pressure field as proposed by the Levine (Levine et al., 1976). It is to be noted that for most of these studies, the capillary flow is assumed to take place from an infinite reservoir. The reservoir effect at the inlet of the microchannel has been simply ignored by assuming infinite reservoir. In case of LOC, where the fluid flows from the inlet reservoir into the microchannel by capillarity to the detection site, the presence of such finite reservoir size can not be neglected. Hence, in case of capillary transport analysis for LOC applications, reservoir with infinite size may not be a valid assumption.

Although it has been reported with the scaling law that the gravity forces are less dominant as compared to surface forces (Nguyen and Werely, 2003), attempts are being made to take an advantage of gravity with capillarity in

microscales. To enhance and control the transport, LOC chip may be oriented vertically to take the advantage of gravity. Jong et al. (Jong et al., 2007) theoretically developed a model for investigating the effect of gravity on capillary transport for a L-shaped reservoir-capillary configuration. An additional gravity head is achieved by placing the capillary in the same horizontal plane as the reservoir exit. Such reservoirs are not un-common in a LOC, where the analytes and biomolecules are typically stored in a fluid reservoir at the inlet of the microchannels. Variation in the reservoir fluid height i.e., gravitational head on the capillary transport is investigated experimentally and the results are compared with closed form theoretical solutions. Their theoretical analysis assumed a constant static head and it matched with the experiments. The effect of gravity with capillarity on the blood transport in microdevice is experimentally presented by Yamada et al. (Yamada et al., 2008). In this study, device consists of intersecting channels- a straight one and two inclined microchannels. It is reported that the channel with more inclination gives higher velocity beyond the point of two intersecting channels. Kung et al. (Kung et al., 2009) have demonstrated experimentally that the velocity of blood flow due to capillary transport in a microchannel increases with the increase in the inclination angle of the microchannel. These studies strongly suggest that, one can couple the gravity with capillarity in microfluidic device to enhance the non-mechanical pumping capability of microfluidic devices. Hence, in the present study the gravitational head with the reservoir effects is modeled and analyzed in detail.

The working fluid considered in the analyses discussed so far is a single phase fluid, but it is quite common for microfluidic applications to have microbeads and other suspended molecules in its carrier fluid (Kawaguchi, 2000). Hence in the present study the working fluid is considered as a microbead suspension. Kawaguchi (Kawaguchi, 2000) has provided an overview for the potential use of microbeads in biomedical applications. Presence of microbeads in the working fluid accommodates more biomolecule due to increase in the surface area. This increment in the surface to volume ratio increases the sensi-

tivity of the device (Verpoorte, 2003). The capability of multiple functionalities of microbeads allows the development of LOC for various applications like detection, separation and identification of different biomolecules (Yun et al., 2009). Review on the development of the microbead based assay in microfluidic devices can be found elsewhere (Lim et al., 2007). In such devices, the majority of the fluid transportation is achieved by either conventional pressure driven flow or by electrokinetic approaches, but rarely using capillarity.

Existing literature suggests that, the investigation of the fluid transport with non-mechanical pumping approach in the microbead based microfluidic devices is in evolving phase. It is observed that the presence of reservoir at the inlet of microfluidic channels and its effect on the capillary transport in the microchannels has not been analyzed in great details. Hence, a theoretical study for predicting capillary transport of a microbead suspension considering reservoir effects is necessary. In the present study, the pressure field distribution at the inlet of the vertical rectangular microchannel is proposed which accounts the reservoir effect and gravitational force from the reservoir. Inclusion of the microbead in the transporting fluid changes the fluid properties like viscosity, density, surface tension and the contact angle. Appropriate expressions for the equivalent physical properties are considered while deriving the governing equation. Further, a generalized non-dimensional governing equation is obtained considering equivalent physical properties of fluid. Finally, a parametric study is performed to investigate the effects of different operating conditions like, gravity head, channel dimensions, fluid properties, etc. on the capillary transport.

6.2 Mathematical modeling for gravity assisted capillary transport

The schematic of the microchannel geometry along with the fluid reservoir under investigation is presented in Fig. 6.1. A rectangular fluid reservoir for an additional gravitational head is considered at the top of the vertically oriented rectangular microchannel. Typically, the microchannel dimensions

in the microfluidic applications are in the range of $50\mu m$ to $200\mu m$ and the reservoir dimensions are in the range of $500\mu m$ to a few millimeters (Kung et al., 2009). The configuration presented in Fig. 6.1 is a fair representation of reservoir-microchannel arrangement in a typical LOC. The additional gravitational head from the reservoir fluid provides an assistance to the fluid, which penetrates through the microchannel due to surface tension i.e., capillarity. This gravitational head can be varied by changing either the volume of fluid or by changing the inclination of the device. Typical fluid volume in the reservoirs is $500 - 1000\mu l$ and within the microchannel it is $50 - 200\mu l$. Initially, the mathematical model for the capillary penetration is developed with equivalent fluid properties. It involves the development of the pressure field expression at the entrance of the rectangular microchannel which accounts for the reservoir effects. Further, appropriate correlations for the equivalent fluid properties are used in the formulation, which are based on previous experiments conducted by the authors and a non-dimensional governing equation is derived to perform the analysis.

The integral momentum equation is applied to a fluid volume which penetrates within the rectangular microchannel of width $2B_1$ and depth $2W_1$, as shown in Fig. 6.1., which can be written as,

$$\sum F_z = \frac{\partial}{\partial t} \int_0^h \int_{-W_1}^{W_1} \int_{-B_1}^{B_1} \rho_e v_z dx dy dz + \int_{-W_1}^{W_1} \int_{-B_1}^{B_1} v_z (-\rho_e v_z) dx dy \quad (6.1)$$

Here, h is the penetration depth or movement of the fluid flow front in the microchannel, ρ_e is the effective density of the suspension and v_z is the velocity of the flow front across the channel, the details of which are provided later. This momentum equation represents the transient movement of the liquid front meniscus along the z -axis, which is termed as penetration depth. The capillary front is measured from the inlet of the microchannel to the point of intersection of the meniscus front with z -axis. The reservoir effect is accounted through the pressure field at the inlet of the microchannel, which is elaborated in the later part of the study.

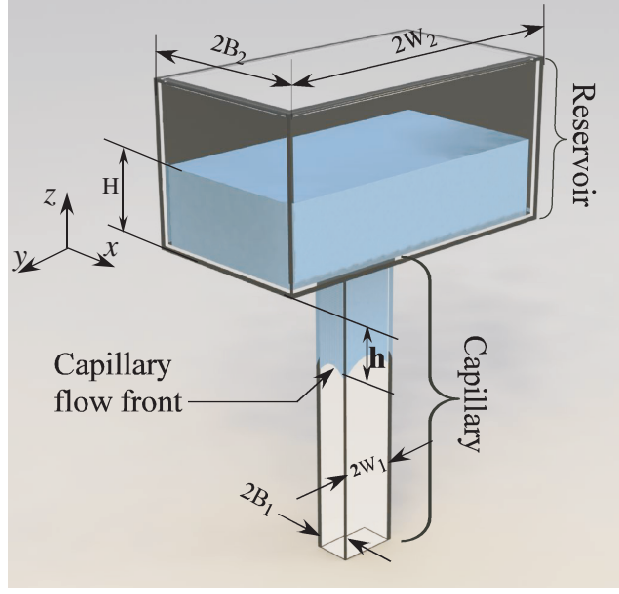


Figure 6.1: Schematic of gravity assisted capillary flow in a vertically oriented microchannels of width $2B_1$ and depth $2W_1$. The additional gravitational head from the fluid in finite reservoir of size $(2B_2 \times 2W_2)$ is assisting the capillary flow. The depth of microchannel is assumed very large as compared to the width of microchannel.

In Eq. 6.1, $\sum F_z$ is the summation of all forces acting on the fluid under consideration viz., viscous (F_v), gravity ($F_g = 4\rho_e g h B_1 W_1$), pressure forces at the flow front (F_{pf}) and at the inlet (F_{pi}), as illustrated here:

$$\sum F_z = F_v + F_g + F_{pf} + F_{pi} \quad (6.2)$$

The knowledge of the velocity field v_z across the channel is necessary for evaluating transient and convective terms of Eq. 6.1 and the viscous force term in Eq. 6.2. Washburn (Washburn, 1921) showed that, the length prior to establishing Poiseuille flow is negligible in microscale capillaries and therefore a fully developed velocity profile can be assumed for the entire microchannel. Also Newman (Newman, 1968) reported that, in capillary transport, the rate of change of momentum of the capillary fluid is negligible as compared to the wetting rate. Further, the width of microchannel is assumed to be very small as compared to the depth of the microchannel. These approximations result into a parabolic velocity profile for v_z in pure capillary flow, which can be written as,

$$v_z = \frac{3}{2} \frac{dh}{dt} \left[1 - \left(\frac{x}{B_1} \right)^2 \right] \quad (6.3)$$

where, the velocity profile is a function of rate of change of the penetration depth. In the recent study by Bhattacharya and Gurung (Bhattacharya and Gurung, 2010), they have showed that this approximation introduces an error of the same order as that of neglecting the inertial term in the Navier-Stokes equation. They have also shown systematically that such approximation may not necessarily hold true for large Reynolds number flows. In the proposed analysis, the flow is a surface tension driven and therefore it can be assumed as a creeping flow. Hence, the approximated velocity profile, provided in Eq. 6.3, holds true as the inertial term in Navier-Stokes equation is always neglected in such analysis. However, one can avoid this approximation by using the exact transient velocity profile (Batchelor, 2002; Waghmare and Mitra, 2010c). The change in the velocity profile at the entrance region and at the flow front are also neglected. It is demonstrated that, the error due to these approximations is negligible because the entrance region and depth of meniscus are very small (Newman, 1968). Theoretical investigations based on these corollaries have been widely accepted and validated with experimental results (Dreyer et al., 1994; Barraza et al., 2002; Dreyer et al., 1993; Mawardi et al., 2008). It is also assumed that the velocity profile, provided in Eq. 6.3, does not alter with the introduction of reservoir placed at the inlet of the microchannel.

6.2.1 Pressure field and force at the inlet of rectangular microchannel

In most of the capillary transport analysis, the entrance effect is added by considering a suction pressure at the inlet of the capillary (Dreyer et al., 1994, 1993; Levine et al., 1976; Mawardi et al., 2008). Szekely et al. (Szekely et al., 1971) used the energy balance to depict the pressure drop at the entrance. In their study, the rate of energy dissipation at the capillary entrance is deduced in terms of empirical constants. Levine et al. (Levine et al., 1976) deduced

the entrance effect in terms of pressure distribution field at the inlet of a circular capillary. The pressure field, as proposed by Levine et al. (Levine et al., 1976), is widely used for circular capillaries and has been further extended to non-circular capillaries by several other authors (Dreyer et al., 1994; Barraza et al., 2002; Dreyer et al., 1993; Mawardi et al., 2008). For non-circular capillaries, the capillary radius has been replaced with an equivalent radius which represents the non-circular geometry. This approach may not be a valid for higher aspect ratio channels (Waghmare and Mitra, 2010). The pressure field in such cases is derived with an assumption of an infinite reservoir i.e., the effect of reservoir is neglected. In the present analysis, the reservoir of a finite dimension is placed at the top of the microchannel, hence the pressure field expression from the literature can not be used in its available form. Therefore, the expression for the pressure field at the entrance of microchannel with reservoir effect is presented here.

If H represent the *initial* reservoir fluid level, then the rate of penetration within a microchannel is $\frac{dh}{dt}$ and rate of decrement in the height of the fluid in the reservoir is $\frac{dH}{dt}$, which can be correlated through the continuity equation,

$$\frac{dH}{dt} = \alpha \frac{dh}{dt} \quad (6.4)$$

where, α is the ratio of microchannel area A_1 to reservoir area A_2 . The momentum equation for the suspension of effective viscosity μ_e in the reservoir in terms of rate of increment in the penetration depth can be written as,

$$\rho_e \alpha \frac{d^2 h}{dt^2} = -\frac{dp}{dz} + \mu_e \frac{32\alpha(\gamma_2^2 + 1)}{B_2^2} \frac{dh}{dt} + \rho_e g \quad (6.5)$$

Here, γ_1 and γ_2 denote the aspect ratios (ratio of width to depth) for the microchannel and the reservoir, respectively and g denotes the acceleration due to gravity. The second term at the right hand side of Eq. 6.5 represents the resistance offered by the reservoir to the fluid in flow within the capillary. The pressure at the inlet of the microchannel, i.e., p can be deduced assuming an atmospheric pressure p_0 at the free surface of the reservoir fluid at height H . The height of the fluid in the reservoir changes with the penetration depth

in the microchannel. The expression for the pressure field at the inlet of the microchannel in terms of rate of increment in the penetration depth can be deduced by integrating Eq. 6.5 with respect to reservoir height,

$$p(x, y, t) = p_0 - \rho_e \alpha \frac{d^2 h}{dt^2} (H - \alpha h) + \frac{32\alpha (\gamma_2^2 + 1)}{B_2^2} \mu_e (H - \alpha h) \frac{dh}{dt} + \rho_e g (H - \alpha h) \quad (6.6)$$

Thus, the force at the inlet of the microchannel can be calculated as,

$$F_{pi} = \int_{-W_1}^{W_1} \int_{-B_1}^{B_1} p(x, y, t) dx dy \quad (6.7)$$

The gravitational force due to fluid transport in the microchannel is,

$$F_g = \int_0^h \int_{-W_1}^{W_1} \int_{-B_1}^{B_1} \rho g dx dy dz \quad (6.8)$$

The capillary action can be determined by the capillary pressure which can be used subsequently to determine the pressure force at the flow front. Generally, the capillary pressure is given by Young-Laplace equation and the force at the flow front can be written as,

$$F_{pf} = \int_{-B_1}^{B_1} \int_{-W_1}^{W_1} \sigma_e \left(\frac{\cos \theta_e}{B_1} - \frac{1}{W_1} \right) dx dy \quad (6.9)$$

where, σ_e and θ_e are the effective surface tension and equilibrium contact angles of the suspension, respectively. Several attempts are being made to present a generalized model which can encapsulate relevant physics for the change in the contact angles of working fluid without microbeads (Barraza et al., 2002; Newman, 1968; Xiao et al., 2006). In case of contact angle, the time dependent contact angle expression is often used which contains tunable parameter that depends on experimental inputs. Recently, Saha and Mitra (Saha and Mitra, 2009a) reported different dynamic contact angle models and their applicability in the microfluidic applications. It has been observed that, no generalized model for dynamic contact angle can be used for capillary driven flows in microfluidic applications. Hence, effective static equilibrium contact angle is considered in the present analysis which will be a function of

microbead concentrations only. Detailed explanation on the effective physical properties of the microbead suspension is elaborated in the next section.

The viscous force in the microchannel can be calculated as,

$$F_v = \int_0^h \int_{-W_1}^{W_1} \mu_e \left(\frac{dv_z}{dx} \right)_{x=\pm B_1} dydz \quad (6.10)$$

The velocity profile given by Eq. 6.3 is used to evaluate the viscous force. The same velocity profile is used to determine transient and convective terms of the momentum equation. Finally, rearranging the forces, the convective and the transient terms of the integral momentum equation, the dimensional momentum equation can be written as,

$$\begin{aligned} & \left[h + \frac{\alpha H}{(1 - \alpha^2)} \right] \frac{d^2 h}{dt^2} - \frac{0.2}{(1 - \alpha^2)} \left(\frac{dh}{dt} \right)^2 \\ & + \frac{3\mu_e}{\rho_e B_1^2 (1 - \alpha^2)} \left\{ [\lambda + 1] h - \frac{\lambda}{\alpha} H \right\} \frac{dh}{dt} \\ & - \frac{g(1 - \alpha)}{(1 - \alpha^2)} h - \frac{gH}{(1 - \alpha^2)} - \frac{\sigma_e}{\rho(1 - \alpha^2)} \left(\frac{\cos \theta_e}{B_1} - \frac{1}{W_1} \right) = 0 \end{aligned} \quad (6.11)$$

where, $\lambda = \frac{32}{3} \gamma_B^2 \alpha^2 (\gamma_2^2 + 1)$ and γ_B is the ratio of the microchannel to the reservoir width. The detailed explanation on the development of Eq. 6.11 is reported in the Appendix A-1. Equation 6.11 governs the gravity assisted capillary transport in a microchannel. Physical properties in the governing equation are effective properties since the inclusion of microbead in the working fluid changes its rheological behavior. The detailed explanation on the selection of the expression for equivalent physical properties is provided in next section.

6.2.2 Physical properties of suspension

In this analysis the properties of the suspension is denoted with subscript ‘e’ whereas the fluid in which the particles are suspended is denoted with subscript ‘f’. Inclusion of microbeads in a carrier fluid changes the effective physical and surface properties of the fluid like viscosity, density and surface tension. In this section the expressions for these properties are proposed which dictate

the effect of microbead in the fluid according to its concentrations. Following assumptions are made in this analysis for microbead suspension:

1. Spherical particles are uncharged, large and rigid enough to assume that Brownian motion will not change the velocity distribution of fluid. Therefore Brownian motion is neglected in the present analysis.
2. Spherical particle has velocity in the direction of flow only i.e., towards gravity.
3. The variation of particle concentration across the channel is neglected.
4. Effect of particle-particle and particle-wall surface interaction is neglected.

It is also assumed that, microchannel inner wall and particle surfaces will not acquire any surface charges during the transport process of the suspension. Hence, the electrokinetic or electrostatic effects such as an electroviscous effect are neglected in the present analysis.

Density and Viscosity

Einstein in his pioneer work reported an expression for the viscosity of a dilute dispersion of solid spheres. It has been assumed that, these spherical particles may or may not rotate in response to the fluid flow. In case of rotating particles, the additional energy is required to rotate particles whereas, non-rotating particle reduces the velocity gradient. The additional energy for the rotation of the particles and due to decrement in the velocity gradient can be compensated by the change in the viscosity. Generally, the concentrations of the microparticles is represented as volume fraction (ϕ), which is the ratio of the particle to suspension volume. The effective viscosity of a suspension with microbead of volume fraction ϕ can be written as (Hiemenz and Rajagopalan, 1997),

$$\frac{\mu_e}{\mu_f} = 1 + 2.5\phi \quad (6.12)$$

which is widely known as Einstein's first order equation of viscosity of suspension. There are certain restrictions for Einstein's equation like, particles must

be solid spheres and the concentration must be small up to 10% (Hiemenz and Rajagopalan, 1997). The applicability of the equation can be extended by providing an exponent to the bead volume fraction, ϕ in Eq. 6.12 but the constant factor for the exponents generally varies with the application. The presence of microbeads also changes the mass of the fluid per unit volume which in turn changes the effective density of the suspension. The effective density of the suspension with particles of density ρ_p can be represented as (Peker and Helveci, 2008),

$$\rho_e = \phi\rho_p + (1 - \phi)\rho_f \quad (6.13)$$

which is a strong function of the volume fraction of the microbeads present in the fluid.

Surface tension and contact angle

Surface tension and contact angles are manifestations of the intermolecular interactions of three phases at the liquid-wall-air interface. It has been reported that, the presence of solid particles in the fluid also changes the surface tension (Blute et al., 2009; Brian and Chen, 1987; Kihm and Deignan, 1995; Wang et al., 2004). Literature suggests that, there is no generalized theory for predicting the surface tension and the contact angle of microbead suspension based on its concentration. Hence, authors have performed experiments to determine these expressions which can be readily used for theoretical analysis. Suspensions with different volume fraction of polystyrene microbeads are prepared to determine the surface tension and the equilibrium contact angle. Equilibrium contact angle is determined by dynamic contact angle measurements i.e., by measuring advancing and receding contact angles. The pendent drop technique is used to determine the surface tension whereas, dynamic contact angles are measured with the sessile drop technique. Average surface tension and equilibrium contact angle for the corresponding sample with fixed volume fraction are determined by averaging the five measurements which are performed on the each sample. Finally, empirical correlations for variations in the surface tension and contact angle are obtained by appropriate curve fitting

to the measured values as depicted in Table 6.1. Such expressions can readily be used in the present analysis. Further details on the experimental set-up and the empirical correlations that are used in the present study can be found elsewhere (Waghmare and Mitra, 2010a). The coefficients of determination for the contact angle correlations are 0.9923 and 0.9642 for suspension A and B, respectively. In case of surface tension correlations for suspension A and B the coefficients of determination are 0.9879 and 0.9863, respectively. The correlation for suspension A is used in further analysis.

Table 6.1: Empirical correlations for contact angle and surface tension using curve fitting to the measurement values over the range of the volume fraction expressed in percentage (Waghmare and Mitra, 2010a)

Range of volume fraction(ϕ) of microbeads	Expression	
	σ	θ
0 – 10 (<i>Suspension A</i>)	$44.89 \exp\left(\frac{-\phi}{2.95}\right) + 27.41$	$0.152\phi^3 - 2.74\phi^2 + 11.13\phi + 52.31$
0 – 5 (<i>Suspension B</i>)	$-0.005 \exp\left(\frac{\phi}{0.611}\right) + 70.71$	$1.24\phi^3 - 10.63\phi^2 + 16.29\phi + 69.75$

Expressions for effective physical properties of the suspensions are replaced in the dimensional governing equation and further non-dimensional analysis is performed to obtain the generalized non-dimensional equation. A non-dimensional time (t^*) and the penetration depth(h^*) are defined with respect to the characteristic time, $t_0 = \frac{\rho_f (2B_1)^2}{12\mu_f}$ and the characteristic length $h_0 = 2B_1$, respectively. Hence, a generalized non-dimensional governing equation for gravity assisted capillary transport in a microchannel with reservoir effects can be written as,

$$(h^* + C_1) \frac{d^2 h^*}{dt^{*2}} + C_2 \left(\frac{dh^*}{dt^*} \right)^2 + (C_3 h^* + C_4) \frac{dh^*}{dt^*} + C_5 h^* + C_6 = 0 \quad (6.14)$$

The coefficients of the non-dimensional governing equation are tabulated in Table 6.2. Several non-dimensional numbers are obtained like Bond number(Bo) and Ohnesorge number(Oh) which represent the importance of gravity and viscous force relative to the surface tension force. The Ohnesorge

number $\left(Oh = \frac{\mu}{\sqrt{2B_1\rho_f\sigma_f}} \right)$ is the ratio of viscous to surface tension force and the Bond number $\left(Bo = \frac{\rho_f g (2B_1^2)}{\sigma_f} \right)$ is the ratio of gravity to surface tension force. Some of the non-dimensional parameters like γ_1 , γ_2 , γ_B and $H^*(= H/2B_1)$ represent characteristic groups of geometrical dimensions. In the analysis, area aspect ratio α is represented in terms of width and depth aspect ratios. Effective physical properties are normalized with the fluid properties and represented with superscript ‘*’. The fourth order Runge-Kutta method is used to obtain the solution of Eq. 6.14 with zero capillary velocity as the initial condition.

Table 6.2: Constants of the generalized non-dimensional governing equation for a gravity assisted capillary flow of microbead suspension in a microchannel

Constants	Expressions
C_1	$\frac{\alpha H^*}{(1-\alpha^2)}$
C_2	$\frac{-0.2}{(1-\alpha^2)}$
C_3	$-\frac{\mu^*}{\rho^*} \frac{1+\lambda}{(1-\alpha^2)}$
C_4	$-\frac{\mu^*}{\rho^*} \frac{\lambda}{\alpha(1-\alpha^2)} H^*$
C_5	$-\frac{Bo}{144Oh^2} \frac{(1-\alpha)}{(1-\alpha^2)}$
C_6	$\frac{\sigma^*(\gamma_1 - \cos\theta_e)}{72\rho^*Oh^2(1-\alpha^2)} - \frac{BoH^*}{144(1-\alpha^2)Oh^2}$

6.3 Results and discussion

The variation in the penetration depth, i.e., h^* with different operating conditions is presented in this section. Such variation can be achieved by varying the reservoir fluid level. This variation depicts the interplay between the surface tension force from the microchannel and gravity force offered by the reservoir. The variation in the flow front transport by changing the reservoir fluid level for a given volume fraction of microbead suspension is observed in Fig. 6.2. Three different reservoir heights (H^*) have been selected for this parametric study viz., 10.0, 50.0 and 100.0. Microbead suspension transport with these different fluid levels in the reservoir has same capillarity effects at

the entrance of the microchannel. At the beginning of the flow front transport, the inertia force dominates the gravitational head of the reservoir. Hence for $H^* = 100$, initially the flow front penetrates with lower rate as compared to other two reservoir heights (10 and 50).

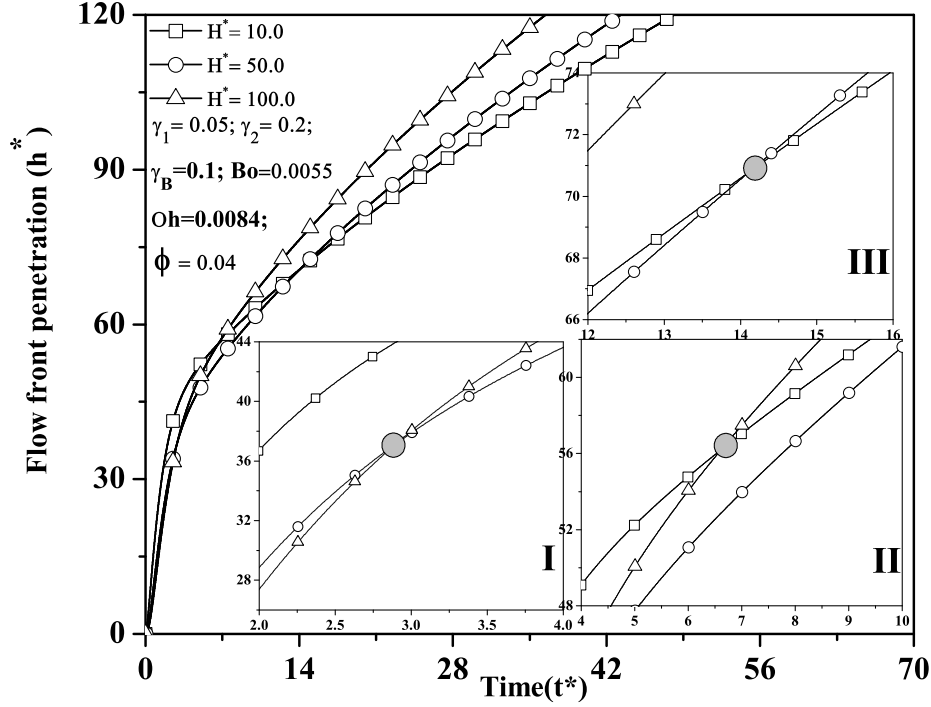


Figure 6.2: Transient response of a flow front transport for different gravitational heads in the reservoir with $Bo=0.0055$, $Oh=0.0084$, $\gamma_1=0.05$, $\gamma_2 = 0.2$, $\gamma_B = 0.1$ and $\phi = 0.04$. **I** : Flow front penetration rate for $H^* = 100$ surpasses the penetration rate for $H^* = 50$. **II** : Flow front penetration rate for $H^* = 100$ surpasses the penetration rate for $H^* = 10$. **III** : Flow front penetration rate for $H^* = 50$ surpasses the penetration rate for $H^* = 10$.

In case of $H^* = 10$, at the beginning of the flow front transport, the capillarity is dominant over gravitational head since less inertia is offered from the reservoir. However, for $H^* = 100$, at the beginning of the flow front transport the inertial forces suppress the capillarity and hence reduces the rate of penetration depth. In the later part of the microbead transport, the rate of

capillary penetration increase with H^* due to the increase in the momentum of the reservoir fluid. Three different transcendences are observed for three different H^* , which are presented in three different insets in Fig. 6.2. The rate of penetration depth with $H^* = 100$ surpasses the rate of penetration with $H^* = 50$ and $H^* = 10$ in insets *I* and *II*, respectively. Such observed crossing of the profiles are due to the interplay between capillary and gravity dominating regions. Similarly, such observation is presented in inset *III* for $H^* = 50$ and 10. Thus, the finite reservoir and gravitational force have significant impact on the capillary flow. The present formulation can be extended to the case where the reservoir has completely drained out with time. Under such condition, pressure at the entrance of the microchannel will approach towards the atmospheric pressure and the total gravity head on the flow front will be from the liquid inside the microchannel. One can use the gravitational head as an additional non-mechanical pumping tool to transport the carrier fluid within the LOC devices. In the subsequent study, for a fixed gravitational reservoir head the capillary penetration is studied by varying different non-dimensional parameters.

The interplay between gravitational head and capillarity in the microchannel can also be studied with the variations in the geometrical dimensions of the microchannel and the reservoir. Figure 6.3 shows the variation in the penetration depth with the change in the width aspect ratio γ_B . Aspect ratio is the ratio of the microchannel to the reservoir width and it is varied from 0.001 to 0.01. It is observed that, lower γ_B assists the transport i.e., flow front for small γ_B penetrates at higher rate as compared to large γ_B . Lower γ_B represents the lower B_1 or higher B_2 , which denotes the smaller microchannel width for a larger reservoir width.

Figure 6.3 suggests that at the beginning of the capillary transport, the surface force dominates the gravity and hence a sudden jump in the penetration depth at the initial time instants is observed as opposed to a linear variation in the penetration depth with time. For lower γ_B , in spite of higher gravitational force due to larger reservoir width, capillarity dominates over the gravity and

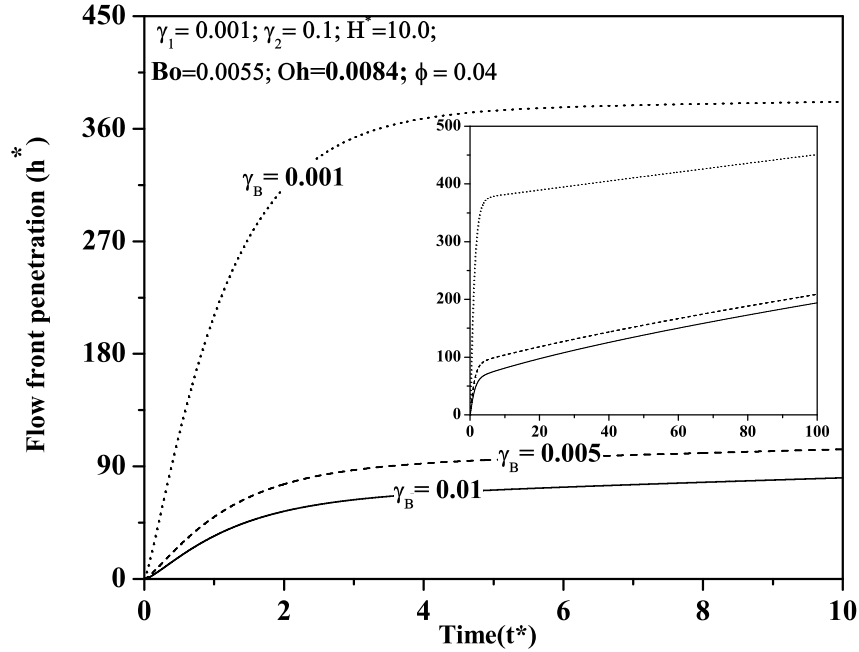


Figure 6.3: Transient response of a flow front transport for different ratios of microchannel to reservoir width with $Bo=0.0055$, $Oh=0.0084$, $\gamma_1=0.001$, $\gamma_2 = 0.1$, $H^* = 10.0$ and $\phi = 0.04$. Inset shows the linear increment in the penetration depth under gravity dominating region.

hence with the lower γ_B the flow front penetrates with a higher rate. The initial portion of the transport can be termed as the capillary dominating region. In this region there is a sudden jump in the penetration depth of the capillary front, which is due to capillarity. Afterwards the gravitational head at the rectangular microchannel entrance dominates the surface forces and the flow is due to gravity only i.e., free fall condition is observed. It is found in Fig 6.3 that the penetration depth attains the equilibrium penetration for shorter time instances i.e., within the capillary dominating region. The microbead suspension flow is allowed to occur beyond the initial capillary dominating region as depicted in the inset of Fig. 6.3 and the linear increment in the penetration depth is observed. Beginning of the linear increment of the penetration depth in the gravity dominating region represents the transition

from capillary dominant region to gravity dominant region. The gravitational head at the microchannel inlet does not allow the flow front to attain the equilibrium penetration depth which is commonly observed in the capillary flow analysis without gravity head (Xiao et al., 2006). Further increment in the reservoir height i.e., with $H^* = 500.0$ is presented in the Fig. 6.4 and it is observed that even for smaller time instances the gravitational force dominates the capillary action and hence for initial portion of the transport, the linear increment is observed. However, under such high H^* condition, differences in the penetration depth for different aspect ratio are smaller as compared to the previous case as shown in Fig. 6.3.

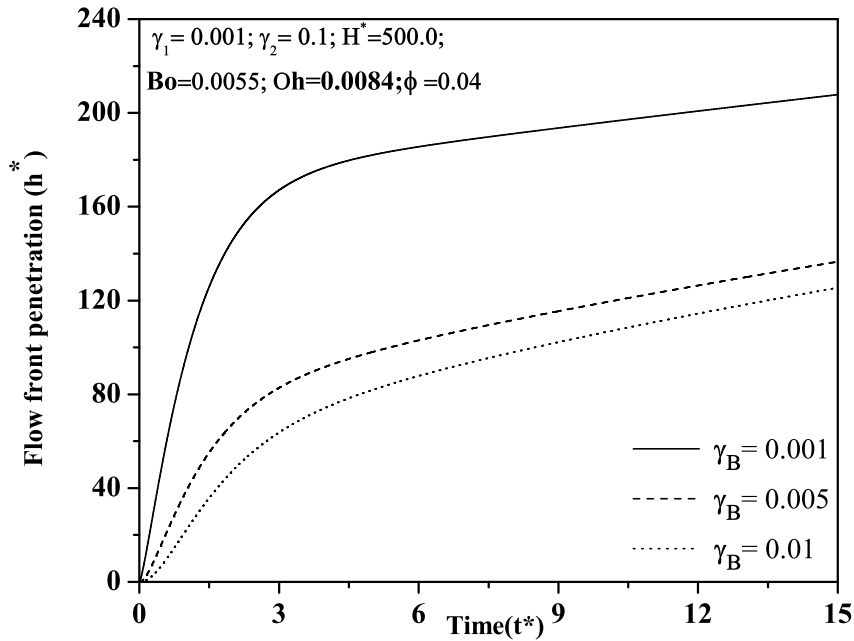


Figure 6.4: Transient response of a flow front transport for different ratios of microchannel to reservoir width with $Bo=0.0055$, $Oh=0.0084$, $\gamma_1=0.001$, $\gamma_2 = 0.1$, $H^* = 500.0$ and $\phi = 0.04$

Individual geometrical parameters of the microchannel and reservoir can also affect the transport of the flow front. This can be studied by varying the aspect ratios of the microchannel and the reservoir separately. The effect

of aspect ratio of the channel for capillary transport has been reported in the literature (Dreyer et al., 1994, 1993; Xiao et al., 2006). Earlier due to limitations in the microfabrication, often the parallel plate arrangement was used with a very small gap instead of a rectangular cross-section. Figure 6.5 shows the variation in the penetration depth with different aspect ratios of the microchannels which are comparable to the parallel plate arrangements reported in the literature. It is observed that, microchannel with higher aspect ratio assists the capillary transport. Aspect ratio of the microchannel γ_1 , is the ratio of the microchannel width to the microchannel depth for constant γ_B . Variation in the γ_1 for constant γ_B represents the variation in the depth of the microchannel. Increment in the γ_1 results in the decrement in the depth of the microchannel. This decrement in the overall area of the microchannel assist capillary flow and hence as the aspect ratio of the microchannel increases, the increment in the penetration depth is observed.

As the aspect ratio of the microchannels plays a vital role in the flow front penetrations, it is important to investigate the effect of reservoir aspect ratio on the variation in the penetration depth. Figure 6.6 shows the variations in the flow front progression with different aspect ratios of the reservoir which is varied from 0.01 to 0.1. Aspect ratio of the reservoir defines the gravitational head on the fluid present in the microchannel. It is to be noted that the aspect ratios of the reservoir are varied keeping the reservoir fluid level (H^*) and width aspect ratio (γ_B) constant. Two hypothesis can be presented for the observed behavior of the capillary front in Fig. 6.6. Firstly, the increment in the reservoir aspect ratio with constant H^* and γ_B results in the decrement in the depth of the reservoir. This provides smaller reservoir area which results in smaller gravitational head for the same capillarity action in the microchannel. The decrement in the gravitational head reduces the magnitude of penetration depth at same time instant for different γ_2 as demonstrated in Fig. 6.6. Secondly, this may be due to the fact that the reservoir with higher aspect ratio exerts more viscous/frictional force for transport of the fluid from the reservoir to the microchannel and hence as the dimension of the reservoir approaches

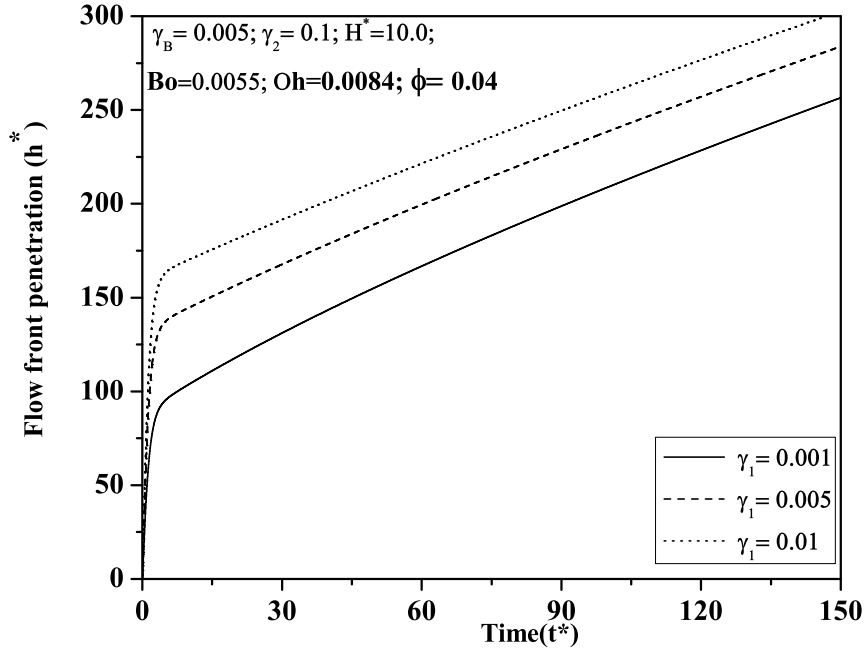


Figure 6.5: Transient response of a flow front transport for different aspect ratios for parallel plate arrangements of the capillary with $Bo=0.0055$, $Oh=0.0084$, $\gamma_B=0.005$, $\gamma_2 = 0.2$, $H^* = 10.0$ and $\phi = 0.04$

towards square cross-section, the frictional resistance increases. This results in decrease of penetration depth as the reservoir aspect ratio increases. In this case also the sudden jump in the penetration depth at the beginning of the process is observed.

Hence, from Figs. 6.4, 6.5 and 6.6 it can be seen that at the beginning of the capillary transport, the surface force dominates the gravity and hence a sudden jump in the penetration depth at the initial time instants is observed as opposed to a linear variation in the penetration depth with time. More importantly, this initial jump in the penetration depth is higher for lower width channels. Also, the difference in the penetration depth created in the capillary dominating region for different aspect ratio channels remains the same in the gravity dominating region, which occurs beyond the initial capillary dominating regime. Hence, at microscale the effect of capillarity at the begin-

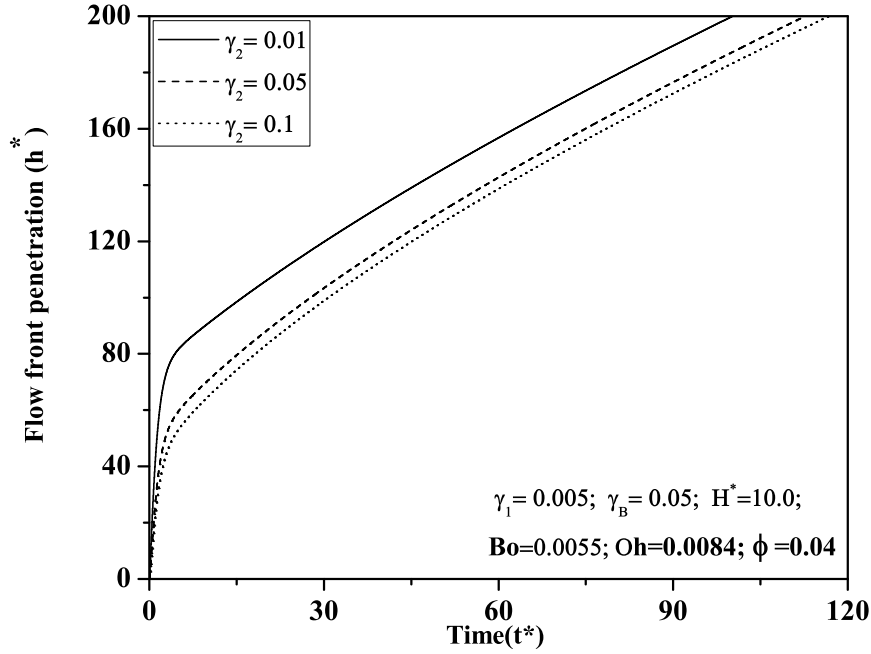


Figure 6.6: Transient response of a flow front transport for different aspect ratios of reservoir with $Bo=0.0055$, $Oh=0.0084$, $\gamma_B=0.005$, $\gamma_1 = 0.005$, $H^* = 10.0$ and $\phi = 0.04$

ning of the channel filling process can not be neglected and this becomes more predominant in case of smaller width microchannels.

Besides the geometrical configurations, the role of the physical properties of the fluid itself on the variation of the flow front transport is also important. As mentioned earlier, the presence of microbeads changes the physical properties and it depends on the concentration of the microparticles in the suspension i.e., volume fraction ϕ . The effect of change in the physical properties of the working fluid can be studied by varying the volume fraction of microparticles in the suspension. The case $\phi = 0$ represents the fluid without microbeads i.e., the working fluid only. The transient response of a flow front with different microbead volume fraction ϕ is depicted in Fig. 6.7. Here, ϕ is varied from 0% to 8%. The presence of microbeads in the fluid suspension delays the transport of flow front. The inset of Fig. 6.7 describe the surface

force dominating region which shows the jump in the flow front progression with different volume fraction. It has been demonstrated with experimental reported evidences (Waghmare and Mitra, 2010a), that the presence of microbead reduces the surface tension. Hence, higher volume fraction of microbeads suppresses the jump due to capillarity and delays the transport of the flow front. The flow front progresses till sufficient fluid is left in the reservoir. Hence, in each case with different volume fraction, the flow front attains the same penetration depth with different rates. The attainment of same depth with different volume fraction in the microchannel gets delayed as the volume fraction of microbeads increases.

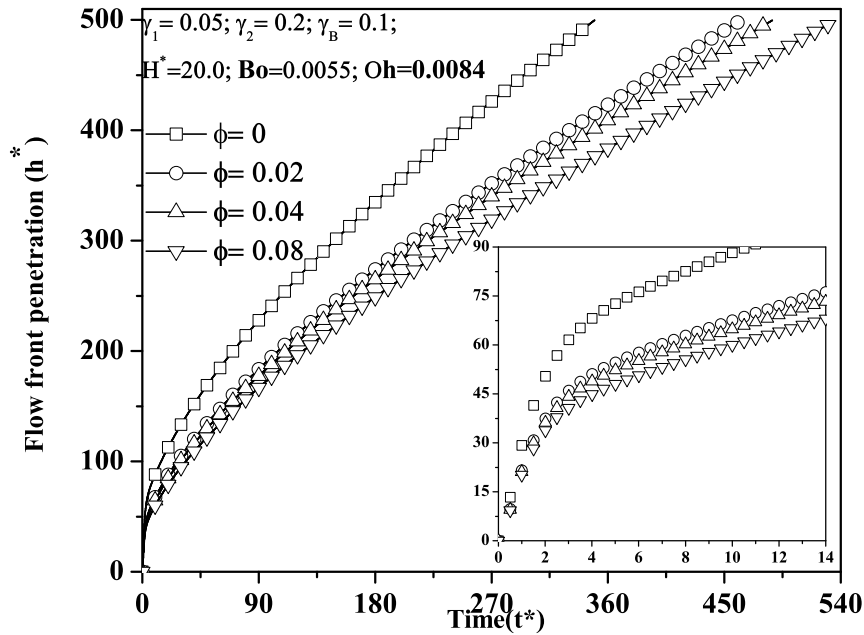


Figure 6.7: Transient response of a flow front transport for different concentrations of microbeads with $Bo=0.0055$, $Oh=0.0084$, $\gamma_1 = 0.05$, $\gamma_2 = 0.2$, $\gamma_B=0.1$ and $H^* = 20.0$. The case $\phi = 0$ represents the fluid without microbeads.

The overall theoretical study conducted so far suggest that, the behavior of flow front transport not only depends on the suspension properties but also depends on the microchannel and reservoir dimension. It is also demonstrated

that, the amount of microbead concentration decide the penetration depth along the microchannel. The capillary, gravitational and viscous forces are important forces acting on the fluid. Interplay between these forces decides whether the flow front transport is capillarity controlled or gravity dominant. Although the scaling among forces tends to suggest that the gravitation force is negligible at microscale, the reported analysis infers that with finite reservoir an added advantage due to gravity can be an useful tool for transporting fluid in microscale. This added force for the capillary transport can be utilized without any additional burden in the design of the LOC device.

6.4 Conclusion

Theoretical investigations for capillary transport of microbead suspension with reservoir effects are presented in this study. Initially, capillary flow with reservoir effects for fluid with effective physical properties of microbead suspension is reported. An expression for pressure field accounting the finite reservoir which is placed at the top of microchannel to gain the advantage of the gravitational head is proposed. The expression for pressure field accounts for both the finite reservoir effects and gravitational head. Correlations for change in the physical properties particularly in surface tension and contact angle are used from earlier reported experimental observations. The non-dimensional governing equation for capillary flow with microbead suspension considering finite reservoir effects is obtained, which is solved numerically. Detailed parametric study is performed to trace out the effects of different operating conditions on the flow front transport. At the beginning of the microchannel filling, the capillarity dominates and at the later time instance the gravity force dominates. The ratio of microchannel to reservoir width and fluid level in the reservoir decides the magnitude of capillarity and gravitational force. For reservoir with higher fluid level, the flow front progresses very slowly at the beginning of the transport but surpasses the penetration depth corresponding to the lower fluid level reservoir with time. Geometry of the microchannel and the reservoir also plays an important role in deciding capillary flow front trans-

port. It is observed that the microchannels of lower width results in higher capillarity. It is also found that the higher aspect ratio reservoirs exerts more resistance to transport of fluid from the reservoir to the microchannel. The concentration of the microbeads in suspensions influences the physical properties of the fluid, which in turn delays the capillary flow front progression.

References

- Barraza H. J., Kunapuli S., and O’Rear E. A., Advancing contact angles of Newtonian fluids during “high” velocity, transient, capillary-driven flow in a parallel plate geometry. *Journal of Physical Chemistry B*, 106(19):4979–4987, 2002.
- Batchelor G. K., *An introduction to fluid dynamics*. Cambridge University Press, 2002.
- Bhattacharya S. and Gurung D., Derivation of governing equation describing time-dependent penetration length in channel flows driven by non-mechanical forces. *Analytica Chimica Acta*, 666(1-2):51–54, 2010.
- Blute I., Pugh R., van de Pas J., and Callaghan I., Industrial manufactured silica nanoparticle sols. 2: Surface tension, particle concentration, foam generation and stability. *Colloids and Surfaces A: Physicochemical and Engineering Aspects*, 337(1-3):127–135, 2009.
- Brian B. and Chen J., Surface tension of solid-liquid slurries. *American Institute of Chemical Engineers*, 33(2):316–318, 1987.
- Dreyer M., Delgado A., and Path H. -J., Capillary rise of liquid between parallel plates under microgravity. *Journal of Colloid And Interface Science*, 163(1):158–168, 1994.
- Dreyer M., Delgado A., and Rath H. -J., Fluid motion in capillary vanes under reduced gravity. *Microgravity Science Technology*, 5(4):203–210, 1993.
- Geschke O., Klank H., and Telleman P., *Microsystem Engineering of Lab-on-a-Chip Devices*. Wiley-VCH, Weinheim, 2004.

- Hiemenz P. C. and Rajagopalan R., *Principles of Colloid and Surface Chemistry*. CRC Press,, 1997.
- Jeje A. A., Rates of spontaneous movement of water in capillary tubes. *Journal of Colloid And Interface Science*, 69(3):420–429, 1979.
- Jong W. R. , Kuo T. H., Ho S. W. , Chiu H. H., and Peng S. H., Flows in rectangular microchannels driven by capillary force and gravity. *International Communications in Heat and Mass Transfer*, 34(2):186–196, 2007.
- Juncker D., Schmid H., Drechsler U., Wolf H., Wolf M., Michel B., de Rooij N., and Delamarche E., Autonomous microfluidic capillary system. *Analytical Chemistry*, 74(24):6139–6144, 2002.
- Karniadakis G., Beskok A., and Aluru N., *Microflows and Nanoflows Fundamentals and Simulation*. Springer Berlin, New York, 2005.
- Kawaguchi H. , Functional polymer microspheres. *Progress in Polymer Science*, 25(8):1171–1210, 2000.
- Kihm K. D. and Deignan P., Dynamic surface tension of coal-water slurry fuels. *Fuel*, 74(2):295–300, 1995.
- Kung C., Chui C., Chen C., Chang C., and Chu C., Blood flow driven by surface tension in a microchannel. *Microfluid and Nanofluid*, 6(5):693–697, 2009.
- Levine S., Lowndes J., Watson E., and Neale G., A theory of capillary rise of a liquid in a vertical cylindrical tube and in a parallel-plate channel. *Journal of Colloid and Interface Science*, 73(1):136–151, 1980.
- Levine S., Reed P., and Watson J., A theory of the rate of rise a liquid in a capillary. *Colloid and Interface Science*, 3(1):403–419, 1976.
- Lim C. T. and Zhang Y., Bead-based microfluidic immunoassays: The next generation. *Biosensors and Bioelectronics*, 22(7):1197–1204, 2007.

- Mawardi A., Xiao Y., and Pitchumani R., Theoretical analysis of capillary-driven nanoparticulate slurry flow during a micromold filling process. *International Journal of Multiphase Flow*, 34(3):227–240, 2008.
- Newman S., Kinetics of wetting of surfaces by polymers; capillary flow. *Journal of Colloid and Interface Science*, 26(2):209, 1968.
- Nguyen N. and Wereley S., *Fundamentals and Applications of Microfluidics*. Artech House, New York, 2003.
- Peker S. and Helveci S., *Solid-liquid two phase flow*. Elsevier, Oxford, first edition, 2008.
- Saha A. A. and Mitra S. K., Effect of dynamic contact angle in a volume of fluid (VOF) model for a microfluidic capillary flow. *Journal of Colloid and Interface Science*, 339(2):461–480, 2009.
- Stange M., Dreyer M., and Rath H., Capillary driven flow in circular cylindrical tubes. *Physics of Fluids*, 15(9):2587–2601, 2003.
- Szekely J., Neumann A. W., and Chuang Y. K., The rate of capillary penetration and the applicability of the Washburn equation. *Journal of Colloid And Interface Science*, 35(2):273–278, 1971.
- Verpoorte E., Beads and chips: New recipes for analysis. *Lab-on-a-chip*, 3(4):60–68, 2003.
- Waghmare P. R. and Mitra S. K., Contact angle hysteresis of microbead suspensions. *Langmuir*, 26(22):17082–17089, 2010a.
- Waghmare P. R. and Mitra S. K., Modeling of combined electroosmotic and capillary flow in microchannels. *Analytica Chimica Acta*, 663(2):117–126, 2010b.
- Waghmare P. R. and Mitra S. K., On the derivation of pressure field distribution at the entrance of a rectangular capillary. *Journal of Fluid Engineering*, 132(5):Art. No. 054502, 2010.

- Walker G. M. and Beebe D. J., A passive pumping method for microfluidic devices. *Lab on a Chip - Miniaturisation for Chemistry and Biology*, 2(3): 131–134, 2002.
- Wang W., Zhou Z., Nandakumar K., Xu Z., and Masliyah J., Effect of charged colloidal particles on adsorption of surfactants at oil-water interface. *Journal of Colloid and Interface Science*, 274(2):625–630, 2004.
- Washburn E., The dynamics of capillary flow. *Physical Review*, 17(3):273-283, 1921.
- Xiao Y., Yang F., and Pitchumani R., A generalized flow analysis of capillary flows in channels. *Journal of Colloid and Interface Science*, 298(2):880–888, 2006.
- Yamada H, Yoshida Y, Terada N, Hagihara T., and Teasawa A., Fabrication of gravity-driven microfluidic device. *Review of Scientific Instruments*, 79 (12):Art. No. 124301, 2008.
- Yun K. S., Lee D., Kim H.-S. , and Yoon E., Multifunctional microwell plate for on-chip cell and microbead-based bioassays. *Sensors and Actuators B-Chemical*, 143(1):387–394, 2009.
- Zimmermann M., Schmid H., Hunziker P., and Delamarche E., Capillary pumps for autonomous capillary systems. *Lab on a Chip - Miniaturisation for Chemistry and Biology*, 7(1):119–125, 2007.

Chapter 7

Modeling of combined electroosmotic and capillary flow in microchannels¹

7.1 Introduction

The recent developments in micro-electro mechanical systems (MEMS) technologies and micromachining techniques opened a new era in fabrication of microfluidic systems consisting of pumps, mixers, valves, filters, etc. In microfluidic devices, the transport of fluid can be achieved by mechanical, non-mechanical pumping or by combination of mechanical and non-mechanical pumping. As the size of these devices decreases, the availability of large surface to volume ratio makes surface forces dominant. These surface forces are termed as surface tension forces or capillary effects which arise due to the large interface between fluid and the bounding channel walls. The flow rate in a pressure driven flow is proportional to the cube of the characteristic channel dimension which requires a very large pressure drop in microchannels. This draws attention towards non-mechanical pumping mechanism, which not only solves the problem of pressure drop but it also eliminates the use of moving components in these devices. The non-mechanical transport can be achieved by electrical, chemical, thermal, magnetic or surface tension effects (Karniadakis et al., 2005; Waghmare and S. K. Mitra, 2008).

¹A version of this chapter has been published as a cover article. Waghmare and Mitra, 2010, *Analytica Chimica Acta*, 663 (2), 117-126

Higher surface to volume ratio allows capillary transport in microfluidic devices. The study of the fluid motion due to capillarity has been well studied theoretically as well as experimentally. Starting with Washburn (Washburn, 1921) and till date by Saha et al. (Saha et al., 2009), researchers have derived the flow equation to describe capillary phenomenon with different geometries for different applications and compared their results with experimental data (Saha and Mitra, 2009a). Theoretical models are developed by balancing several forces acting on the fluid control volume. The novelty in each study is the addition of a new force or an effect which is unaccounted earlier but being an important force to decide the behavior of flow front development. An excellent theoretical model with generalized governing equation for capillary transport in rectangular and circular capillary is presented by Xiao et al. (Xiao et al., 2006). The analytical solution of this model is compared with experimental results. The development of such theoretical models is extensively reviewed by Mawardi et al. (Mawardi et al., 2008). Important modifications in Washburn equations are inclusion of inertial force, entrance pressure difference and dynamic contact angle between the moving liquid front and the solid wall in addition to the viscous, surface tension and gravity forces. It is also demonstrated that, the variation in the contact angle also changes the behavior of capillary transport within a microchannel (Saha and Mitra, 2009b). After the inclusion of dynamic contact angle, the theoretical model shows good agreement with experimental results. The dynamic contact angle can be included using empirical correlations, which prescribe the contact angle as a function of time (Barraza et al., 2002; Hamraoui and Nylander, 2002).

The wide range of advantages of non-mechanical pumps attract the attention towards electrokinetic pumping. The substrate materials for microfluidics materials acquire a surface electric charge when brought into contact with an electrolyte (Li, 2004). There are several mechanisms like ionization, dissociation of ions, isomorphic substitution, etc., which make the surface electrically charged (Masliyeh and Bhattacharjee, 2006). These surface charges forms an electrical double layer(EDL) while filling the channel with the buffer solu-

tion. The movement of the liquid with respect to stationary surface charges can be achieved by applying external electric field across the channel. This is known as electroosmotic flow which is one of the electrokinetic transport in microscale. Electroosmosis finds wide applications and the review of electrokinetic flow in microchannels and its applications can be found in Nguyen and Wereley (Nguyen and Wereley, 2003), Rawool and Mitra (Rawool and Mitra, 2006) and Stone et al. (Stone et al., 2004). Hsieh et al. (Hsieh et al., 2006) demonstrated experimentally that, the flow behavior in electrokinetic flow deviates significantly from the predictions of conventional fluid mechanics. The transient analysis of electroosmotic flow without capillary effect is studied extensively and the review of these studies can be found elsewhere (Chang and Wang, 2008; Keh and Tseng, 2001; Yan et al., 2007). Recently, an analysis on a capillary transport (Chakraborty, 2005) and electroosmotically driven capillary filling process (Chakraborty, 2007) of non-Newtonian fluid are reported by Chakraborty. In the case of electroosmotically driven capillary process, the effect of hemetocratic fraction on the flow front displacement and velocity are demonstrated.

However, literature suggests that, generalized theoretical analysis for electroosmotically assisted capillary filling process has not been presented yet. Hence, a theoretical analysis of electrokinetic flows with capillary effect is required to decide the optimum design and performance of micro-devices. The objective of the present study is to investigate the effect of capillary and electroosmotic transport parameters on flow front displacement and velocity behavior. Experiments are needed for the approval of such electroosmotic effect on the capillary transport. A generalized analysis of electroosmotically assisted capillary flow in a microchannel incorporating the transient effect for a range of different operating conditions is presented here. The analysis is based on the capillary flow model presented by Dreyer et al. (Dreyer et al., 1993) and Xiao et al. (Xiao et al., 2006). A generalized non-dimensional second order differential equation is derived and it is solved numerically to perform the parametric study.

7.2 Formulation of the Mathematical Model and Solution

Theoretical model for the investigation of the fluidic transport in an electroosmotically assisted capillary flow is presented here. The schematic of the microchannel is shown in Fig. 7.1. The electric field is applied in the axial direction i.e., parallel to the direction of flow. The microchannel of width $2B$ and depth of $2W$ is considered for the analysis. The lower aspect ratio ($\gamma = \frac{B}{W} \ll 1$) causes the capillary transport in microchannel and the axial electric field results into an electrokinetic transport. The magnitude and direction of the electrokinetic transport depends on electrokinetic parameters.

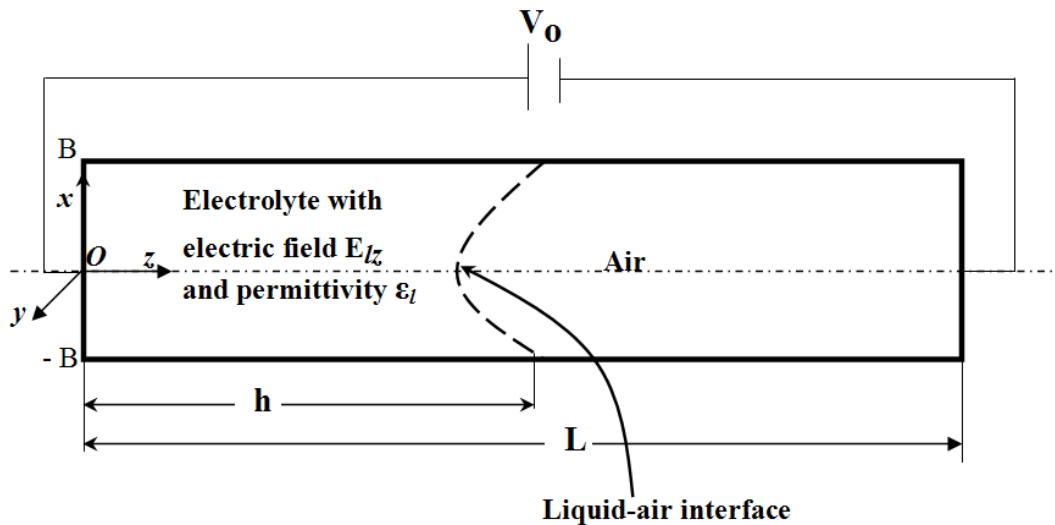


Figure 7.1: Schematic of the microchannel of width $2B$, depth $2W$ and of length L considered for electroosmotically assisted capillary transport.

The integral momentum equation for homogeneous, incompressible and Newtonian fluid is given by Eq. 7.1 where h is the penetration depth. This equation represents the transient movement of the liquid front meniscus along the z -axis, which is termed as penetration depth. This movement is measured from the coordinate origin to the point of intersection of the meniscus front

with z -axis (Dreyer et al., 1993).

$$\sum F_z = \frac{\partial}{\partial t} \int_0^h \int_{-W}^W \int_{-B}^B \rho v_z dx dy dz + \int_{-W}^W \int_{-B}^B v_z (-\rho v_z) dx dy \quad (7.1)$$

Here, ρ is the density of the fluid, $\sum F_z$ is the summation of all forces acting on fluid under consideration viz., viscous (F_v), gravity ($F_g = 4\rho ghBW$), electroosmotic (F_{eo}) and pressure forces at the flow front (F_{pf}) and at the inlet (F_{pi}).

$$\sum F_z = F_v + F_g + F_{pf} + F_{pi} + F_{eo} \quad (7.2)$$

In the present study, in addition to the capillary effect, the influence of electroosmosis (EO) is to be taken into account. Therefore, it is necessary to derive the velocity profile which can take care of capillary as well as EO. In electroosmotic flow, the distribution of potential due to applied electric field is governed by the Poisson's equation. Assuming Debye-Huckel approximation with Poisson's potential distribution within the liquid part of the channel, the charge density (ρ_e) is given by Eq. 7.3. Where, $1/\kappa$ is the characteristic thickness of the electric double layer (EDL) which represents the Debye length i.e., $\lambda = 1/\kappa$ and ϵ_l is the dielectric permittivity of the liquid. In the present analysis the wall potential (ψ_w) is assumed as the zeta potential (ζ) (Masliyah and Bhattacharjee, 2006).

$$\rho_e = -\epsilon_l \frac{d^2\psi}{dx^2} = -k^2 \epsilon_l \psi_w \frac{\cosh(\kappa x)}{\cosh(\kappa B)} \quad (7.3)$$

The modified Navier-Stokes equation including electrokinetic effect is,

$$\rho \frac{\partial v_z}{\partial t} = \mu \frac{\partial^2 v_z}{\partial x^2} + \frac{dp}{dz} + \rho_e E_{lz} \quad (7.4)$$

where, $\frac{dp}{dz}$ and E_{lz} are applied pressure drop and electric field along the flow of the channel, respectively. The velocity in Eq. 7.4 can be decoupled in the following manner (Keh and Tseng, 2001),

$$v_z(x, t) = v_{z\infty}(x) + v_{zt}(x, t) \quad (7.5)$$

where, $v_{z\infty}(x)$ is the velocity field at steady state, which can be written as (Batchelor, 2002),

$$v_{z\infty}(x) = \frac{B^2}{2\mu} \frac{dp}{dz} \left[1 - \left(\frac{x}{B} \right)^2 \right] - \frac{\epsilon_l E_{lz} \zeta}{\mu} \left[1 - \frac{\cosh(\kappa x)}{\cosh(B\kappa)} \right] \quad (7.6)$$

The transient coupling of the velocity can be obtained from following equation (Keh and Tseng, 2001),

$$\frac{1}{\rho} \frac{\partial v_{zt}}{\partial t} = \mu \frac{\partial^2 v_{zt}}{\partial x^2} \quad (7.7)$$

The method of separation of variable is used to obtain the solution of Eq. 7.7 and is given as,

$$v_{zt}(x, t) = 2 \sum_{n=1}^{\infty} (-1)^n \left\{ \frac{1}{B\mu\lambda_n^3} \frac{dp}{dz} - \frac{\varepsilon E_z \zeta}{B\mu} \left[\frac{\kappa^2}{\lambda_n (\kappa^2 + \lambda_n^2)} \right] \right\} \times \cos(\lambda_n x) \exp(-\nu \lambda_n^2 t) \quad (7.8)$$

where, $\lambda_n = \frac{(2n-1)\pi}{2B}$ and ν is the kinematic viscosity of the fluid. Hence, the transient fluid velocity profile $v_z(x, t)$ can be obtained by combining Eqs. 7.6 and 7.8.

The average velocity across the channel can be expressed in terms of Onsager transport coefficients L_{11} and L_{12} as (Keh and Tseng, 2001),

$$v_z(x, t)_{avg} = L_{11} \frac{dp}{dz} + L_{12} E_{tz} \quad (7.9)$$

The Onsager transport coefficients can be derived by Eqs.7.5, 7.6 and 7.8 as,

$$L_{11} = \frac{B^2}{3\mu} \left[1 - \sum_{n=1}^{\infty} \frac{96}{(2n-1)^4 \pi^4} \exp \left[-\frac{(2n-1)^2 \pi^2 \nu t}{4B^2} \right] \right] \quad (7.10a)$$

$$L_{12} = \frac{\varepsilon \zeta}{\mu} \left\{ \left[\sum_{n=1}^{\infty} \frac{32 (B\kappa)^2 \exp \left[-\frac{(2n-1)^2 \pi^2 \nu t}{4B^2} \right]}{\pi^2 (2n-1)^2 [(2B\kappa)^2 + \pi^2 (2n-1)^2]} \right] - \left[\frac{B\kappa - \tanh(B\kappa)}{B\kappa} \right] \right\} \quad (7.10b)$$

It is to be noted that, the steady state velocity profile (Eq.7.6) for combined electroosmotic and pressure driven flow can also be obtained from Eq. 7.9 as $t \rightarrow \infty$. In Eq. 7.5 the pressure drop term is replaced by average velocity (as done for capillary flow (Dreyer et al., 1993)) so that the velocity profile is

obtained in terms of the penetration depth, as given by Eq. 7.11. The detailed expressions for different terms(A_1 to A_7) used in Eq. 7.11 are reported in Appendix A-2.

$$v_z(x, t) = \left\{ \sum_{n=1}^{\infty} A_1 \cos(\lambda_n x) \exp(-\nu \lambda_n^2 t) + A_2 \left(1 - \frac{x^2}{B^2} \right) \right\} \\ \left\{ \frac{\mathbf{h}'(\mathbf{t})}{A_3 [1 - \sum_{n=1}^{\infty} A_4 \exp(-\lambda_n \nu t)]} - \frac{\sum_{n=1}^{\infty} [A_5 \exp(-\lambda_n \nu t)] - A_6}{[1 - \sum_{n=1}^{\infty} A_4 \exp(-\lambda_n^2 \nu t)]} \right\} \\ - \left\{ \sum_{n=1}^{\infty} A_7 \cos(\lambda_n x) \exp(-\lambda_n^2 \nu t) + A_8 \left[1 - \frac{\cosh(x\kappa)}{\cosh(B\kappa)} \right] \right\} \quad (7.11)$$

Equation 7.11 is derived based on the following assumptions:

- (i) The Change in contact angle, velocity profile and electric field due to accumulation of charges on the liquid-air interface is neglected as the meniscus depth is small
- (ii) It is known that, the electroviscous effect mainly depends on the streaming potential and the EDL thickness in nanochannels, which can be neglected for microchannels (Mortensen and Kristensen, 2008)
- (iii) In the present analysis, the flow is governed by the pressure drop due to surface tension and electroosmosis. Therefore, the magnitude of streaming potential is very small as compared to the combined electroosmotic and pressure driven flow where the externally applied pressure drop is a major factor to cause the streaming potential (Li, 2002). Hence, the effect of streaming potential is neglected.

During the filling process, the electrolyte penetrates the empty channel replacing the gas present in the channel. Therefore, the net applied voltage V_0 is the combination of electric field which acts on the electrolyte(E_{lz}) and the gaseous part(E_{gz}) of the channel and can be expressed as,

$$V_o = E_{lz}h + E_{gz}(L - h) \quad (7.12)$$

It is to be noted that at the interface, the electric field at either phases is related through following relationship (Yang et al., 2004),

$$E_{lz}\epsilon_l = E_{gz}\epsilon_g \quad (7.13)$$

Hence, combining Eq. 7.12 and Eq. 7.13 the electric field in the electrolyte is given by Eq. 7.14,

$$E_{lz} = \frac{V_0\epsilon_g}{L\epsilon_l + h(\epsilon_g - \epsilon_l)} \quad (7.14)$$

By expressing E_{lz} in terms of penetration depth(h), the transient response of the electroosmotic component in the velocity profile given in Eq. 7.11 has been addressed. The velocity profile given by Eq. 7.11 can be used to calculate the necessary terms in the governing equation. The viscous force during the transport of flow front can be calculated using Eq. 7.15,

$$F_v = 2 \int_0^h \int_{-W}^W \mu \left(\frac{\partial v_z}{\partial x} \right)_{x=B} dydz \quad (7.15)$$

where, μ is the dynamic viscosity of the fluid. The entrance effect at the microchannel inlet is considered to be due to the pressure force at the entry of the microchannel. This can be computed using the pressure distribution at the inlet of the microchannel. Levine et al. (Levine et al., 1976) reported for the first time the pressure field at the entrance of the circular capillary. Typically the entrance pressure for the rectangular capillary is derived based on a circular capillary geometry (Dreyer et al., 1993; Xiao et al., 2006), where an equivalent radius for a rectangular capillary is used. Such approximation may not be valid for a high aspect ratio channel. Hence, the modified expression for rectangular capillary as shown in Eq. 7.16 is used in the present analysis. Further details of the derivation of this can be seen elsewhere (Waghmare and Mitra, 2010). Finally, the pressure force at the entry of microchannel can be calculated using Eq. 7.17,

$$p(0, t) = p_{atm} - \frac{4\mu}{\pi B} \frac{dh}{dt} - \rho B \left\{ \left(\frac{3\pi}{20} + \frac{1}{2\pi} \right) + \frac{2}{\pi} \left[\ln \frac{r_\infty}{B} \right] \right\} \frac{d^2h}{dt^2} + \rho \left\{ -\frac{6}{5} + \frac{3}{\pi^2} \right\} \left(\frac{dh}{dt} \right)^2 \quad (7.16)$$

$$F_{pi} = - \int_{-W}^W \int_{-B}^B p(x, y, 0) dx dy \quad (7.17)$$

Here r_∞ is the radial distance far away from the capillary inlet where the capillary forces vanishes. In this study, this is taken as ten times the half channel width. The pressure force at the flow front is estimated by balancing the force due to surface tension(σ) and the ambient pressure force. In this analysis, the effect of applied electric field on the liquid-air interface is neglected therefore, the pressure on the liquid front can be derived using Young-Laplace equation. The dynamic contact angle θ_d can be used instead of constant equilibrium contact angle but the experimental based empirical relation is required for the inclusion of the dynamic contact angle. Hence, the equilibrium contact angle θ_e , is considered for deriving the force at the flow front. Here, the force at the flow front can be written as (Xiao et al., 2006),

$$F_{pf} = 4BW \left[\sigma \left(\frac{\cos \theta_e}{B} - p_o \right) \right] \quad (7.18)$$

The electroosmotic effect is added by considering the additional force i.e., electroosmotic force(F_{eo}), which can be estimated by (Chakraborty, 2007),

$$F_{eo} = \int_0^h \int_{-W}^W \int_{-B}^B \rho_e E_{lz} dx dy dz \quad (7.19)$$

The detail explanation for deriving the forces can be found elsewhere (Chakraborty, 2007; Mawardi et al., 2008; Xiao et al., 2006).

The momentum equation, Eq. 7.1 can now be rewritten using the forces given in Eqs. 7.15 , 7.17, 7.18 and 7.19. The transient term is evaluated using the same velocity profile given by Eq. 7.11. Typically, for microfluidic applications, the Reynolds number for the flow within the capillary is very small and hence inertial effect can be neglected (Bhattacharya and Gurung, 2010). Therefore, in the present analysis the convective term is neglected. After rearranging the terms, the dimensional form of the governing equation for the penetration depth as a function of time can be written, the details of which are presented in Appendix A-2.

A non-dimensional analysis is performed to get the generalized non-dimensional equation. The non-dimensional analysis provides a better ability to perform

parametric study which decides the transient behavior of penetration depth. The characteristic time(t_0) and length (h_0) are used to represent the non-dimensional time (t^*) and the penetration depth(h^*), respectively. The characteristic time and length are defined as, $t_0 = \frac{\rho(2B)^2}{12\mu}$ and $h_0 = 2B$, respectively. Using these definitions, a generalized non-dimensional governing equation for electroosmotically assisted capillary filling process in a microchannel is given by Eq. 7.20,

$$(h^* + C'_1) \frac{d^2 h^*}{dt^{*2}} + C'_2 \left(\frac{dh^*}{dt^*} \right)^2 + [C'_3 h^* + C'_4] \frac{dh^*}{dt^*} + C'_5 h^* + C'_6 = 0 \quad (7.20)$$

For the purpose of brevity, the expression for constants (C'_1 to C'_6) of Eq. 7.20 are provided in Appendix A-2.1. These constants are combination of different non-dimensional groups which depends on the geometry. Certain non-dimensional groups are defined by the non-dimensional numbers like Bond number(Bo), Ohnesorge number(Oh) and Electroosmotic number(E_o). Some are represented as characteristic groups like aspect ratio (γ), non-dimensional length (L^*) and non-dimensional permittivity (ϵ^*). The non-dimensional length of channel(L^*) is the ratio of the total length of the channel to width of channel, aspect ratio(γ) is the ratio of width to depth and ϵ^* is non-dimensional dielectric constant, which is ratio of air to liquid permittivity. Remaining non-dimensional groups are representation of ratio of forces, which are viscous, gravity, electroosmotic and surface tension forces. Gravity, viscous and electroosmotic forces are normalized with surface tension forces to get the non-dimensional form of the governing equation as a function of different non-dimensional numbers. The Ohnesorge number ($Oh = \frac{\mu}{\sqrt{2B\rho\sigma}}$) is the ratio of viscous to surface tension force and the Bond number ($Bo = \frac{\rho g(2B^2)}{\sigma}$) is the ratio of gravity to surface tension force. A new non-dimensional group, Electroosmotic number ($E_o = \frac{V_0 \epsilon_g \zeta}{2B\sigma}$), which is the ratio of electroosmotic to surface tension force is formulated here. The present analysis is mainly focused on the response of penetration depth and velocity of the flow front due to change in E_o under different operating conditions. The governing equation is a second order ordinary differential equation, the solution for penetration depth with

respect to time can be evaluated analytically (Xiao et al., 2006) or numerically (Morales et al., 2005). In the present analysis, the fourth order Runge-Kutta method is used to obtain the solution with zero penetration depth and zero velocity as initial conditions. Here, $t^* = 0$ represents the starting of the capillary filling process.

7.3 Results and Discussion

The variation in the penetration depth(h^*) and velocity($v^* = \frac{dh^*}{dt^*}$) with different operating parameters is presented in this section. As mentioned earlier, after the non-dimensionalizing of the governing equation, a new non-dimensional group is obtained i.e., E_o due to inclusion of electroosmosis. It is important to decide the operating range of E_o to perform the parametric study. The range of electrokinetic parameters can be found in (Karniadakis et al., 2005; Lee et al., 2005). A detailed explanation for deciding the operating range of E_o with respect to surface tension is recently reported by Waghmare and Mitra (Waghmare and Mitra , 2009). In addition to E_o, Bo and Oh , different electroosmotic flow parameters are also considered to perform the parametric study. In the present analysis, it is assumed that, the contact angle is independent of the electroosmotic parameter. Thus the parametric study is performed with constant contact angle of 27° .

The transient behavior of penetration depth under different electroosmotic operating conditions is demonstrated in Fig. 7.2. Here, the effect of positive and negative ranges of E_o numbers on the penetration depth is studied. In Fig. 7.2, the E_o number varies from -0.01 to 0.01 . Negative range of E_o numbers can be achieved by Changing the applied electric field or the surface charges. It is observed that, the transient behavior of penetration depth due to positive and negative ranges of E_o numbers deviates from a pure capillary flow($E_o = 0$). In a pure capillary transport, the penetration depth attains the equilibrium penetration depth asymptotically and the time taken to attain the equilibrium depth is a function of viscous, gravity, surface tension forces and capillary geometry. Similarly, the attainment of equilibrium penetration

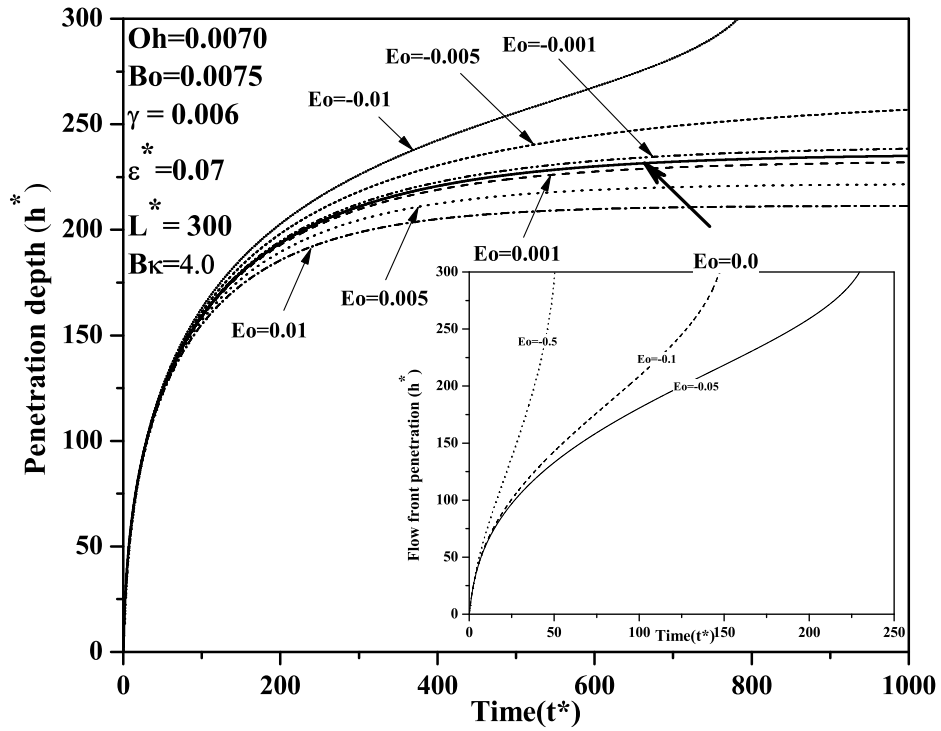


Figure 7.2: Transient response of a penetration depth for $0.01 \leq E_o \leq -0.01$ with $Oh = 0.0070$, $Bo = 0.0075$, $\gamma = 0.006$, $\epsilon^* = 0.07$, $L^* = 300$ and $B\kappa = 4$. $E_o = 0$ represents pure capillary flow

depth is observed in combined electroosmotic and capillary transport for lower range of E_o numbers. In the combined flow, the flow with positive E_o numbers ($E_o > 0$) opposes the capillary transport. Therefore, it retards the capillary flow and subsequently reduces the equilibrium penetration depth. In case of negative range of E_o numbers ($E_o < 0$), the assistance to capillary transport is observed. In general we can say that, the flow with $E_o < 0$ is electroosmotically assisted flow whereas, the flow with $E_o > 0$ is electroosmotically retarded flow. For $0 > E_o > -0.005$, the increment in equilibrium penetration depth as compared to pure capillary transport is observed. Hence, the magnitude of equilibrium penetration depth increases as the magnitude of $-E_o$ increases. It is observed that, the magnitude of assistance in electroosmotically assisted flow and retardation in electroosmotically retarded flow is different for the same positive and negative E_o numbers. Further, the increase in the magnitude of $-E_o$ ($E_o = -0.01$) changes the behavior quite dramatically. In the present analysis, the entire length of channel (L^*) is taken as 300. In case of $E_o = -0.01$, the penetration depth attains the value of L^* instead of attaining the equilibrium penetration depth within the channel, which represents the complete filling of the channel. The rate of penetration depth for complete filling of the channel depends on the magnitude of negative E_o , which is illustrated in the inset of Fig 7.2. As the magnitude of $-E_o$ increases, the rate of penetration depth approaches towards the linear behavior at large time instants. The physical situation similar to Fig. 7.2 is presented in Fig. 7.3. The variation in an electric field within the electrolyte is also presented in the inset of the Fig 7.3. This electric field decides the nature and magnitude of the electroosmotism. The transient behavior of penetration depth is similar to the non-dimensional analysis presented in Fig. 7.2.

However, the rate of penetration depth shows nonlinearity at the beginning of the channel filling process, as shown in Fig 7.4. This nonlinearity arises due to the viscous, surface and gravity forces. The effect of all these parameters can be investigated with the parametric study. In general for the combined flow, two phenomena are observed- the attainment of the equilibrium pene-

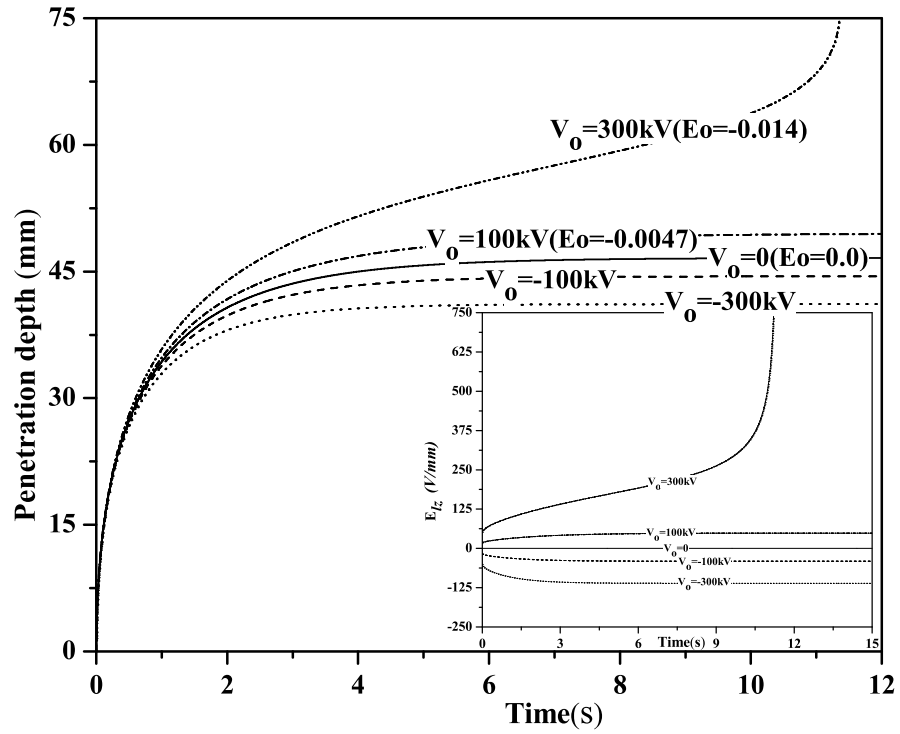


Figure 7.3: Variation in the penetration depth for vertically oriented channel with water as electrolyte where $B = 100\mu m$, $W = 400\mu m$, $L = 75mm$, $\zeta = -75mV$ and constant contact angle of 27° . Inset shows the variation in the electric field within the electrolyte as flow front progresses under different applied voltages

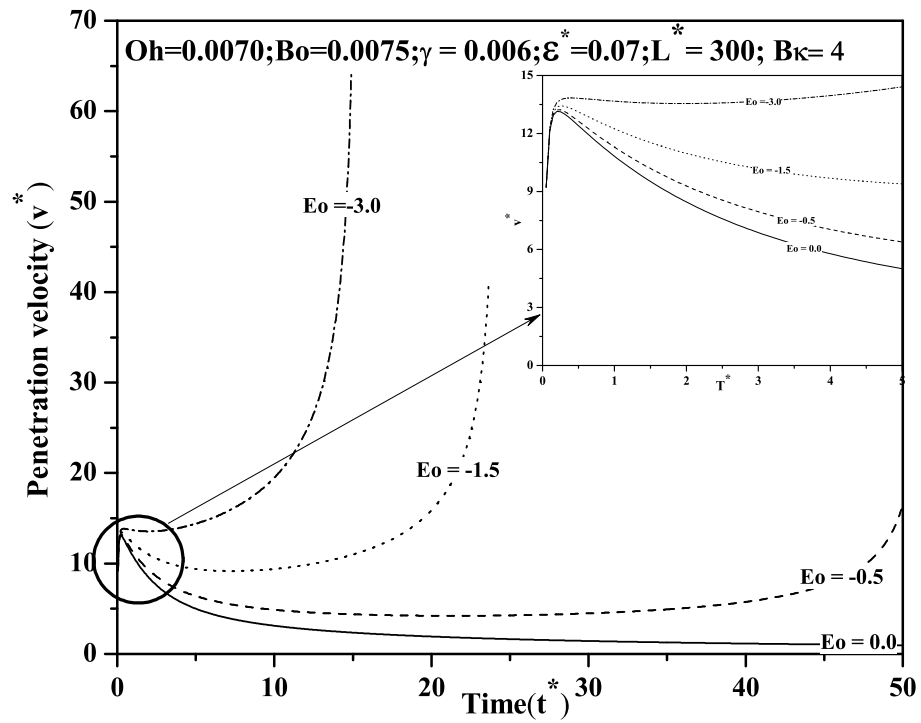


Figure 7.4: Transient response of a flow front velocity for different E_0 with $Oh = 0.0070$, $Bo = 0.0075$, $\gamma = 0.006$, $\epsilon^* = 0.07$, $L^* = 300$ and $B\kappa = 4$ with constant contact angle of 27°

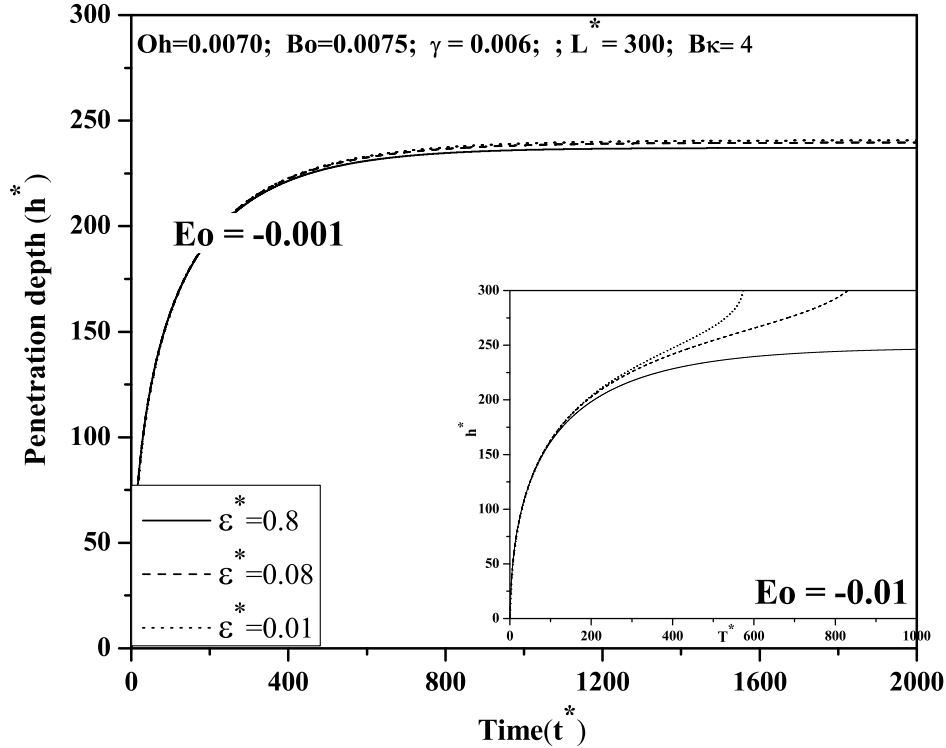


Figure 7.5: Transient response of a penetration depth for different non-dimensional permittivity(ϵ^*) with $Oh = 0.0070$, $Bo = 0.0075$, $\gamma = 0.006$, $E_o = -0.001$ and -0.01 , $L^* = 300$ and $B\kappa = 4$ with constant contact angle of 27°

tration depth and complete filling of the channel. When the attainment of equilibrium penetration depth occurs, it shows that the flow is dominated by capillary transport parameters. In case of complete filling of the channel, the electroosmosis dominates and overcome the capillary resistance which allows it to fill the complete channel.

The variation in the flow front velocity under electroosmotically dominant conditions is demonstrated in Fig. 7.4 where only complete filling of the channel is observed. At the beginning of the channel filling process, sudden jump in the velocity is observed. Inset of Fig. 7.4 shows the variation in magnitude of the jump in flow front velocity at the beginning of the filling process. As

the liquid meniscus advances inside the microchannel, its velocity reduces due to the increase in viscous and gravity forces in a capillary flow. In case of capillary flow ($E_o = 0$), this retardation of velocity leads to zero velocity and hence equilibrium penetration depth. In electroosmotically assisted flow, the additional electroosmotic force overcomes the resistance offered by the viscous and gravity force. Finally this contributes towards the filling of the channel instead of attaining the equilibrium penetration depth within the channel. Theoretical as well as experimental studies are reported on the behavior of the transient velocity profile in pure electroosmotic flow (Keh and Tseng, 2001; Yan et al., 2007). In such studies, the analysis is based on the assumption that, the channel is filled completely prior to application of the electric field. Keh and Tseng (Keh and Tseng, 2001) reported a theoretical study for pure electroosmotic flows in completely filled capillary. They reported that, the transient electroosmotic velocity far away from the capillary wall attains the plateau. Similar observation is reported with experimental results and theory presented by Yan et. al (Yan et al., 2007). For electroosmotically dominant condition ($E_o = -3.0$), the flow front velocity also tries to attain the plateau but as the flow front approaches towards the exit of the channel, it experiences a higher electric field near the electrode. This higher electric field attracts the flow front and disturbs the plateau. Therefore, a sudden jump in the velocity at the channel exit is observed corresponding to large time instants in case of combined flow.

The permittivity of the medium is an important parameter to decide the nature of electrokinetic transport in an electrokinetic flow. The ϵ^* is the ratio of the permittivity of the air to the permittivity of the liquid. The voltage is applied across the length of the microchannel containing two phases. Therefore, it is important to understand the combined effect of the liquid and air present in the channel on the flow transport. Figure 7.5 represents the effect of non-dimensional permittivity (ϵ^*) on the transient response of the penetration depth at two different E_o . In the range of $-0.001 > E_o$ the transport behavior is dominated by the capillary transport therefore, the attainment of

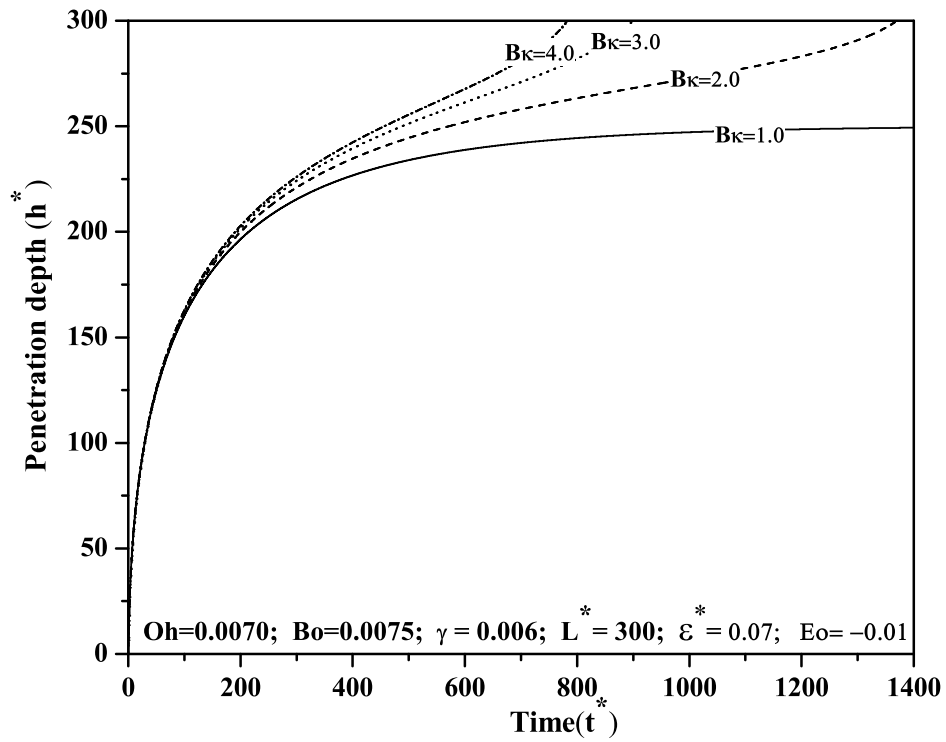


Figure 7.6: Transient response of a penetration depth for different non-dimensional Debye-length($B\kappa$) with $Oh = 0.0070$, $Bo = 0.0075$, $\gamma = 0.006$, $E_o = -0.01$, $L^* = 300$ and $\epsilon^* = 0.07$ with constant contact angle of 27°

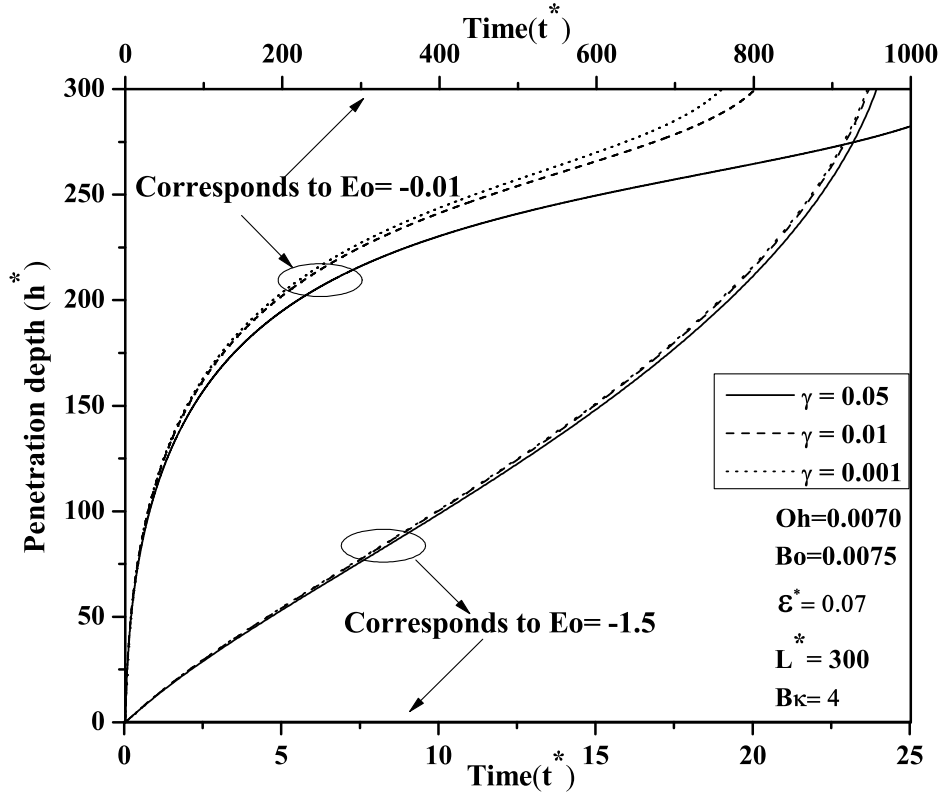


Figure 7.7: Transient response of a penetration depth for different aspect ratios(γ) with $Oh = 0.0070$, $Bo = 0.0075$, $\epsilon^* = 0.07$, $E_o = -0.01$ and -1.5 , $L^* = 300$ and $B\kappa = 4$ with constant contact angle of 27°

equilibrium penetration depth is observed. As the penetration depth increases, the amount of the liquid(electrolytes) in the channel under the electric field increases progressively. Hence, the increment in liquid permittivity i.e. decrement in ϵ^* results in the increase of the equilibrium penetration depth. The inset of Fig. 7.5 shows the variation in the penetration depth under electroosmotically dominant condition. In such case, the complete filling of the channel is expected but for lower permittivity electrolyte($\epsilon^* = 0.8$) the equilibrium penetration depth is observed.

The effect of Debye length($1/\kappa$) on the potential distribution across the channel is studied extensively in electroosmotic flow. Keh and Tseng (Keh and Tseng, 2001) theoretically demonstrated that, as $B\kappa$ decreases towards

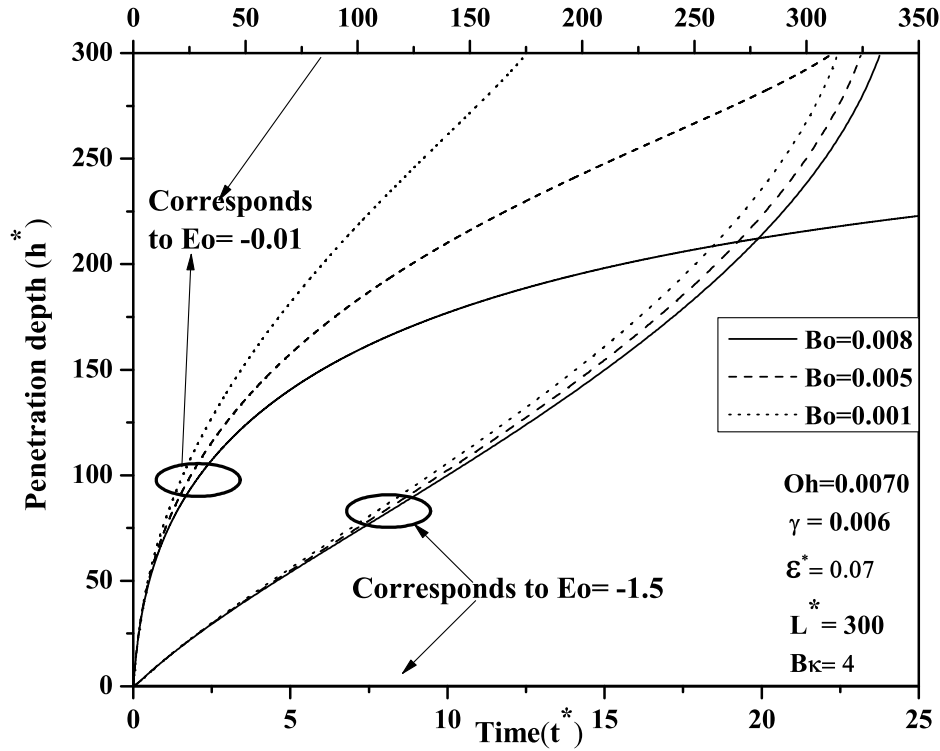


Figure 7.8: Transient response of a penetration depth for different values of Bond number(Bo) with $Oh = 0.0070$, $\epsilon^* = 0.07$, $E_o = -0.01$ and -1.5 , $L^* = 300$ and $B\kappa = 4$ with constant contact angle of 27°

the minimum value i.e. zero, the potential distribution approaches towards wall potential. It is also demonstrated that, for larger $B\kappa$ values the velocity profile becomes like pluglike flow with larger maximum velocity as compare to the flow with smaller $B\kappa$. Similar effect is observed in Fig. 7.6, where the variation in the penetration depth is plotted for different values of $B\kappa$. For smaller $B\kappa$ values, the delay in the channel filling of channel is observed and as $B\kappa$ increases, the channel filling time decreases. The geometrical dimensions of the channel also decide the magnitude of the different forces and subsequently the magnitude and behavior of penetration depth and flow front velocity. Figure 7.7 shows the variation of the penetration depth due to change in the aspect ratio(γ) of the channel. In pure capillary transport, as γ increases,

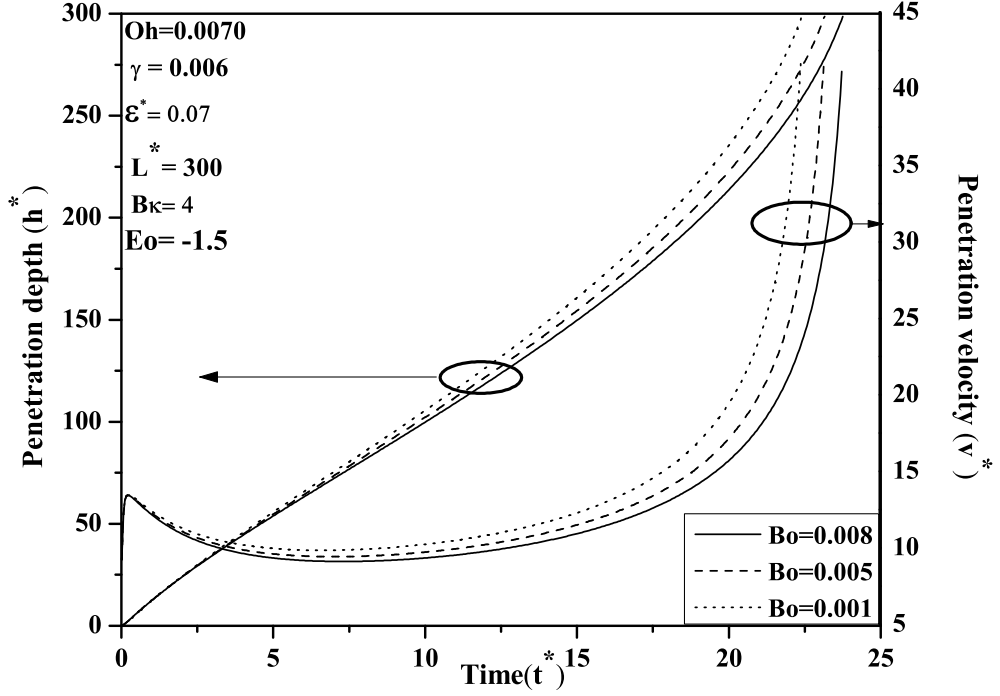


Figure 7.9: Transient response of a penetration depth and flow front velocity for different values of Bond number(Bo) with $Oh = 0.0070$, $\epsilon^* = 0.07$, $E_o = -1.5$, $L^* = 300$ and $B\kappa = 4$ with constant contact angle of 27°

the equilibrium penetration depth decreases due to the increase in gravity and viscous forces (Xiao et al., 2006). In case of combined flow, the similar behavior is observed. The same effect is studied under combined flow conditions i.e., at $E_o = -0.01$ and $E_o = -1.5$. In higher electroosmotically dominant conditions($E_o = -1.5$), the effect of larger aspect ratios is less as compared to the effect under lower electroosmosis($E_o = -0.01$). Thus at higher electroosmotic flow conditions($E_o = -1.5$), the effect of increment in the aspect ratio has negligible impact on the complete channel filling time. It is to be noted that for lower γ , thicker EDL affects the electroosmotic flow (Baldessari, 2008; Dutta, 2007), which is not considered here.

The effect of gravity and viscous forces on penetration depth and flow front

velocity under combined flow conditions is discussed in this section. As the gravity force decreases (decrement in Bo number), the fluid approaches towards microgravity, and hence the effect of Bo is negligible. As Bo increases, the gravity force on the fluid increases which causes the delay in the filling of the channel. The effect of gravity force for $E_o = -0.01$ and $E_o = -1.5$ is presented in Fig. 7.8. The delay in the filling of the channel due to increment in Bo is observed in both the cases. These results are similar to the results under variation in γ i.e., the difference in the delay of complete filling of the channel for different Bo is negligible at higher electroosmotic flow conditions ($E_o = -1.5$). At higher electroosmotic flow conditions the velocity at the channel exit increases as the Bo decreases. This increment in velocity for $E_o = -1.5$ is shown in Fig. 7.9.

The viscous force plays a vital role as compared to the gravity force in the combined flow. In pure capillary transport, the magnitude of equilibrium penetration depth is independent of the viscous force. The Oh number or in other words the viscous force decides the delay in attaining the equilibrium penetration depth. Similarly, in case of combined flow, the delay in the filling of complete channel depends on Oh number. In Fig. 7.10, the variation in the penetration depth for $E_o = -0.01$ and $E_o = -1.5$ is observed under different viscous forces. The effect of viscous force at $E_o = -0.01$ delays the filling of the complete channel with increment in Oh . For higher electroosmotic flow ($E_o = -1.5$), the delay in complete filling of the channel is also observed with the increment in the Oh . As shown in Fig. 7.11, the increment in Oh with $E_o = -1.5$ reduces the velocity of the flow front. Hence, the viscous effect can not be neglected at the higher electroosmotic conditions.

In combined flow, it is observed that, during the filling process of the microchannel, the magnitude of surface, gravity (Bo) and viscous (Oh) forces influences the behavior of the rate of penetration depth. It is also demonstrated that, the amount of deviation in the penetration depth and the flow front velocity or in other words, the departure from the electroosmotically dominant behavior is a function of all the forces included in this analysis. The resistance

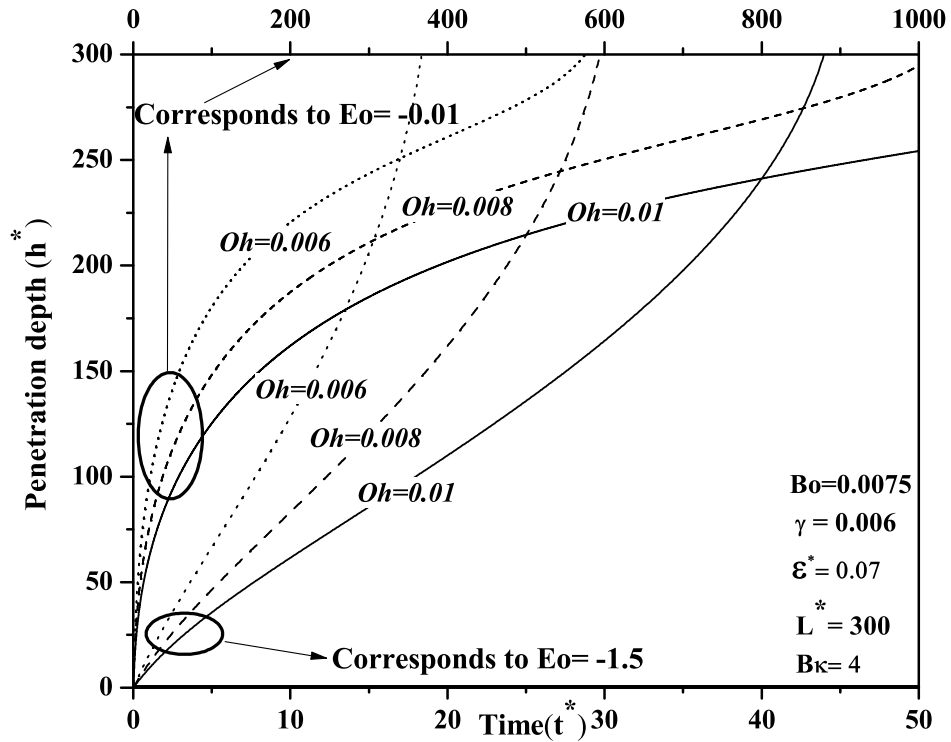


Figure 7.10: Transient response of a penetration depth and flow front velocity for different values of Ohnesorge number(Oh) with $Bo = 0.0075$, $\gamma = 0.006$, $\epsilon^* = 0.07$, $E_o = -0.01$ and -1.5 , $L^* = 300$ and $B\kappa = 4$ with constant contact angle of 27°

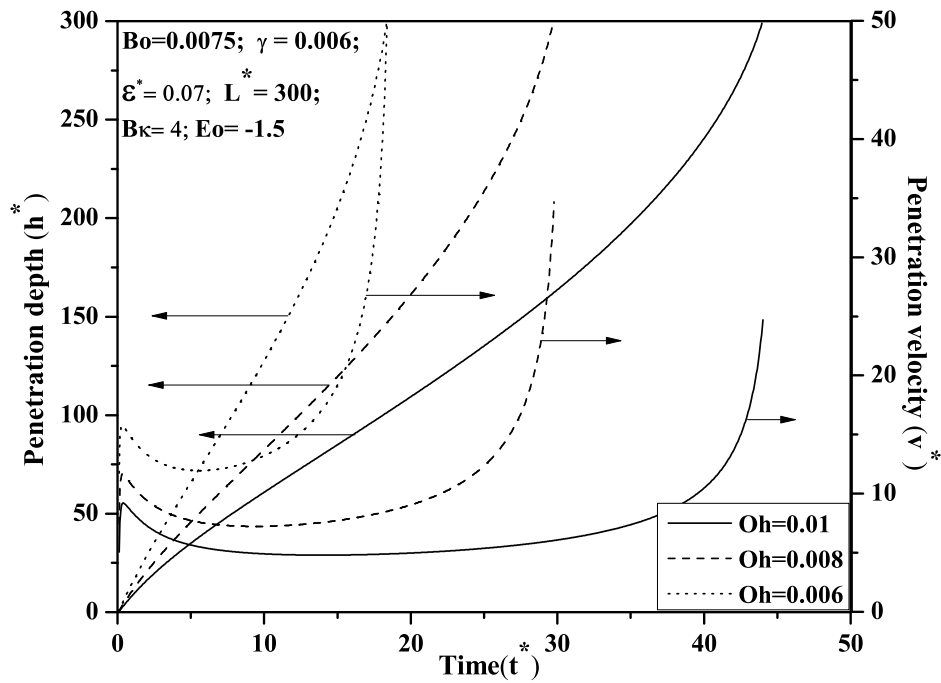


Figure 7.11: Transient response of a penetration depth and flow front velocity for different values of Ohnesorge number(Oh) with $Bo = 0.0075$, $\gamma = 0.006$, $\epsilon^* = 0.07$, $E_o = -1.5$, $L^* = 300$ and $B\kappa = 4$ with constant contact angle of 27°

offered by all possible forces like viscous, gravity and surface tension is different under different operating conditions and the magnitude of electrokinetic force required to overcome this resistance changes the behavior of penetration depth under each operating condition.

7.4 Conclusion

A theoretical model for investigating the fluid transport in a microchannel under the combined influence of electroosmosis and capillarity is presented. This is particularly important for microfluidic applications where the flow has low Reynolds number. The non-dimensional governing equation for electroosmotically assisted capillary flow is obtained which includes viscous, gravity, surface tension and electroosmotic forces. A new non-dimensional group for electroosmotic force, E_o is derived through non-dimensional analysis, which is a ratio of the electroosmotic and the surface tension forces. The parametric study is presented to trace out the effect of different operating conditions on penetration depth and velocity. It is necessary to perform experiments to confirm the reported observations. From the parametric study, the following important conclusions can be made:

- Transient behavior of penetration depth and penetration velocity deviates from pure capillary behavior ($E_o = 0$) with positive as well as negative range of E_o numbers. Positive E_o number retard the capillary transport whereas, negative E_o number assist the capillary transport.
- The equilibrium penetration depth similar to pure capillary transport is observed for all positive and larger $-E_o$ number range. In electroosmotically dominant combined flow ($E_o \leq -0.01$) the complete filling of the channel is observed and the rate of filling depends on the magnitude of $-E_o$.
- The flow of lower permittivity liquid in microchannels delays the capillary transport. The increase in permittivity, results in the transition of pure capillary to electroosmotically assisted flow.

- For lower values of $B\kappa$, delay in the filling of the channel is observed. The large values of $B\kappa$ accelerates the capillary transport in combined flow.
- The effect of aspect ratio and gravitational force is dominant in lower range of $E_o(E_o \leq -0.001)$. In combined flow, the viscous force plays a vital role as compared to gravitational force. In electroosmotically assisted flow, large viscous and gravity forces retard the fluid transport.

References

- Baldessari F., Electrokinetics in nanochannels. Part I . Electric double layer overlap and channel-to-well equilibrium. *Journal of Colloid and Interface Science*, 325(2):526–538, 2008.
- Barraza H. J., Kunapuli S., and O’Rear E. A., Advancing contact angles of Newtonian fluids during “high” velocity, transient, capillary-driven flow in a parallel plate geometry. *Journal of Physical Chemistry B*, 106(19):4979–4987, 2002.
- Batchelor G. K., *An introduction to fluid dynamics*. Cambridge University Press, 2002.
- Bhattacharya S. and Gurung D., Derivation of governing equation describing time-dependent penetration length in channel flows driven by non-mechanical forces. *Analytica Chimica Acta*, 666(1-2):51–54, 2010.
- Chakraborty S., Dynamics of capillary flow of blood into a microfluidic channel. *Lab on a Chip - Miniaturisation for Chemistry and Biology*, 5(4):421–430, 2005.
- Chakraborty S., Electroosmotically driven capillary transport of typical non-newtonian biofluid in rectangular microchannels. *Analytica Chimica Acta*, 605(2):175–184, 2007.
- Chang C. and Wang C., Starting electrosmotic flow in an annulus and in rectangular channel. *Electrophoresis*, 29(14):2970, 2008.
- Dreyer M., Delgado A., and Rath H. -J., Fluid motion in capillary vanes under reduced gravity. *Microgravity Science Technology*, 5(4):203–210, 1993.

- Dutta D., Electroosmotic transport through rectangular channels with small zeta potentials. *Journal of Colloid and Interface Science*, 315(2):740–746, 2007.
- Hamraoui A. and Nylander T., Analytical approach for the lucas-washburn equation. *Journal of Colloid and Interface Science*, 250(2):415, 2002.
- Hsieh S. S., Lin H. C., and Lin C. Y., Electroosmotic flow velocity measurements in a square microchannel. *Colloid and Polymer Science*, 284(11):1275–1286, 2006.
- Karniadakis G., Beskok A., and Aluru N., *Microflows and Nanoflows Fundamentals and Simulation*. Springer Berlin, New York, 2005.
- Keh H. and Tseng H., Transient electrokinetic flow in fine capillaries. *Journal of Colloid and Interface Science*, 242(2):450, 2001.
- Lee G., Lin C., Lee K., and Lin Y., On the surface modification of microchannels for microcapillary electrophoresis chips. *Electrophoresis*, 26(24):4616–4624, 2005.
- Levine S., Reed P., and Watson J., A theory of the rate of rise a liquid in a capillary. *Colloid and Interface Science*, 3(1):403–419, 1976.
- Li D., *Surface Science Series by A. Delgado*. Springer Berlin, 2002.
- Li D., *Interface Science and Technology- Volume 2; Electrokinetics in Microfluidics*. Elsevier Academic Press, London, 2004.
- Masliyah J. and Bhattacharjee S., *Electrokinetic and Colloid Transport Phenomena*. Willey, New Jersey., 2006.
- Mawardi A., Xiao Y., and Pitchumani R., Theoretical analysis of capillary-driven nanoparticulate slurry flow during a micromold filling process. *International Journal of Multiphase Flow*, 34(3):227–240, 2008.

- Morales A., Pitchumani R., Garino T., Gutmann A., and Domeier L., Fabrication of ceramic microstructures via microcasting of nanoparticulate slurry. *Journal of the American Ceramic Society*, 88(3):570, 2005.
- Mortensen N. A. and Kristensen A., Electroviscous effects in capillary filling of nanochannels. *Applied Physics Letters*, 92(6), 2008.
- Nguyen N. and Wereley S., *Fundamentals and Applications of Microfluidics*. Artech House, New York, 2003.
- Rawool A. S and Mitra S. K., Numerical simulation of electroosmotic effect in serpentine channels. *Microfluidics and Nanofluidics*, 2(3):261–269, 2006.
- Saha A. A. and Mitra S. K., Effect of dynamic contact angle in a volume of fluid (VOF) model for a microfluidic capillary flow. *Journal of Colloid and Interface Science*, 339(2):461–480, 2009a.
- Saha A. A. and Mitra S. K., Numerical study of capillary flow in microchannels with alternate hydrophilic-hydrophobic bottom wall. *Journal of Fluids Engineering, Transactions of the ASME*, 131(6):0612021–06120212, 2009b.
- Saha A. A., Mitra S. K. , Tweedie M., Roy S., and McLaughlin J., Experimental and numerical investigation of capillary flow in su8 and pdms microchannels with integrated pillars. *Microfluidics and Nanofluidics*, 7(4): 451–465, 2009. ISSN 1613-4982.
- Stone H. A., Stroock A. D., and Ajdari A., Engineering flows in small devices: Microfluidics toward a lab-on-a-chip. *Annual Review of Fluid Mechanics*, 36:381–411, 2004.
- Waghmare P. R. and Mitra S. K., On the derivation of pressure field distribution at the entrance of a rectangular capillary. *Journal of Fluid Engineering*, 132(5):Art. No. 054502, 2010.
- Waghmare P. R. and Mitra S. K., A generalized analysis of electroosmotically driven capillary flow in rectangular microchannels. In *Proceedings of Sev-*

enth International ASME Conference on Nanochannels, Microchannels and Minichannels, Pohang, South Korea, ICNMM2009-8271, June 22-24, 2009.

Waghmare P. R. and Mitra S. K., Investigation of combined electro-osmotic and pressure-driven flow in rough microchannels. *Journal of Fluids Engineering, Transactions of the ASME*, 130(6), 2008.

Washburn E., The dynamics of capillary flow. *Physical Review*, 17(3):273-283, 1921.

Xiao Y., Yang F., and Pitchumani R., A generalized flow analysis of capillary flows in channels. *Journal of Colloid and Interface Science*, 298(2):880-888, 2006.

Yan D., Yang C., Nguyen N. T., and Huang X., Diagnosis of transient electrokinetic flow in microfluidic channels. *Physics of Fluids*, 19:Art. No. 017114, 2007.

Yang J., Lu F., and Kwok D. Y., Dynamic interfacial effect of electroosmotic slip flow with a moving capillary front in hydrophobic circular microchannels. *Journal of Chemical Physics*, 121(15):7443-7448, 2004.

Chapter 8

General discussion and conclusion

8.1 Overview and Summary

The present thesis addresses some important questions related to the passive and non-mechanical transport in microchannels, especially capillary transport. Under the purview of this general theme, we address the following issues:

- Investigation of the effect of a developing velocity profile on the capillary filling problem.
- Development of a generalized expression of the appropriate inlet (entrance) pressure field valid for a microchannel of any aspect ratio.
- Development of empirical correlations connecting the wettability parameters with the concentration (volume fraction) in BSA solution or microbead suspension, and use these correlations to describe the microcapillary transport of these liquids.
- Analysis of the effect of gravitational or electroosmotic body force in modulating the capillary transport.

Capillary transport, which depends on the wettability of the liquid and the solid, is one of the foremost passive pumping approaches. Through comprehensive mathematical modeling, influence of different operating and system parameters on the capillary transport have been pinpointed. For example,

unlike the existing approaches that invariably considers a fully-developed velocity profile for the description of capillary filling, our model considers a more general case of a developing velocity profile, and accordingly manifests several non-trivial effects in the classical capillary-filling problem that gets overlooked with the consideration of a developed velocity profile (Waghmare and Mitra, 2012).

Another aspect, closely related to the scope of the *above-stated* study, is the formulation of the appropriate driving pressure-field at the capillary entrance. In this thesis, we develop an accurate expression for the pressure field for microchannels with high aspect ratios (Waghmare and Mitra, 2010). The gross simplifications intrinsic to the existing expressions of the pressure field make it inappropriate for applications for such high aspect ratio channels. In fact, the difference between these two (existing and newly proposed) pressure fields is exhibited in the significant differences in the corresponding penetration depths during the capillary filling process (Waghmare and Mitra, 2012).

Very often to transport biomolecules in microfluidic devices, one needs BSA solution or microbead suspension as the liquid medium. Therefore, investigations on the wetting properties of these liquid media are extremely important, particularly in the light of a proposed capillary transport. In this thesis, experiments are performed to systematically analyze the wetting behavior of these two media. From the results, we derive important correlations expressing the surface tension and the equilibrium contact angle as functions of the concentration of the BSA solution (Waghmare and Mitra, 2012a) and the volume fraction of the microbead suspension (Waghmare and Mitra, 2010a). Such correlations will serve as analogous to *Equations of State* for describing these two most widely used liquid solvents. Additionally, using these newly hypothesized correlations, effect of volume fraction (of microbead suspension) on the microcapillary transport has been analyzed (Waghmare and Mitra, 2010b).

Finally, capillary transport in presence of additional body forces, such as gravitational (Waghmare and Mitra, 2010b) or electroosmotic body force (Waghmare and Mitra, 2010c), has been studied. These two effects are found to

not only augment the capillary transport, but also introduce important non-trivialities in the overall capillary dynamics.

8.2 Scope of Future Work

The developing velocity profile model, or the generalized entrance pressure-field expressions are substantial sophistications of the existing analyses. A more important step forward would be to self consistently describe the capillary filling and the wetting of the capillary. This can be done by expressing the overall curvature of the moving capillary meniscus as a function of the dynamic contact angle, especially relevant for a very thin capillary (where the length scale over which the dynamic contact angle varies becomes important). Under such a condition, the driving pressure-gradient which depends on the meniscus curvature becomes a function of the dynamic contact angle, and accordingly the velocity field would also be a function of the dynamic contact angle. Therefore, one will be able to achieve a perfectly coupled problem, where both the capillary filling velocity and the wetting dynamics are mutually inter-connected. Through appropriate micro-visualization techniques (e.g., micro-PIV), one can observe and establish this model which will mutually interconnect the velocity field and the dynamic contact angle. Further, in case of the closed microchannel, where the width and depth are comparable, one can consider the double parabolic or paraboloid velocity profile instead of one-dimensional parabolic velocity for the analysis.

The correlations connecting the wetting parameters and the properties of the liquid media like the BSA solution or the microbead suspension are mostly valid for those ranges of parameters of these liquid media that are typically employed in biomedical applications. It will be an interesting study to investigate the validity of these correlations at other concentration ranges. Secondly, it will be useful to develop theoretical models that can correctly identify the important physical effects which dictate this relation between the wetting properties and the concentration (or volume fraction) – in such a case we shall be able to connect the possible differences in the correlations to the changing

dynamics at different ranges of concentration (or volume fraction).

Finally, the combined electroosmotic and capillary transport model can be considerably augmented by developing a relation that interconnects the Electric Double Layer (which dictates the electroosmotic transport) with the corresponding dynamic contact angle – this will be analogous to the “electrowetting” scenario where the EDL electrostatic energy modifies the apparent contact angle. In such a case, we shall be able to define a transport where the capillary and the electroosmotic forces are mutually coupled, and not simply linearly superposed.

References

- Waghmare P. and Mitra S., A comprehensive theoretical model of capillary transport in rectangular microchannels. *Microfluidics and Nanofluidics*, 12 (1-4):53–63, 2012.
- Waghmare P. R. and Mitra S. K., On the derivation of pressure field distribution at the entrance of a rectangular capillary. *Journal of Fluid Engineering*, 132(5):Art. No. 054502, 2010.
- Waghmare P. R. and Mitra S. K., Contact angle hysteresis of Bovine Serum Albumin (BSA) solution/metal (Au-Cr) coated glass substrate, *Colloid Polymer Science*, DOI: 10.1007/s00396-012-2756-1, 2012.
- Waghmare P. R. and Mitra S. K., Contact angle hysteresis of microbead suspensions. *Langmuir*, 26(22):17082–17089, 2010a.
- Waghmare P. R. and Mitra S. K., Finite reservoir effect on capillary flow of microbead suspension in rectangular microchannels. *Journal of Colloid and Interface Science*, 351(2):561–569, 2010b.
- Waghmare P. R. and Mitra S. K., Modeling of combined electroosmotic and capillary flow in microchannels. *Analytica Chimica Acta*, 663(2):117–126, 2010c.

Appendix

A-1 Detailed explanation of momentum equation

The Eqs. 2.1, 6.1 and 7.1 are the different forms of the generalized integral momentum equation. The right hand side of these equations is the rate of change of momentum of a system, which is derived using *Reynolds Transport Theorem*. The Reynolds Transport Theorem provides the relationship between the rate of change of any extensive property and the variation of this property associated with the control volume. Here we use the Reynolds Transport Theorem to obtain the change of momentum. For a control volume presented with dotted line in Fig. 2.1 and representative of the control volume considered for analysis is shown in Fig. A-1

The rate of change of momentum for that control volume can be expressed as,

$$\frac{\partial}{\partial t} \int_0^h \int_{-W}^W \int_{-B}^B \rho v_z dx dy dz + \int_{-W}^W \int_{-B}^B v_z (-\rho v_z) dx dy \quad (\text{A-1})$$

The first term of Eq. A-1 is the rate of change of momentum inside the control volume whereas the second term represents the net rate of flux of momentum through the control surface. Here, in case of capillary flow, the momentum flux at the entrance of capillary is considered. The other surface i.e., air-liquid interface moves with the capillary filling velocity therefore, no outlet momentum flux takes place at the air-liquid interface. These two terms of momentum equation are also known as transient and convective terms of the momentum equation, respectively. The transient term with velocity profile from Eq. 6.3 can be given as,

$$\frac{\partial}{\partial t} \int_0^h \int_{-W_1}^{W_1} \int_{-B_1}^{B_1} \rho_e v_z dx dy dz = 4\rho_e B_1 W_1 \left[h \frac{d^2 h}{dt^2} + \left(\frac{dh}{dt} \right)^2 \right] \quad (\text{A-2})$$

and with the same velocity profile the convective term can be written as,

$$\int_{-W_1}^{W_1} \int_{-B_1}^{B_1} v_z (-\rho_e v_z) dx dy = -\frac{24}{5} \rho B_1 W_1 \left(\frac{dh}{dt} \right)^2 \quad (\text{A-3})$$

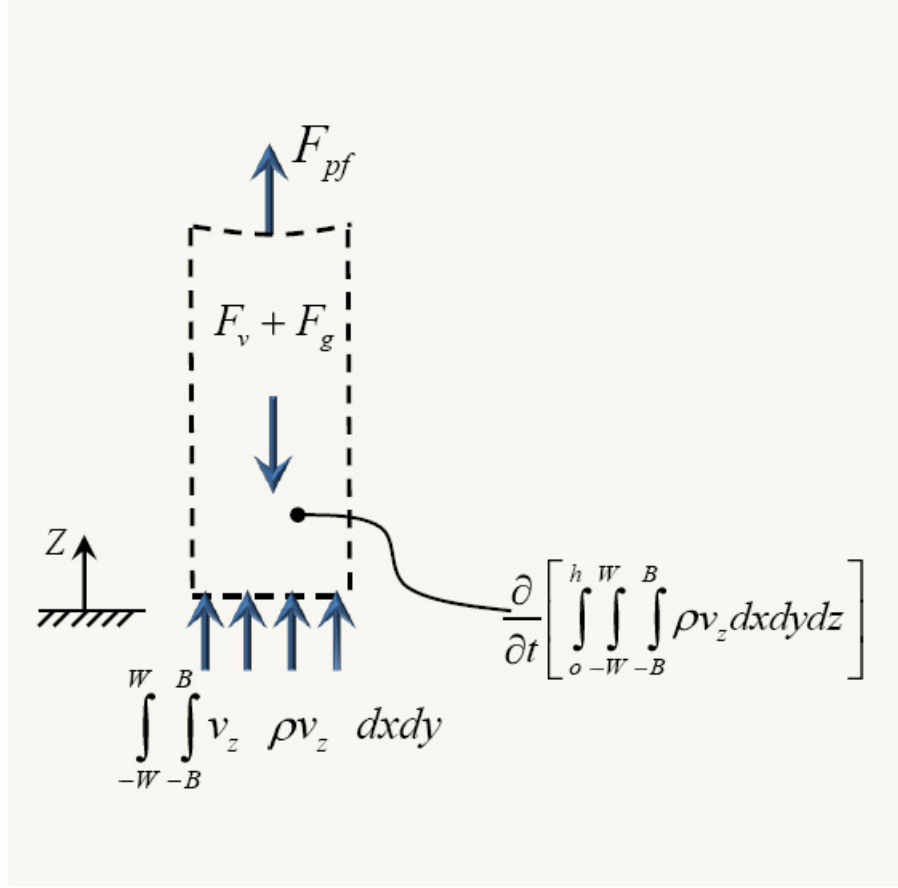


Figure A-1: Free body diagram for a control volume considered in mathematical analysis.

The left hand side of Eq. 6.1 is the summation of forces term as presented in Eq.6.2. Different forces of this summation are;

$$F_v = \frac{-12\mu_e h W_1}{B_1} \frac{dh}{dt}, \quad (\text{A-4})$$

$$F_{pf} = 4B_1 W_1 \left[\sigma_e \left(\frac{\cos\theta}{B_1} - \frac{1}{W_1} \right) - p_0 \right], \quad (\text{A-5})$$

In the literature (Dreyer et al., 1994), it is experimentally observed that the air-liquid interface is of saddle shape and to account for this shape the second radius of curvature is considered as $-W_1$ in Eq. A-5.

$$F_g = 4B_1 W_1 \rho_e g h \quad (\text{A-6})$$

and from Eq. 6.6 the pressure force at the inlet of the microchannel can be calculated as,

$$F_{pi} = 4B_1W_1 \times p(x, y, t) \quad (\text{A-7})$$

Replacing Eqs. A-2 to A-5 in Eq 6.1 and one can obtain the dimensional form of governing equation as presented in , Eq. 6.11.

A-2 Dimensional governing equation

The detailed dimensional form of the governing equation is presented on the next page.

$$\begin{aligned}
& \frac{[2\lambda_n A_2 B - (-1)^n 3A_1 e^{-\lambda_n^2 \nu t}]}{3B\lambda_n A_3 [1 - A_4 e^{-\lambda_n^2 \nu t}]} \mathbf{h}(\mathbf{t}) \mathbf{h}''(\mathbf{t}) + 2.096B \mathbf{h}''(\mathbf{t}) \\
& + \left\{ \frac{[2\lambda_n A_2 B - (-1)^n 3A_1 e^{-\lambda_n^2 \nu t}]}{3B\lambda_n A_3 [1 - A_4 e^{-\lambda_n^2 \nu t}]} + 0.245 \right\} \mathbf{h}'(\mathbf{t})^2 - \left\{ \frac{\sigma}{\rho} \left[\frac{\cos\theta}{B} - \frac{1}{W} \right] \right\} \\
& \left\{ -\frac{\lambda_n \nu [2\lambda_n A_2 B - (-1)^n 3A_1 e^{-\lambda_n^2 \nu t}]}{3A_3 B [1 - A_4 e^{-\lambda_n^2 \nu t}]^2} - \frac{[2\lambda_n A_2 B - (-1)^n 3A_1 e^{-\lambda_n^2 \nu t}] \lambda_n \nu}{3A_3 B [1 - A_4 e^{-\lambda_n^2 \nu t}]} \right. \\
& + \frac{[2\lambda_n A_2 B - (-1)^n 3A_1 e^{-\lambda_n^2 \nu t}] \lambda_n^2 \nu}{3\lambda_n A_3 B [1 - A_4 e^{-\lambda_n^2 \nu t}]} + \frac{2\lambda_n^2 A_2 \nu}{3A_2 [1 - A_4 e^{-\lambda_n^2 \nu t}]} \\
& \left. - \frac{(-1)^n \mu A_1 \lambda_n e^{-\lambda_n^2 \nu t}}{A_3 \rho B [1 - \sum_{n=1}^{\infty} A_4 e^{-\lambda_n^2 \nu t}]} + \frac{2\mu A_2}{A_3 \rho B^2 [1 - \sum_{n=1}^{\infty} A_4 e^{-\lambda_n^2 \nu t}]} \right\} \mathbf{h}(\mathbf{t}) \mathbf{h}'(\mathbf{t}) \\
& + \left\{ \frac{(-1)^n A_7 e^{-\lambda_n^2 \nu t}}{\lambda_n B} - A_8 \beta_3 + \frac{1.273\mu}{\rho B} + \frac{A_3 A_6 [2\lambda_n A_2 B - (-1)^n 3A_1 e^{-\lambda_n^2 \nu t}]}{3\lambda_n A_3 B [1 - A_4 e^{-\lambda_n^2 \nu t}]} \right. \\
& \left. - \frac{A_3 A_5 e^{-\lambda_n^2 \nu t} [2\lambda_n A_2 B - (-1)^n 3A_1 e^{-\lambda_n^2 \nu t}]}{3\lambda_n A_3 B [1 - A_4 e^{-\lambda_n^2 \nu t}]} \right\} \mathbf{h}'(\mathbf{t}) \\
& + \left\{ \frac{A_3 A_5 \lambda_n \nu e^{-\lambda_n^2 \nu t} [2\lambda_n A_2 B - (-1)^n 3A_1 e^{-\lambda_n^2 \nu t}]}{3A_3 B [1 - A_4 e^{-\lambda_n^2 \nu t}]^2} - \frac{(-1)^n A_7 \lambda_n \nu e^{-\lambda_n^2 \nu t}}{B} \right. \\
& - \frac{A_3 A_6 \lambda_n \nu [2\lambda_n A_2 B - (-1)^n 3A_1 e^{-\lambda_n^2 \nu t}]}{3A_3 B [1 - A_4 e^{-\lambda_n^2 \nu t}]^2} + \frac{2\mu A_2 A_6}{\rho B^2 [1 - \sum_{n=1}^{\infty} A_4 e^{-\lambda_n^2 \nu t}]} \\
& + \frac{A_3 A_5 \lambda_n \nu e^{-\lambda_n^2 \nu t} [2\lambda_n A_2 B - (-1)^n 3A_1 e^{-\lambda_n^2 \nu t}]}{3A_3 B [1 - A_4 e^{-\lambda_n^2 \nu t}]} + \frac{2\lambda_n^2 A_2 A_6 \nu}{3 [1 - A_4 e^{-\lambda_n^2 \nu t}]} \\
& - \frac{\lambda_n A_3 A_6 \nu [2\lambda_n A_2 B - (-1)^n 3A_1 e^{-\lambda_n^2 \nu t}]}{3A_3 B [1 - A_4 e^{-\lambda_n^2 \nu t}]} - \frac{2\lambda_n^2 A_2 A_5 \nu}{3e^{\lambda_n^2 \nu t} [1 - A_4 e^{-\lambda_n^2 \nu t}]} \\
& + \frac{\lambda_n^2 A_3 A_6 [2\lambda_n A_2 B - (-1)^n 3A_1 e^{-\lambda_n^2 \nu t}]}{3\lambda_n A_3 B [1 - A_4 e^{-\lambda_n^2 \nu t}]} - \frac{\sum_{n=1}^{\infty} 2\mu A_2 A_5 e^{-\lambda_n^2 \nu t}}{\rho B^2 [1 - \sum_{n=1}^{\infty} A_4 e^{-\lambda_n^2 \nu t}]} \\
& + \frac{2\mu A_2 A_6}{\rho B^2 [1 - \sum_{n=1}^{\infty} A_4 e^{-\lambda_n^2 \nu t}]} - \frac{(-1)^n \mu A_1 \lambda_n A_6 e^{-\lambda_n^2 \nu t}}{\rho B [1 - \sum_{n=1}^{\infty} A_4 e^{-\lambda_n^2 \nu t}]} \\
& \left. + \frac{\sum_{n=1}^{\infty} (-1)^n \mu A_1 \lambda_n A_5 e^{-2\lambda_n^2 \nu t}}{\rho B [1 - \sum_{n=1}^{\infty} A_4 e^{-\lambda_n^2 \nu t}]} + \frac{(-1)^n \lambda_n A_7 \mu e^{-\lambda_n^2 \nu t}}{\rho B} + g \right\} \mathbf{h}(\mathbf{t}) = 0
\end{aligned}$$

Different coefficients used in the dimensional governing equations are as follows;

$$\begin{aligned}
A_1 &= (-1)^n A_2 \left[\frac{4}{(B\lambda_n)^3} \right] \\
A_2 &= \frac{3 B^2}{2 3\mu} \\
A_3 &= \frac{B^2}{3\mu} \\
A_4 &= \frac{96}{(2n-1)^4 \pi^4} \\
A_5 &= \frac{\beta_1 \beta_2}{A_3} E_{lz} \\
A_6 &= \frac{\beta_1 \beta_3}{A_3} E_{lz} \\
A_7 &= (-1)^n \beta_1 \beta_4 E_{lz} \\
A_8 &= \beta_1 E_{lz} \\
\phi &= \lambda_n B \\
\lambda_n &= \frac{(2n-1)\pi}{2B} \\
\beta_1 &= \frac{\varepsilon \zeta}{\mu} \\
\beta_2 &= \left[\frac{32 (B\kappa)^2}{\pi^2 (2n-1)^2 [(2B\kappa)^2 + \pi^2 (2n-1)^2]} \right] \\
\beta_3 &= \left[1 - \frac{\tanh(B\kappa)}{B\kappa} \right] \\
\beta_4 &= \left[\frac{2\kappa^2}{\lambda_n B (\kappa^2 + \lambda_n^2)} \right]
\end{aligned}$$

A-2.1 Expressions for constants of non-dimensional governing equation

$$C'_1 = \frac{0.63304 + 0.6366 \ln \frac{r_\infty}{B}}{2\alpha_1}$$

$$C'_2 = \frac{\alpha_1 + 0.245}{\alpha_1}$$

$$C'_3 = \frac{1}{3\alpha_1 \left[\phi^4 - 6e^{-\frac{\phi^2 t^*}{3}} \right]} \left[\phi^6 (1 - \alpha_1) - 4\phi^2 e^{-\frac{\phi^2 t^*}{3}} + 3\phi^4 \right]$$

$$C'_4 = 0.212 + \frac{\alpha_2}{\alpha_1} \left(\frac{\alpha_3}{\phi^2} e^{-\frac{\phi^2 t^*}{3}} - \beta_3 \right) (1 - \alpha_1)$$

$$C'_5 = \frac{\alpha_2}{3\alpha_1} \left\{ \frac{\phi^4 \alpha_1}{\phi^4 - 6e^{-\frac{\phi^2 t^*}{3}}} \left[\alpha_3 e^{-\frac{\phi^2 t^*}{3}} - \beta_3 \phi^2 \right] + \alpha_3 e^{-\frac{\phi^2 t^*}{3}} (\alpha_1 - 1) \right. \\ \left. + \frac{\beta_3 \phi^4 (\phi^2 + 3)}{\phi^4 - 6e^{-\frac{\phi^2 t^*}{3}}} - \frac{\phi^2 \alpha_3 (\phi^2 + 3) e^{-\frac{\phi^2 t^*}{3}}}{\phi^4 - 6e^{-\frac{\phi^2 t^*}{3}}} \right. \\ \left. + \frac{4\phi^2 \left(e^{-\frac{2\phi^2 t^*}{3}} - \beta_3 e^{-\frac{\phi^2 t^*}{3}} \right)}{\phi^4 - 6e^{-\frac{\phi^2 t^*}{3}}} + \frac{e^{-\frac{2\phi^2 t^*}{3}}}{\phi^4 - 6e^{-\frac{\phi^2 t^*}{3}}} \right\} + \frac{Bo}{144\alpha_1 Oh^2}$$

$$C'_6 = \frac{1}{72\alpha_1 Oh^2} (\gamma - \cos \theta)$$

where,

$$\alpha_1 = \frac{\left[\phi^4 e^{\frac{\phi^2 t^*}{3}} - 4 \right]}{\left[\phi^4 e^{\frac{\phi^2 t^*}{3}} - 6 \right]}$$

$$\alpha_2 = \frac{Eo\lambda^*}{12Oh^2}$$

$$\alpha_3 = \left[\frac{2(B\kappa)^2}{[(B\kappa)^2 + \phi^2]} \right]$$

A-3 Detailed explanation of numerical technique used

Equations 2.11, 6.14 and 7.20 are the generalized form of the non-dimensional governing equation. One can represent this second order ordinary differential equation into two first order ordinary differential equation as follows;

$$\frac{dh^*}{dt^*} = v^* \quad (\text{A-1})$$

$$\frac{dv^*}{dt^*} = -\frac{C_2v^{*2} + (C_3h^* + C_4)v^* + C_5h^* + C_6}{(h^* + C_1)} \quad (\text{A-2})$$

Equations A-1 and A-2 are solved simultaneously using fourth order Runge-Kutta(RK) method (Chapra, 2003). In fourth order RK method, four slopes at different intervals are determined. First, the slopes (k) of both the variables (h^*, v^*) at the initial value is determined (k_1) and set of k_1 's is further used to predict the dependent variable at the midpoint of the interval. Then set of slopes at the midpoint (k_2 's) are computed with new interval values. These new slope values are used again to predict the midpoint interval value which leads to the new predictions of midpoint slope values (k_3 's). New set of midpoint of slope values are further used to determine the slope at the end point of the interval (k_4 's). Finally, the slopes (k 's) are combined to compute the prediction of dependent variable at next interval. For any function $[f(h, t)]$, the expressions for k 's can be written as

$$\begin{aligned} k_1 &= \Delta t^* f(t_i^*, h_i^*) \\ k_2 &= \Delta t^* f\left(t_i^* + \frac{\Delta t^*}{2}, h_i^* + \frac{k_1}{2}\right) \\ k_3 &= \Delta t^* f\left(t_i^* + \frac{\Delta t^*}{2}, h_i^* + \frac{k_2}{2}\right) \\ k_4 &= \Delta t^* f(t_i^* + \Delta t^*, h_i^* + k_3) \end{aligned}$$

Finally, the the

$$h_{i+1} = h_i + \frac{k_1}{6} + \frac{k_2}{3} + \frac{k_3}{3} + \frac{k_4}{6}$$

Fortran 77 is used to solve the time step independent solution for the governing equation.

References

Dreyer M., Delgado A., and Path H. -J., Capillary rise of liquid between parallel plates under microgravity. *Journal of Colloid And Interface Science*, 163(1):158–168, 1994.

Chapra S. *Numerical methods for engineers*, Third Edition, McGraw-Hill, 2003.